NASA/TP—2002-210780

The New NASA Orbital Debris Engineering Model ORDEM2000

Jer-Chyi Liou
Lockheed Martin Space Operations
Houston, Texas

Mark J. Matney
Lockheed Martin Space Operations
Houston, Texas

Phillip D. Anz-Meador
Viking Science and Technology, Inc.
Houston, Texas

Donald Kessler
Consultant
Asheville, North Carolina

Mark Jansen
Hernandez Engineering
Houston, Texas

Jeffery R. Theall
NASA Johnson Space Center
Houston, Texas

May 2002

The NASA STI Program Office . . . in Profile

Since its founding, NASA has been dedicated to the advancement of aeronautics and space science. The NASA Scientific and Technical Information (STI) Program Office plays a key part in helping NASA maintain this important role.

The NASA STI Program Office is operated by Langley Research Center, the lead center for NASA's scientific and technical information. The NASA STI Program Office provides access to the NASA STI Database, the largest collection of aeronautical and space science STI in the world. The Program Office is also NASA's institutional mechanism for disseminating the results of its research and development activities. These results are published by NASA in the NASA STI Report Series, which includes the following report types:

- TECHNICAL PUBLICATION. Reports of completed research or a major significant phase of research that present the results of NASA programs and include extensive data or theoretical analysis. Includes compilations of significant scientific and technical data and information deemed to be of continuing reference value. NASA's counterpart of peer-reviewed formal professional papers but has less stringent limitations on manuscript length and extent of graphic presentations.

- TECHNICAL MEMORANDUM. Scientific and technical findings that are preliminary or of specialized interest, e.g., quick release reports, working papers, and bibliographies that contain minimal annotation. Does not contain extensive analysis.

- CONTRACTOR REPORT. Scientific and technical findings by NASA-sponsored contractors and grantees.

- CONFERENCE PUBLICATION. Collected papers from scientific and technical conferences, symposia, seminars, or other meetings sponsored or cosponsored by NASA.

- SPECIAL PUBLICATION. Scientific, technical, or historical information from NASA programs, projects, and mission, often concerned with subjects having substantial public interest.

- TECHNICAL TRANSLATION. English-language translations of foreign scientific and technical material pertinent to NASA's mission.

Specialized services that complement the STI Program Office's diverse offerings include creating custom thesauri, building customized databases, organizing and publishing research results . . . even providing videos.

For more information about the NASA STI Program Office, see the following:

- Access the NASA STI Program Home Page at ***http://www.sti.nasa.gov***

- E-mail your question via the Internet to help@sti.nasa.gov

- Fax your question to the NASA Access Help Desk at (301) 621-0134

- Telephone the NASA Access Help Desk at (301) 621-0390

- Write to:
  NASA Access Help Desk
  NASA Center for AeroSpace Information
  7121 Standard
  Hanover, MD 21076-1320

NASA/TP—2002-210780

The New NASA Orbital Debris Engineering Model ORDEM2000

Jer-Chyi Liou
Lockheed Martin Space Operations
Houston, Texas

Mark J. Matney
Lockheed Martin Space Operations
Houston, Texas

Phillip D. Anz-Meador
Viking Science and Technology, Inc.
Houston, Texas

Donald Kessler
Consultant
Asheville, North Carolina

Mark Jansen
Hernandez Engineering
Houston, Texas

Jeffery R. Theall
NASA Johnson Space Center
Houston, Texas

National Aeronautics and
Space Administration

Johnson Space Center
Houston, Texas 77058-3696

May 2002

Acknowledgments

We would like to thank Dr. Paula Krisko for helping with the EVOLVE simulations and Mrs. Sara Portman for preparing figures and processing the manuscript.

Available from:

NASA Center for AeroSpace Information
7121 Standard
Hanover, MD 21076-1320

National Technical Information Service
5285 Port Royal Road
Springfield, VA 22161

This report is also available in electronic form at http://techreports.larc.nasa.gov/cgi-bin/NTRS

Contents

	Page
1. Introduction	1
1.1 Requirements of an Engineering Model	1
1.2 Applicability of an Engineering Model	2
1.3 An Historical Overview of Engineering Models	2
1.4 Point of Contact	3
2. Data Sources and Data Analysis	4
2.1 Data Overview	4
2.1.1 Space Surveillance Network Catalog	5
2.1.2 The Long-Duration Exposure Facility	7
2.1.3 The Long-Range Imaging Radar	10
2.1.4 Haystack Auxiliary Radar	11
2.1.5 Hubble Space Telescope solar arrays	12
2.1.6 The European Retrievable Carrier	14
2.1.7 Space Transportation System Orbiter	15
2.1.8 The Goldstone Radar	16
2.1.9 The Space Flyer Unit	17
2.1.10 *Mir*	19
2.1.10.1 Orbital Debris Collection Experiment	19
2.1.10.2 Other *Mir*-Based Impact Experiments	20
2.2 Data Analysis	20
2.2.1 The Maximum Likelihood Estimator	20
2.2.2 Primary Data	22
2.2.2.1 Space Surveillance Network	22
2.2.2.2 Long-Duration Exposure Facility	23
2.2.2.3 Long-Range Imaging Radar (“Haystack”)	30
2.2.3 Secondary Data	32
2.2.3.1 Shuttle Data	32
2.2.3.2 The Goldstone Radar	33
2.2.3.3 HST Solar Array Impacts	35
2.2.3.4 The European Retrievable Carrier	36
2.2.3.5 Aerogel Impact Experiments Aboard the *Mir* Space Station	36
2.2.4 Solar-Related Effects Modeling	37
2.2.4.1 Projected Solar Activity for Atmospheric Drag	37
2.2.4.2 Solar Radiation Pressure	38

Contents
(continued)

	Page
2.2.5 EVOLVE Auxiliary Modeling	39
2.2.6 Future Launch Traffic Model	43
2.2.7 Extension of Data Sets to 2000 km Altitude	44
3. ORDEM2000 Debris Environment Model	46
3.1 A Finite Element Model for LEO Debris Environment	47
3.2 Applications of the Debris Environment Model	50
3.2.1 For a Ground-based Observer	51
3.2.2 For an Orbiting Spacecraft	51
4. ORDEM2000 Verification and Validation	52
4.1 Comparisons With Radar Observations	52
4.2 Comparisons With In Situ Measurements	58
4.2.1 Space Shuttle	58
4.2.2 HST Solar Array	60
4.2.3 EuReCa Solar Arrays	60
4.2.4 MEEP Experiment Aboard *Mir*	61
4.3 Sensitivity Analysis	62
5. ORDEM2000 Graphic User Interface	64
5.1 Introduction	64
5.2 Program Requirements	64
5.3 Program Installation	64
5.4 Program Execution	65
5.4.1 Graphical User Interface-Based Computation	65
5.4.1.1 Example Telescope Assessment	65
5.4.1.2 Spacecraft Assessment	69
5.4.2 DOS-Based Computation	72
5.5 Output Data File Names in the Program	73
6. References	74
Appendix A: ORDEM96 vs. ORDEM2000	A-1
Appendix B: Debris Flux at 400 km Altitude (1999-2030)	B-1
Appendix C: Average Velocity Distributions	C-1

Contents
(continued)

Page

Tables

Table 2-1: The Ten Data Sources 6
Table 2-2: LDEF Cratering Record 9
Table 2-3: Haystack Data Sets Used 10
Table 2-4: Goldstone Radar Observations. 16
Table 2-5: Selected Goldstone Data Showing Time of Detection, Range, Range-Rate, and RCS in Square Millimeters 17
Table 2-6: LDEF Material Properties Used in the Computations 24
Table 2-7: Table of Values Used to Adjust the Environment Based on the STS Data Fits 33
Table 2-8: Table of Values Used to Adjust the 1-mm Environment Based on Goldstone Data Fits 34
Table 5-1: Output Data Files 73

Figures

Figure 2-1: The orientation of LDEF as viewed from the space-facing end 7
Figure 2-2: A typical HAX surface area flux from FY97 11
Figure 2-3: Impacts upon the HST solar arrays (with inset cross section of a solar cell) 13
Figure 2-4: HST-SA cross-sectional flux 14
Figure 2-5: EuReCa measurements 15
Figure 2-6: The SFU spacecraft 18
Figure 2-7: Exposed facility flyer unit cross section (not to scale; some layers accentuated) 18
Figure 2-8: Cumulative size distribution of LEO-crossing SSN objects in 1999 23
Figure 2-9: Crater feature distribution on the space-facing Humes surface along with the LDEF meteoroid fit 26
Figure 2-10: Crater feature distributions at two different limiting sizes on the various Humes surfaces along the LDEF sides as a function of yaw angle 27
Figure 2-11: Crater feature distributions at two different limiting sizes on the various intercostal surfaces along the LDEF sides as a function of yaw angle 28
Figure 2-12: Crater feature distributions on the CME gold surface on the rear side of LDEF broken out by craters made by debris only and meteoroids only 28
Figure 2-13: Total crater feature distributions on the CME aluminum surface compared to the fit 29
Figure 2-14: The CME aluminum surface was not able to distinguish some of the craters between meteoroids and debris 29

Contents
(continued)

		Page
Figure 2-15:	The orbit families estimated from the Haystack data using the EM method have been broken out by eccentricity and the spatial density with altitude is shown in comparison to the equivalent populations in the catalog	31
Figure 2-16:	The orbit families estimated from the Haystack data have been broken out by inclination for the low-eccentricity population	31
Figure 2-17:	The orbit families estimated from the Haystack data have been broken out by inclination for the high-eccentricity population	32
Figure 2-18:	The Goldstone data give some indication of the populations of debris in the 1-mm to 1-cm size range	34
Figure 2-19:	A comparison of historical and projected solar activities	38
Figure 2-20:	Spatial density variation between 1991 and 2030 for debris >10 µm in size	40
Figure 2-21:	Spatial density variation between 1991 and 2030 for debris >100 µm in size	41
Figure 2-22:	Spatial density variation between 1991 and 2030 for debris >1 mm in size	41
Figure 2-23:	Spatial density variation between 1991 and 2030 for debris >1 cm in size	42
Figure 2-24:	Spatial density variation between 1991 and 2030 for debris >10 cm in size	42
Figure 2-25:	Spatial density variation between 1991 and 2030 for debris >1 m in size	43
Figure 2-26:	Historical and projected launch traffic	44
Figure 3-1:	ORDEM96 and ORDEM2000 use different approaches to build the LEO debris environment model	46
Figure 3-2:	A finite element model	48
Figure 3-3:	Velocity distribution matrix	49
Figure 3-4:	Color-coded spatial density distribution (no/km3) of 100-µm objects	50
Figure 4-1:	ORDEM2000 vs. HAX data (1999, objects ≥1 m)	52
Figure 4-2:	ORDEM2000 vs. HAX data (1999, objects ≥10 cm)	53
Figure 4-3:	ORDEM2000 vs. HAX data (1999, objects ≥5 cm)	53
Figure 4-4:	ORDEM2000 vs. Haystack data (1999, objects ≥1 cm)	54
Figure 4-5:	ORDEM2000 vs. HAX data (1998, objects ≥1 m)	54
Figure 4-6:	ORDEM2000 vs. HAX data (1998, objects ≥10 cm)	55
Figure 4-7:	ORDEM2000 vs. HAX data (1998, objects ≥5 cm)	55
Figure 4-8:	ORDEM2000 vs. Haystack data (1998, objects ≥1 cm)	56
Figure 4-9:	ORDEM2000 vs. HAX data (1997, objects ≥1 m)	56

Contents
(concluded)

		Page
Figure 4-10:	ORDEM2000 vs. HAX data (1997, objects ≥10 cm)	57
Figure 4-11:	ORDEM2000 vs. HAX data (1997, objects ≥5 cm)	57
Figure 4-12:	ORDEM2000 vs. Haystack data (1997, objects ≥1 cm)	58
Figure 4-13:	ORDEM2000 predictions of the Shuttle radiator tape-hole-diameter distributions	59
Figure 4-14:	ORDEM2000 population predictions of the Shuttle window crater-depth distributions	59
Figure 4-15:	The ORDEM2000 predictions of HST conchoidal crater-diameter distributions	60
Figure 4-16:	The ORDEM2000 population predictions of the EuReCa conchoidal crater-diameter (D_{co}) distributions	61
Figure 4-17:	ORDEM population size predictions compared to the *Mir* MEEP size distribution estimates	62
Figure 4-18:	Predicted average cross-sectional area flux on a spacecraft with an ISS-type orbit	63
Figure 5-1:	ORDEM2000 main panel	65
Figure 5-2:	Telescope Assessment Choice panel	66
Figure 5-3:	Telescope Input panel	66
Figure 5-4:	ORDEM2000_fort.exe window	67
Figure 5-5:	Telescope Results window	68
Figure 5-6:	Display of Spatial Density vs. Altitude for Telescope	68
Figure 5-7:	Spacecraft Assessment panel	69
Figure 5-8:	DOS computation panel	70
Figure 5-9:	Computation completed panel for the spacecraft mode	71
Figure 5-10:	Graph of flux over orbit	71
Figure A-1:	ORDEM2000, ORDEM96 vs. HAX data (1999, objects >1 m)	A-1
Figure A-2:	ORDEM2000, ORDEM96 vs. HAX data (1999, objects >10 cm)	A-2
Figure A-3:	ORDEM2000, ORDEM96 vs. Haystack data (1999, objects >1 cm)	A-2
Figure B-1:	Debris flux on ISS in 2000	B-1
Figure B-2:	Debris flux on ISS in 2005	B-2
Figure B-3:	Debris flux on ISS in 2010	B-2
Figure B-4:	Debris flux on ISS in 2015	B-3
Figure B-5:	Debris flux on ISS in 2020	B-3
Figure B-6:	Debris flux on ISS in 2025	B-4
Figure B-7:	Debris flux on ISS in 2030	B-4

Acronyms

CME	Chemistry of Meteoroids Experiment
D_{co}	conchoidal feature diameter
D_p	particle (impactor) diameter
EM	expectation maximization
ESA	European Space Agency
ESEF	European Space Exposure Facility
EuReCa	European Retrievable Carrier
GOST	Soviet Union orbital debris engineering model
GUI	graphical user interface
HAX	Haystack Auxiliary radar
HST	Hubble Space Telescope
JSC	Lyndon B. Johnson Space Center
LDEF	Long-Duration Exposure Facility
LEO	low Earth orbit
MASTER'99	ESA engineering model
MEEP	*Mir* Experiments Exposure Package
MLE	maximum likelihood estimator
MLI	multilayer insulation
MSAFE	Marshall Solar Activity Future Estimation
NOAA	National Oceanic and Atmospheric Administration
ODC	Orbital Debris Collection Experiment
ORDEM	Orbital Debris Engineering Model
PIE	Particle Impact Experiment
POSA	passive optical sample assembly
PPMD	polished plate meteoroid detector
RCS	radar cross section
SBRAM	satellite breakup risk-assessment model
SEM	Size Estimation Model
SFU	Space Flyer Unit
SSN	Space Surveillance Network
STS	space transportation system

Foreword

The NASA Orbital Debris Program Office at Johnson Space Center has developed a new computer-based orbital debris engineering model, ORDEM2000. The model describes the orbital debris environment in the low Earth orbit region between 200 and 2000 km altitude. The model is appropriate for those engineering solutions requiring knowledge and estimates of the orbital debris environment (debris spatial density, flux, etc.). ORDEM2000 can also be used as a benchmark for ground-based debris measurements and observations.

We incorporated a large set of observational data (both in situ and ground-based), covering the object size range from 10 μm to 10 m, into the ORDEM2000 debris database, employing a new analytical technique utilizing a maximum likelihood estimator to convert observations into debris population probability distribution functions. These functions then form the basis of debris populations. We developed a finite element model to process the debris populations to form the debris environment. A more capable input and output structure and a user-friendly graphical user interface are also implemented in the model. ORDEM2000 has been subjected to a significant verification and validation effort. Currently, ORDEM2000 runs on Windows 95/98/2000/NT computers. An interactive UNIX version is also available.

1. Introduction

This document describes the new NASA Orbital Debris Engineering Model, ORDEM2000. ORDEM2000 supersedes the previous model, ORDEM96. The availability of new sensor and in situ data, as well as new analytical techniques, has enabled the construction of this new model. This section describes the general requirements and scope of an engineering model. Data analyses and the theoretical formulation of the model are described in Sections 2 and 3. Section 4 describes the verification and validation effort and the sensitivity and uncertainty analyses. Finally, Section 5 describes the graphical user interface (GUI), software installation, and test cases for the user.

1.1 Requirements of an Engineering Model

The primary requirement for any engineering model is to provide the user accurate results in a timely fashion. Two main constituencies compose the ORDEM user community: spacecraft designers and operators, and debris observers. A third user group includes spacecraft designers and analysts using the Debris Assessment Software package. Engineering models, currently the ORDEM96 code, form the heart of the Debris Assessment Software orbital debris environment subroutines.

The requirements of each user group differ somewhat, though they of course share many common requirements. For example, the designer of an oriented spacecraft requires more detailed estimates of the flux than the designer of a randomly oriented or randomly tumbling spacecraft. In the case of the former vehicle, a designer may prefer the flux to be described in terms of azimuth in the local horizontal plane so as to design shielding in the most cost-effective manner. Such detail is not required in the case of a randomly tumbling spacecraft. Both designers, however, would be concerned with the distribution of debris flux as a function of size and altitude. Because of the long lead times in new satellite designs, the temporal behavior of the debris environment over a satellite life cycle is of interest. In the case of an observer planning a debris observation campaign, results will be dependent upon the inclination distribution of resident space objects visible to the ground-based sensor site; further complications result depending upon whether the sensor is fixed in its orientation or is steerable in azimuth and elevation. In the case of bistatic radars utilizing parallax, the altitude distribution becomes of crucial importance due to common field of view constraints.

Thus, any engineering model must include an accurate assessment of the orbital debris environment as a function of altitude, latitude, and debris size. ORDEM2000 is an engineering model that is consistent with this requirement. It is based on debris populations with various altitude, inclination, and size distributions. The model provides a complete description of the environment in terms of debris flux onto spacecraft surfaces or debris detection rate observed by a ground-based sensor.

1.2 Applicability of an Engineering Model

Engineering models are applicable to the problems described in the preceding section. Some problems, however, are beyond the scope of an engineering model. For example, one cannot evaluate the short-term collision risk, due to fragments from recent breakup events, relative to an orbiting satellite using an engineering model. In addition, the long-term impact of various mitigation measures on the debris environment must rely on a debris evolution model that includes secular effects such as the solar activity cycle, which affects atmospheric density and hence the decay rate of objects in low Earth orbit (LEO), the growth of the space vehicle population, and a projected fragmentation rate. Other models, such as the NASA SBRAM (satellite breakup risk-assessment model) and the NASA EVOLVE long-term debris evolution model, are more applicable to examining the consequences of such phenomena.

1.3 An Historical Overview of Engineering Models

Engineering models were first assembled for agency internal use. Kessler (1984) developed the first debris engineering model for the Space Station Program Office. Further models were assembled for the Strategic Defense Initiative Organization and various LEO spacecraft programs (Kessler et al. 1989) and, again, the Space Station Program Office (Kessler et al. 1991). Each of these models portrayed the environment in terms of curve fits to describe the distributions of large objects (the Space Surveillance Network – or SSN – catalog of objects larger than approximately 10 cm) and small objects (as recorded by the inspection of surfaces exposed to, and returned from space). Both periodic (solar cycle) and secular (growth rate) effects were included explicitly. A significant requirement of these models was that they be easily executed by a programmable calculator or be capable of manipulation "by hand" in a reasonable amount of time.

The need to better define the debris environment eventually outgrew this latter requirement. ORDEM96 (Kessler et al. 1996) was the first model that required a personal computer for effective implementation. ORDEM96 pioneered the use of debris population ensembles characterized by altitude, eccentricity, inclination, and size. ORDEM2000 adopts a similar approach, but it replaces the final remnants of curve fitting, as used by all previous NASA engineering models, with a finite element model to represent the debris environment.

Engineering models are not limited to the NASA models mentioned above. For example, the European Space Agency (ESA) MASTER'99 (Sdunnus et al. 2001) series of models performs similar functions, as did the former Soviet Union's GOST three-population (orbital debris, micrometeoroids, and "Earth-orbiting meteoroids") engineering model. MASTER'99 is similar to the ORDEM series of models, whereas the GOST model is more similar to the earlier NASA models.

1.4 Point of Contact

The official point of contact for ORDEM2000 at the NASA Orbital Debris Program Office is:

Dr. James F. Pawlowski
Mail Code: SX
NASA Johnson Space Center
Houston, TX 77058
USA

Phone: (281) 483-0038
Email: james.f.pawlowski1@jsc.nasa.gov

2. Data Sources and Data Analysis

2.1 Data Overview

Ten data sources form the basic database of ORDEM2000 (Table 2-1):

- SSN catalog
- Haystack and Haystack Auxiliary (HAX) radar data (Settecerri et al. 1999)
- Goldstone radar data (e.g., Matney et al. 1999)
- Impact measurements from the Long-Duration Exposure Facility (LDEF) (e.g., Levine 1991, 1992, 1993)
- Hubble Space Telescope Solar Array (HST-SA) impact data (Drolshagen et al. 1997, McDonnell et al. 1998a,b)
- European Retrievable Carrier (EuReCa) impact data (Drolshagen et al. 1996, McDonnell et al. 1998a,b)
- Space Shuttle window and radiator impact data (Hyde et al. 2000a,b)
- Space Flyer Unit (SFU) data (Yano 1999)
- *Mir* impact data (Hörz et al. 1999)

They are described in detail in the following sections.

As will be described in Section 3, we based the ORDEM2000 model on five pre-calculated debris populations. They correspond to objects of five different size thresholds: 10 µm and greater, 100 µm and greater, 1 cm and greater, 10 cm and greater, and 1 m and greater (hereafter referred to as 10-µm, 100-µm, 1-cm, 10-cm, and 1-m populations). We used the major sources to build the debris populations, while the other sources were used to verify and validate the model predictions.

We used the following major data sources to obtain our five populations:

SSN catalog	build the 1-m and 10-cm populations
Haystack radar data	build the 1-cm population
LDEF measurements	build the 10-µm and 100-µm populations

Since no direct measurement at 1 mm is available, the 1-mm debris population in the model is based on an interpolation between the 100-µm and 1-cm populations. Goldstone radar data for the 3-mm objects are used to justify the interpolation.

Before construction of the model, a decision was made regarding the time baseline of the environment. We selected the debris populations to be those on a preselected reference date: January 1, 1999. We used the SSN catalog from the same reference date and projected the Haystack debris detection from each year to the reference date using the historical growth rate of

the 1-cm population from the NASA orbital debris evolution model EVOLVE 4.0 (Krisko et al. 2000). We then used the combined Haystack data to build the 1-cm population as of January 1, 1999. The LDEF debris impact data are first processed with a simple model that calculates the historical 10-µm and 100-µm debris populations, including the effects of atmospheric drag and solar radiation pressure. We then scaled the number of debris impacts detected during the LDEF mission (1984-1990) with the model prediction during the same period and then projected them to January 1, 1999.

2.1.1 Space Surveillance Network Catalog

The United States Space Command SSN is composed of ground- and space-based sensor systems whose charter is to track human-made resident space objects. These data are compiled daily into Keplerian element sets and distributed to the user community via NASA Goddard Space Flight Center's Orbital Information Group. In addition, the United States Space Command maintains an archive of historical element sets. This archive was supplied to the NASA Orbital Debris Program Office at Johnson Space Center (JSC) and, coupled with regular updates, comprises our element set database.

We use two ancillary data sets in conjunction with the two-line element data: the radar cross section (RCS)-size data set and the area-to-mass ratio database. The RCS-size data set consists of an object identifier, an on-orbit/decayed flag, the number of unique (non-default, non-repeating, non-blank) observations of a particular object, and a statistical description of RCS and size ("characteristic length") of the object, including the median and mean RCSs, the standard deviation, skewness and kurtosis of the RCSs, and median and mean sizes. We use the NASA Size Estimation Model (SEM) to derive size from RCS.

The area-to-mass ratio database, consisting of several databases, contains statistical area-to-mass ratio data for individual members of various debris clouds/ensembles, including the rocket body (Delta, Agena, Long March, Ariane, Able Star(t), etc.), spacecraft (Cosmos 1275, etc.), and miscellaneous (P78, Cosmos 1813, etc.) debris ensembles. Specific debris-generating categories of space vehicles examined include, but are not limited to, U.S. Delta 100 and 1000 series rocket bodies, Agena D rocket bodies, Soviet Anti-Satellite Interceptor vehicles, and Soviet/Russian Electronic Ocean Reconnaissance satellites. The area-to-mass ratios of debris fragments were determined from the orbital decay history of those fragments using a Jacchia atmospheric model and measured values of solar activities.

The SSN auxiliary data includes, but is not limited to, direct access files linking SSN catalog number, mean and median RCS, mean and median size, source identity (e.g. U.S., Japan, etc.), and object type identity (e.g. fragmentation debris, operational debris, spacecraft, etc.).

Table 2-1: The Ten Data Sources

	Size range	Altitude Range (km)	Inc. Range (degree)	Time of Collection
SSN	10 cm to 10 m	200 to 2000	All	up to Dec. 99
Haystack	0.3 cm to 10 m 0.5 cm to 10 m 0.5 cm to 10 m 0.5 cm to 10 m 1.0 cm to 10 m	350 to 1100 350 to 650 350 to 650 700 to 1100 1200 to 2100	40 to 140 28 to 152 32 to 148 32 to 148 40 to 140	91 to 99 91 to 99 91 to 94 94 to 98 93,94,96,97
HAX	1.0 cm to 10 m 0.8 cm to 10 m	450 to 1050 450 to 1050	40 to 140 40 to 140	94 to 97 98 to 99
LDEF[a]	0.01 to 1 mm	330 to 480	All	Apr. 84 to Jan. 90
HST-SA	0.01 to 1 mm	586 to 614	All	Apr. 90 to Dec. 93
EuReCa	0.005 to 0.5 mm	502 to 508	All	Aug. 92 to Jun. 93
Shuttle[b]	0.1 to 1 mm	300 to 400	All	95 to 98
SFU	10 μm to 1 mm	480	All	Mar. 95 to Jan. 96
Mir	10 to 100 μm	170 to 300	All	Mar. 96 to Oct. 97
Goldstone	2 mm to 2 cm	280 to 2000	32 to 148	Oct. 94 to Oct. 98

[a]LDEF: Space Debris Impact Experiment (D. Humes), Chemistry of Meteoroid Experiment (F. Hörz), Interplanetary Dust Experiment (F. Singer), LDEF frame (M/D Special Investigation Group).

[b]Shuttle: STS-50, 56, 71, 72, 73, 75, 76, 77, 79, 80, 81, 84, 85, 86, 87, 88, 89, 91, 94, 95, 96.

2.1.2 The Long-Duration Exposure Facility

LDEF is a unique data set for several reasons. LDEF had a number of surfaces that were deliberately designed and calibrated to measure the debris environment. LDEF maintained its orientation throughout its mission, allowing for a detailed analysis of the directionality of the debris and meteoroid impactors (for a good overview of the LDEF project and details of the various experiments described below, see the Proceedings from the First, Second, and Third LDEF Conferences, Levine et al. 1991, 1992, and 1993).

LDEF (international designator 1984-034B, catalog number 14898) was in a circular, 28.5-deg-inclination orbit for 5.77 years (1.8196×10^8 seconds)—much longer than originally planned. It was deployed on the STS-41C flight of the Space Shuttle *Challenger* (launched April 6, 1984). The initial orbit was at 480-km altitude, but had dropped to 331-km altitude due to atmospheric drag by the time it was recovered by the Space Shuttle *Columbia* (STS-32) on January 12, 1990. The time-averaged altitude was 457 km, so that is the value used for the calculations.

LDEF was designed as a multi-faceted cylinder with 12 faces and two end-pieces. The spacecraft maintained its orientation throughout the mission so that each face along the cylinder pointed in a different yaw angle separated by 30 deg. LDEF was deployed so that the face intended to point in the ram direction actually was rotated 8 deg off ram. In addition, the spacecraft was not deployed perfectly vertical but was canted 2 deg forward at the upper end. Figure 2-1 shows the orientation of LDEF.

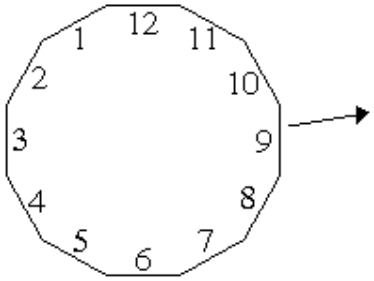

Figure 2-1: The orientation of LDEF as viewed from the space-facing end. The arrow indicates LDEF's direction of motion. The spacecraft was rotated 8 deg from the intended direction.

The data sets consist of crater diameters and location of the feature on the surface. In addition, any information on the chemistry of the impactor or other unique feature is preserved. Other information, such as at what facility the feature was measured, is also preserved.

In preparing for the assembly of data for this analysis, it became clear that the data sets for the various surfaces are not of uniform quality. Some of the surfaces were analyzed much more carefully than others. On some surfaces, it was possible to identify smaller structures than on others.

The intercostals were polished aluminum frame segments that held the experiment trays in place—4 intercostals were available from each of the 12 sides. Because of their highly polished surfaces, the experimenters could reliably detect craters down to sizes less than 50 μm. In addition to the intercostals, there were somewhat larger frame pieces known as longerons. These were not actually removed from the LDEF structure, but they were measured for the largest craters (>500 μm) before the LDEF was disassembled. The facing of each longeron was halfway between each of the 12 side faces—corresponding to 15 deg in yaw difference between the longerons and the neighboring faces. They were numbered so that Longeron 1 was located between LDEF faces 1 and 2.

The Humes experiments (Humes 1991) consisted of aluminum plates designed to measure craters, but the microscopic pitting on the surfaces from the manufacturing techniques made the limiting crater size around 100 μm. Because of resource limitations, only a subset of the surfaces was measured to this accuracy. Because of its unique ability to see meteoroids with minimal contamination by orbital debris, the space-facing surface underwent careful analysis to see the minimum possible crater sizes. Data were also included from the Earth-facing surface. The craters on this surface should be dominated by meteoroids alone. The LDEF database can sometimes be difficult to use, and it is not always clear whether a particular crater has been counted more than once. The data we used are from Humes (1993). We also included some data from the aluminum thermal panels (discussed and tabulated in the same paper). A crater-by-crater data set exists for a majority of the Humes data, but it is not complete (e.g., it does not contain the space-facing surface data), so the cumulative values tabulated in that paper were used.

The Chemistry of Meteoroids Experiment (CME) gold plate (Hörz etal. 1991) on side 3 can distinguish the nature of the impactor—whether it was debris or a meteoroid. Because the gold surface was on the rear side of LDEF and had a very high material density, it is assumed that any debris impacts would be from low-velocity particles that would be the most likely to leave a residue. Meteoroids, on the other hand, would impact the rear with significantly higher velocities, making it more likely that they were vaporized. In those cases where there was no residue found, it was assumed that it was due to a meteoroid. Consequently, the craters were segregated into two categories: debris and meteoroids-plus-unknowns. In essence, this turns the CME gold surface into two detectors—one to measure only debris and the other to measure only meteoroids. The data from the CME aluminum plate on side 11 were also included in this study, but it is possible to use the chemistry on this plate to unambiguously segregate only some of the data into debris and meteoroids. Consequently, for the fit, this surface was treated like the others in that the crater distribution contains an unknown mixture of meteoroids and debris.

Table 2-2: LDEF Cratering Record

Experiment	Material	Side	Area [m^2] / Crater Sizes [μm]
Intercostal	Aluminum 6061-T6	1	0.2376 / >50
Intercostal	Aluminum 6061-T6	2	0.2358 / >50
Intercostal	Aluminum 6061-T6	3	0.2325 / >50
Intercostal	Aluminum 6061-T6	4	0.2352 / >50
Intercostal	Aluminum 6061-T6	5	0.2365 / >50
Intercostal	Aluminum 6061-T6	6	0.2372 / >50
Intercostal	Aluminum 6061-T6	7	0.2380 / >50
Intercostal	Aluminum 6061-T6	8	0.2352 / >50
Intercostal	Aluminum 6061-T6	9	0.2348 / >50
Intercostal	Aluminum 6061-T6	10	0.2391 / >50
Intercostal	Aluminum 6061-T6	11	0.2403 / >50
Intercostal	Aluminum 6061-T6	12	0.2374 / >50
Longerons	Aluminum 6061-T6	1-12*	0.4816 / >500
Humes	Aluminum 6061-T6	1	0.59 / >100 3.69 / >500
Humes	Aluminum 6061-T6	2	0.59 / >100 2.11 / >500
Humes	Aluminum 6061-T6	3	0.59 / >100 1.23 / >500
Humes	Aluminum 6061-T6	4	0.59 / >100 2.51 / >500
Humes	Aluminum 6061-T6	5	0.59 / >100 2.51 / >500
Humes	Aluminum 6061-T6	6	0.59 / >100 3.26 / >500
Humes	Aluminum 6061-T6	7	0.59 / >100 3.54 / >500
Humes	Aluminum 6061-T6	8	0.78 / >100 0.93 / >500
Humes	Aluminum 6061-T6	9	0.3 / >100 0.69 / >500
Humes	Aluminum 6061-T6	10	0.59 / >100 1.33 / >500
Humes	Aluminum 6061-T6	11	0.59 / >100 3.69 / >500
Humes	Aluminum 6061-T6	12	0.59 / >100 1.33 / >500
Humes	Aluminum 6061-T6	Space-Facing	0.0447 / >20 1.14 / >80 5.48 / >500
Humes	Aluminum 6061-T6	Earth-Facing	0.52 / >100 2.84 / >500
Chemistry of Meteoroids Experiment	Aluminum 1100	11	**0.57685 / >100
Chemistry of Meteoroids Experiment	Gold	3	***0.459 / >50

* The longerons were located at yaw angles half-way between the main LDEF faces, so they represent yaw angles offset 15 deg from the faces.

** The CME aluminum plate data used only covered half of the total area of the experiment. The data set appeared to be complete only down to around 100 μm.

*** The CME gold plates had a shell that exposed the surface to space for only a fraction of the time. The area in the table is the estimated equivalent exposure area over the lifetime of the mission.

2.1.3 The Long-Range Imaging Radar

The Long-Range Imaging Radar (hereafter referred to as "Haystack") instrument and the orbital debris data processing are discussed in some detail in the NASA Haystack reports (Settecerri et al. 1999). This section contains a short summary of the data used and rationale for the choices in the data selection.

The primary data analysis requires more information than the standard plots of flux versus altitude because one of the important factors of the flux on a spacecraft is the relative abundance of elliptical and circular orbits. In general, the Haystack measurements by themselves are not precise enough to unambiguously determine the eccentricity of each debris orbit. Therefore, the method outlined in Section 2.2.1 is used to obtain statistical distributions in the orbital parameters using the range and range-rate information.

In principle, one can use an expectation maximization (EM) method (see Section 2.2.1) to simultaneously solve for the conversion from RCS to debris size. However, this could be a daunting computational task. For this study, we limited the EM analysis to determining orbit distributions only. Settecerri et al. (1999) have shown that the populations based on the simple NASA SEM alone are close to those obtained by more sophisticated analysis. The SEM model therefore screens the data sets to give the detection rates of objects with a given size and larger. For the model populations, the final distributions are modified by an altitude-dependent factor to remove the biases introduced in the RCS-to-size conversion. Typically, this factor increased the population by 25% over that estimated from the SEM alone.

We chose a number of view modes from the Haystack data that covered different regions of the LEO environment over a period of a decade. Table 2-3 summarizes the data sets used in the EM analysis.

Table 2-3: Haystack Data Sets Used

Pointing	Time (hours)*	Ranges Used (km)	Range-Rates (km/s)	Years
10 deg South	1279.6	1160 – 2340	+/-11	1991-1999
20 deg South	1534.1	630 – 2570	+/-10	1991-1999
90 deg South	802.0	300 – 2000	+/-6	1991-1998
75 deg East	1270.4	310 – 1620	+/-6	1994-1999
82 deg East	93.8	1200 – 2000	+/-6	1996-1997
20 deg East	149.9	760 – 1740	+/-10.5	1993-1994

*Total hours observed at that pointing direction. Different ranges were observed for different lengths of time over different years.

A number of special long-range modes have been used over the years. We decided to use these data sets to improve our estimation of the population at higher altitudes despite the low number of hours used in some cases.

The Haystack data itself consist of a number of "Events" files that record the basic data measured for each object detected. These data include time of detection, range, range-rate, signal-to-noise ratio, and RCS. The files are maintained at NASA Orbital Debris Program Office.

2.1.4 Haystack Auxiliary Radar

HAX became operational in 1994 and has been used to observe the LEO debris environment since then (Settecerri and Stansbery 1997; Settecerri et al. 1999). Although its sensitivity is lower than Haystack, HAX has a wider field of view (1.7 times that of Haystack). The HAX data complement the Haystack data well. The two HAX observation modes are vertical and 82 deg east. The available data files are from FY94 to FY99. The average debris diameter is determined using the SEM. Figure 2-2 shows the surface area flux between 650- and 750-km altitudes from the 82 deg east mode obtained in FY97. All HAX data are stored in "Events" files, in a manner similar to Haystack data.

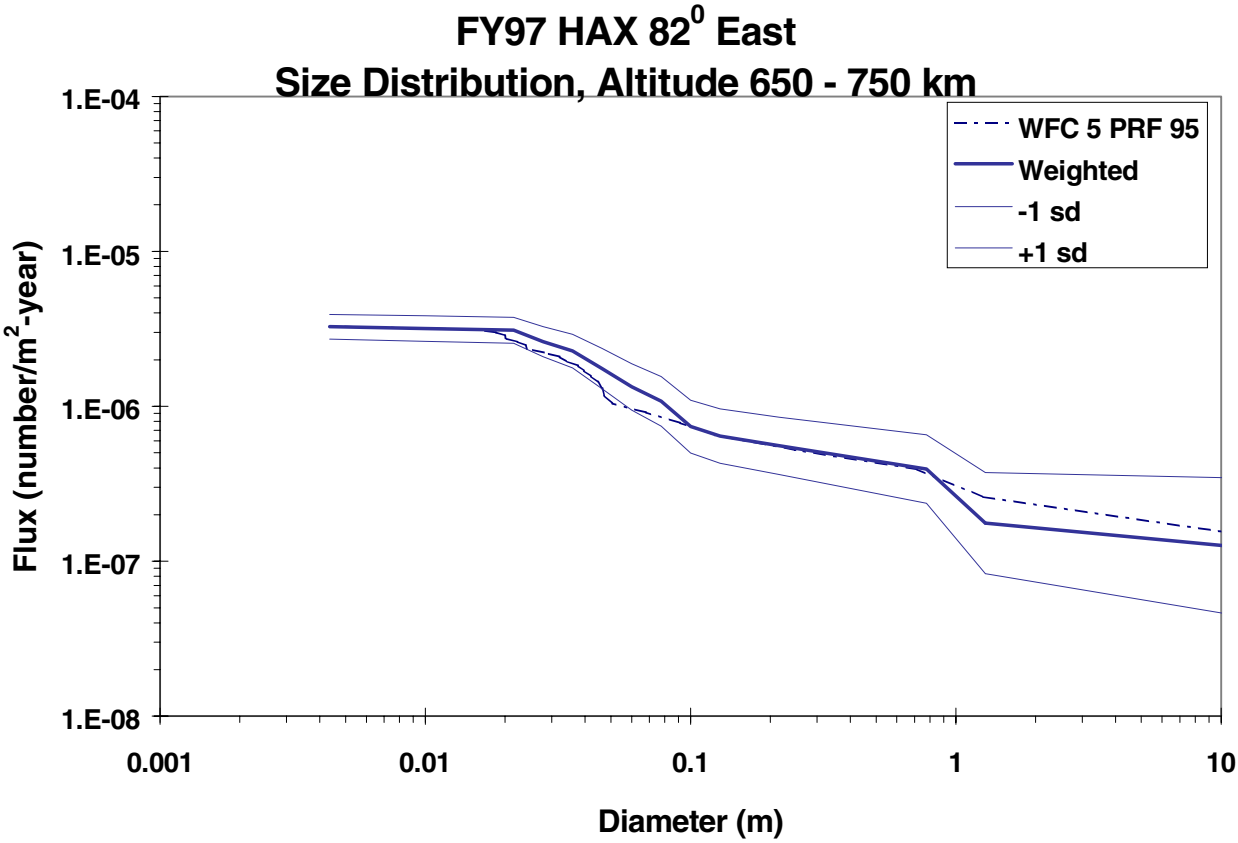

Figure 2-2: A typical HAX surface area flux from FY97.

2.1.5 Hubble Space Telescope solar arrays

The Hubble Space Telescope (HST, international designator 1990-037B, catalog number 20580) was launched on April 24, 1990, into a 28.5-deg-inclination orbit. The HST is designed to be regularly serviced or upgraded on orbit; the STS-61 crew carried out a servicing mission in December 1993. During that 3½ -year period (1320 days), HST had decayed from an original altitude of 614 km to about 586 km. During servicing operations conducted in the STS payload bay, one of the solar arrays (+V2) was unable to retract into its deployment cassette, and was jettisoned on orbit. However, the other (-V2) of the two solar arrays was retrieved and returned to Earth (Drolshagen et al. 1997).

Figure 2-3 (McDonnell et al. 1998b) depicts impacts on the 0.7-mm-thick blanket-type solar array. This figure shows the general orientation of the solar arrays with respect to the HST bus. As may be seen, each solar array was assembled from five solar panel assemblies, designated A-E and AA-EE. Each solar panel assembly is further composed of 160 solar cells arranged in series. The inset figure in Figure 2-3 depicts a typical solar cell in cross section.

The ESA maintains the impact analyses results. These data, and the data reduction procedure, are discussed in detail by McDonnell et al. (1998a,b), hereafter referred to as the Unispace reports. Data consist of raw and reduced data tables and descriptions, impact crater and penetration images, results of chemical analyses on the crater residues, and reports and papers. HST-SA surfaces examined include multilayer insulation (MLI) blankets, the solar array panels, and other surfaces exposed to space. As with EuReCa data (below), interpolation of hypervelocity data into thin surfaces was used to relate impact crater diameters to debris diameters. Figure 2-4 depicts the cumulative cross-sectional flux, measured from the four faces of the solar array, as a function of size based on the published data (McDonnell et al. 1998a). It is based on the assumption that the projectiles have a density of 4 g/cm^3 with an average impact velocity of 10 km/sec.

The nomenclature adopted is that of the Unispace reports. Here, “front” refers to the sun-facing side of the array; “rear” refers to the side oriented in the anti-sun direction; “top”/“upper” refers to array sections A-E; and “bottom”/“lower” refers to array sections AA-EE. The latter nomenclature refers to the order in which the array was stowed within its cassette. “Top” panels literally lay upon the “bottom” panels. Chemical analyses were performed on impactor residue found within HST solar array craters. Graham et al. (2000) report upon a selection of impactors and identify impactor type.

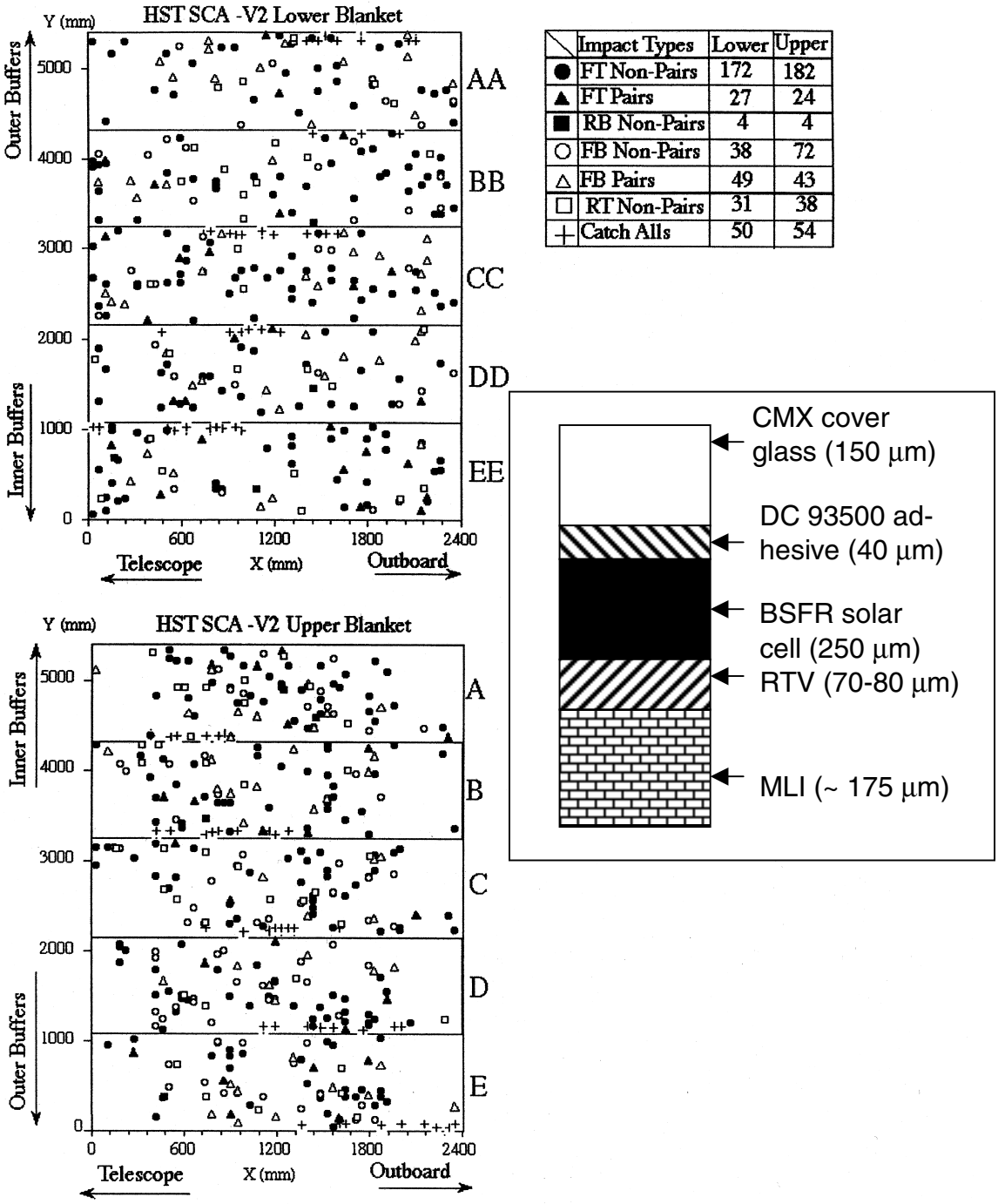

Impact Types	Lower	Upper
● FT Non-Pairs	172	182
▲ FT Pairs	27	24
■ RB Non-Pairs	4	4
○ FB Non-Pairs	38	72
△ FB Pairs	49	43
□ RT Non-Pairs	31	38
+ Catch Alls	50	54

Figure 2-3: Impacts upon the HST solar arrays (with inset cross section of a solar cell). From: McDonnell et al., 1998b. Solar cell component thickness is not to scale.

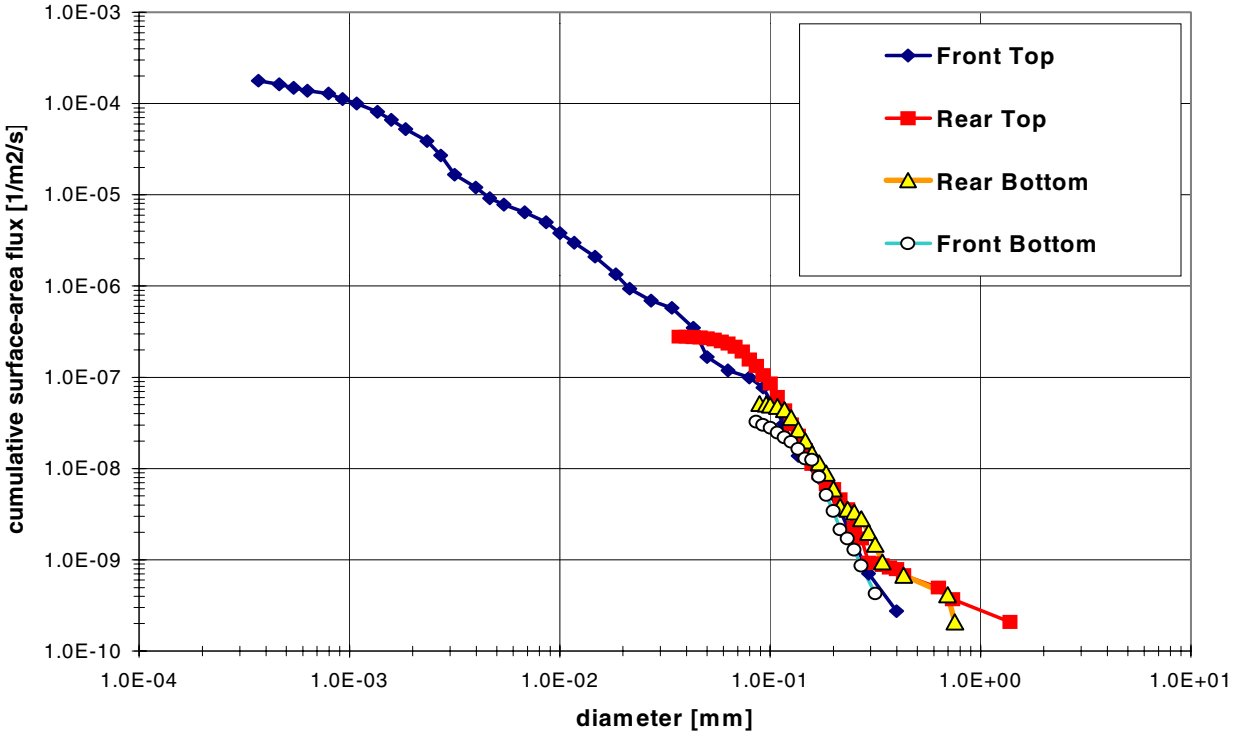

Figure 2-4: HST-SA cross-sectional flux.

2.1.6 The European Retrievable Carrier

EuReCa (international designator 1992-049B, catalog number 22065) was launched in August 1992 aboard STS-46 and retrieved in June 1993 by STS-57. During its 11-month mission, EuReCa was placed in a Sun-pointing mode with an inclination of 28.5 deg at altitudes between 502 and 508 km (Drolshagen et al. 1996). The post-mission analyses results are published in two Unispace reports. Interpolation of hypervelocity data into thin surfaces was used to relate impact crater diameters to particle diameters. Two fluxes, based on different assumptions of the projectile mass densities and impact velocities, are available from the reports. The first one assumes a projectile density of 4 g/cm^3 and an average impact velocity of 10 km/sec ("debris") while the second flux assumes a projectile density of 2.5 g/cm^3 with an average impact velocity of 21.4 km/sec ("meteoroid"). Figure 2-5 shows the two cross-sectional fluxes.

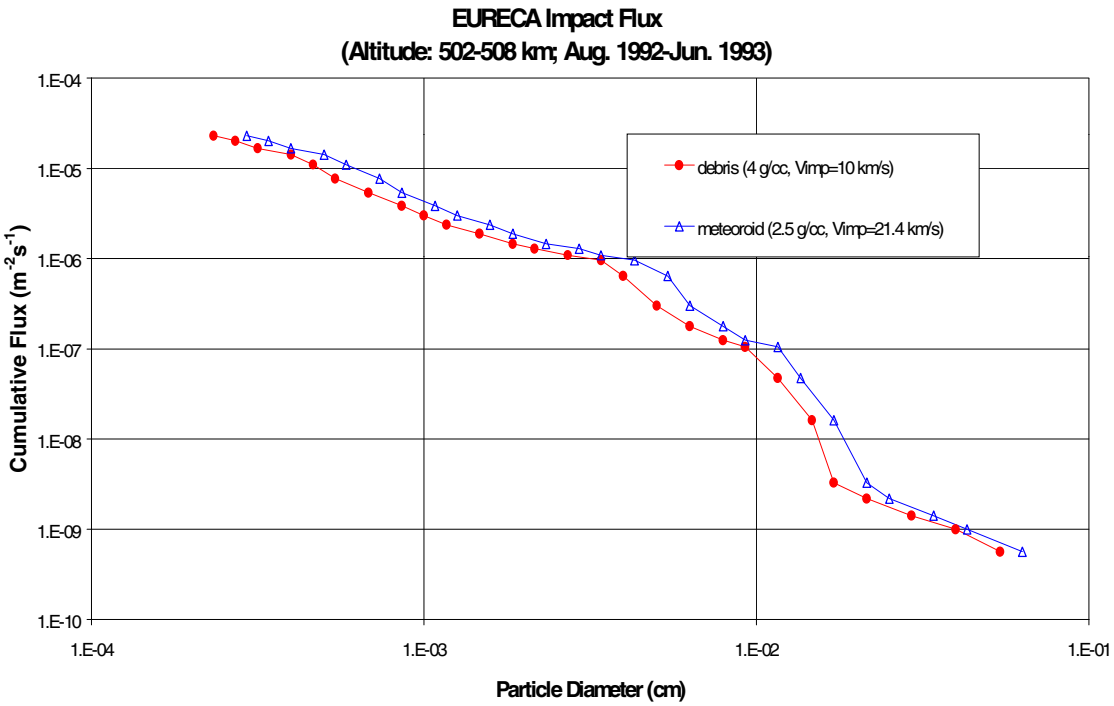

Figure 2-5: EuReCa measurements.

2.1.7 Space Transportation System (STS) Orbiter

The Shuttle data consist of careful analysis of the important surfaces after a mission. These surfaces are the wing leading edge reinforced carbon-carbon tiles, the payload bay door flexible reusable surface insulation, the payload bay door radiators, and the crew module windows. Sometimes, it is possible to identify the source of the debris—whether meteoroid or human-made. The available data includes STS flights 71, 76, 79, 81, 84, 86, 89, and 91 (Hyde et al. 2000a) and STS flights 50, 56, 72, 73, 75, 77, 80, 85, 87, 88, 94, 95, and 96 (Hyde et al. 2000b). Note that these references contain detailed descriptions of the data sets, including feature-by-feature size and impactor chemistry of each (if available) for each surface and mission. The documents also contain a summary of cratering equations. In addition, the detailed flight geometry is computed for each mission and the pointing history of each surface, complete with shadowing by other surfaces. The predicted hit rate according to ORDEM96 (Kessler et al. 1996) and the meteoroid model is computed for each surface and summarized in the document, and the detailed time-integrated orientation information for each surface is saved in special files. A large amount of hypervelocity data exist for hypervelocity impacts into glass surfaces, and was used to relate crater diameters to particle diameters for the Shuttle windows; however, other surfaces are very complex (tiles, radiators, etc.), and required special impact tests to determine impactor sizes. Details on the hypervelocity impact relations are described in Christiansen (1998).

2.1.8 The Goldstone Radar

NASA Jet Propulsion Laboratory's Goldstone radar system consists of a bistatic pair of parabolic antennas located 497 m apart. The 70-m antenna is used for the transmitter and the 35-m antenna is used for the receiver. The transmitting antenna points 1.5 deg from zenith at azimuth 154.6 deg toward the receiving antenna. The receiving antenna points 1.44 deg from zenith so that the two beams overlap between about 280 and 3000 km altitude. The radar has a wavelength of 3.5 cm, and can see objects down to 2 mm in size in LEO (Goldstein et al. 1998, Matney et al. 1999).

The Goldstone data sets consist of debris detections over a period from October 1994 to October 1998. Table 2-4 summarizes the observation hours and number of detections. Due to reduced sensitivity in the 1998 data and some of the 1997 data, only a subset of the data summarized in the table was actually used in the analysis.

Table 2-4: Goldstone Radar Observations

Year	Observation Hours	Number of Detections
1994	23.2	696
1995	7.5	218
1996	43.0	1485
1997	107.4	2934
1998	172.2	3785

The receiver only detects signal in the principal polarization channel, so only a portion of the reflected radar energy is measured. This will result in some underestimation of an object's RCS. An adjustment factor was added in the calculations based on polarization distributions measured by Haystack.

There appears to be a saturation problem at large RCS values. This means that the radar probably underestimates the RCS of larger objects (>>1 cm), but should not interfere with measurements of the smaller objects. Nor should it affect the cumulative flux rate determined at small sizes.

Reconstructing the size-dependent flux for Goldstone is a difficult process because the overlapping beams create a complicated beam pattern. In addition, while there is some information in the range-rate data, it is difficult to extract accurate inclination values because the beam direction is nearly vertical. The biggest drawback is the lack of detailed information about how each object went through the beam. The RCS is computed as if each object went through the center of the beam where the radar signal is the strongest. This means that the quoted RCS is a lower limit. For this reason, ORDEM2000 uses the Goldstone data as a secondary source to

validate the model. The model fluxes are used to "fly" various debris sizes randomly through the overlapping Goldstone beams using a Monte Carlo technique. For each path and size, an "equivalent RCS" value is computed—the RCS value Goldstone would have assigned to that object. Once a predicted "equivalent RCS" distribution is computed, it can be compared directly with the data.

Table 2-5 shows selected Goldstone data. All data sets are in the form of "Events" files that preserve the time, range, range-rate, and RCS (the value measured by Goldstone) of the individual detection for all the observation periods.

Table 2-5: Selected Goldstone Data Showing Time of Detection, Range, Range-Rate, and RCS in Square Millimeters

YY	DOY	Date	Det#	Time (GMT)	Time	SNR	Rng (km)	Vel (km/s)	Sqmm	Diam (mm)	Hits
94	291	17-Oct	1	7.4039	7:24:14	22.23	828.4	0.029	0.1878	3.13	2
94	291	17-Oct	2	7.4075	7:24:27	12.8	2877.6	0.2551	45.8401	7.83	6
94	291	17-Oct	3	7.4214	7:25:17	23.59	1200.5	-0.1066	1.0789	4.19	4
94	291	17-Oct	4	7.4222	7:25:20	22.98	2791.4	0.0679	53.8642	8.28	4
94	291	17-Oct	5	7.4292	7:25:45	18.44	2829	-0.1115	48.7153	7.91	5
94	291	17-Oct	6	7.4464	7:26:47	10.45	821.8	-0.1559	0.1017	2.83	4

2.1.9 The Space Flyer Unit

The Japanese SFU (international designator 1995-011A, catalog number 23521) was launched on 18 March 1995 from the National Space Development Agency Tanegashima Space Center aboard their third H-II launch vehicle. The initial checkout orbit was a 330-km altitude circular orbit at approximately 28.5-deg inclination. After the solar array paddles were deployed and the portions of the spacecraft bus were checked out, the on-board engines fired five times to raise the spacecraft to its 480-km circular operational orbit, which was achieved on 23 March 1995. The STS-72 crew retrieved the SFU on 13 January 1996.

The spacecraft is shown in Figure 2-6; during the majority of its operational mission, the spacecraft was oriented such that the solar array paddles pointed at the Sun while the –Y solar array paddle always pointed to the northern celestial hemisphere and the +Z face preferentially pointed in the direction of the Earth's heliocentric motion, i.e. the apex direction. The exception to this general orientation was during the operational period of the onboard Infra-Red Telescope in Space experiment. The experiment period extended from 29 March to 26 April 1995, during which the spacecraft was oriented to point at celestial targets. However, in general, surfaces may be assumed to be tumbling with respect to the local velocity vector.

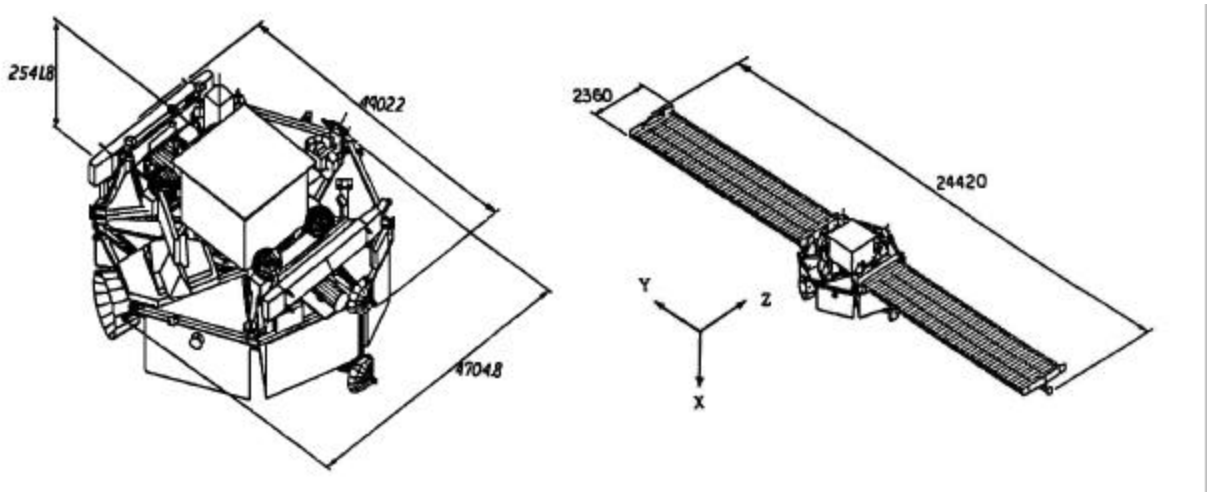

Figure 2-6: The SFU spacecraft. All dimensions are in millimeters.

The total exposed area was approximately 146 m^2. The solar array paddles were covered with solar cells, while the majority of the spacecraft exposed surfaces were covered with MLI composed of an aluminized Kapton polymide outer layer or silverized Teflon thermal control radiators. That portion of the spacecraft which has been examined (Kuriki et al. 1997) is the exposed facility flyer unit, which structurally forms the core of the spacecraft and constitutes a radiator for the spacecraft. The exposed facility flyer unit surface area exposed to space is approximately 2.19 m^2. This surface is composed of second surface mirror silverized Teflon tape attached to Al 2024-T81 plate (Yano 1999). Figure 2-7 shows a cross section of this surface.

Data analyzed in this report are drawn from Kuriki et al. (1997). Yano (1999) has conducted and reported more extensive data analyses, incorporating not only the exposed facility flyer unit set but also surface and MLI impact data. Since these data were unfortunately unavailable for analysis during this work, we will not analyze them in this report. However, the reduced data are consistent with the LDEF average flux, the HST, and EuReCa data sets.

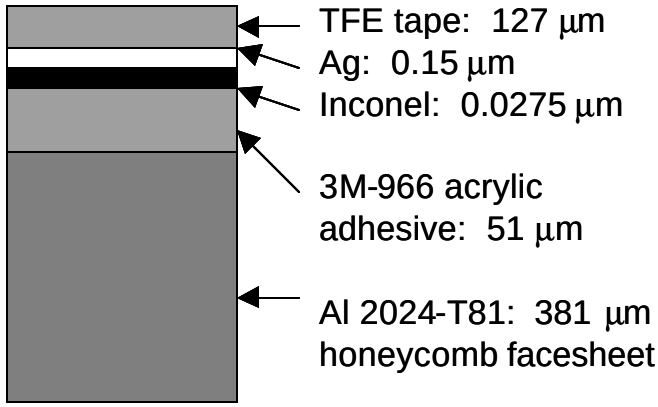

Figure 2-7: Exposed facility flyer unit cross section (not to scale; some layers accentuated).

2.1.10 *Mir*

2.1.10.1 Orbital Debris Collection (ODC) Experiment

The ODC experiment [Hörz et al. 1999] was one of four components of the *Mir* Experiments Exposure Package (MEEP) experiment managed by NASA Langley Research Center. Astronauts deployed this experiment by extravehicular activity conducted during the STS-79 mission to *Mir* and retrieved it by extravehicular activity during the STS-86 mission. Physically, the MEEP was attached to the Kristall module's docking module. Other components of MEEP were the Langley polished plate meteoroid detector (PPMD) and the NASA Marshall Space Flight Center's passive optical sample assembly (POSA) I and II. The ODC, PPMD, and POSAs I and II were contained in four separate passive experiment carriers. The passive experiment carriers allowed packages up to $62 \times 62 \times 8$ cm to be installed.

The POSA experiments exposed various materials—including paint, glass coatings, MLI, and metallic samples—to the space environment. PPMD exposed gold, zinc, and aluminum plates to the environment in a manner similar to POSAs I and II and previous flight experiments such as the LDEF. In contrast, the ODC used 0.02 g/cm^3 mass density silicon dioxide (SiO_2) aerogel (produced by NASA Jet Propulsion Laboratory) to decelerate impacting particles within the material, allowing for extraction and elemental analysis as well as impact trajectory assessment. Aerogel tiles ($9.6 \times 9.6 \times 1.1$ cm) were press-fit into an aluminum frame within the passive experiment carrier. Two frames, similar to the leaves of an open book, compose the ODC; each frame possesses an effective exposed area of ~ 0.319 m^2.

The ODC was deployed such that frame 1 nominally faced into the ram direction while frame 2 faced into the anti-ram (or wake) direction. However, due to maneuvering during MEEP deployment, actual pointing of the ODC relative to the *Mir* velocity vector is poorly understood. Also, shielding by adjacent structures is poorly understood and hence not properly incorporated into the analysis at this time. Maneuvering tends to randomize orientation with respect to the ram direction, lending to the ODC the character of a randomly tumbling plate. Shielding also tends to enhance the pointing uncertainty, and its concomitant uncertainty in flux estimation, because a shielded orientation can mimic a much less active orientation. In other words, were the ODC to be oriented at or near the ram direction and yet shielded by adjacent components, the number of impacts could be similar to that observed in the wake orientation.

Following retrieval after 553 days of exposure, the ODC was returned to JSC for analysis in October 1997. It was disassembled in the Facility for the Optical Inspection of Large Surfaces and approximately 0.106 m^2 of each was analyzed. Frame 2 had an enhancement, attributed to a swarm of particles. This was identified by uniformity of impact direction in the aerogel, and may be due to secondary ejecta created by an impact on a nearby surface.

With the swarm particles removed, frame 1 and 2 results are statistically identical. The swarm particles, however, dominate below approximately 15 μm. The similarity between frame 1 and 2 results for larger sizes (and all sizes if the swarm particles are removed) lends further credence to the tumbling plate approximation to the ODC's orientation.

2.1.10.2 Other Mir*-Based Impact Experiments*

In addition to the ODC experiment, the *Mir* station has hosted three other particle-impact surface collectors (Mandeville and Bariteau 2000): the "Echantillons" experiment, the European Space Exposure Facility (ESEF), and the Particle Impact Experiment (PIE). Echantillons was a component of the Aragatz experiment, and was attached to the *Mir* main core module for 13 months, beginning in December 1988. ESEF was mounted externally on the Spektr module as part of the *Euromir 95* measurement campaign. PIE was attached externally to the Kvant-2 module from June 1996 to April 1997. These experiments exposed areas of 750, 400, and 665 cm^2, respectively. These experiments, necessarily like the ODC, were similarly plagued by uncertainty in orientation direction.

Mandeville and Bariteau (2000) compare the flux of microparticles measured by these experiments with that recorded by the MEEP/PPMD experiment (Humes 1998). With the exception of PIE results, Aragatz, ESEF, PPMD, and LDEF (averaged over azimuth in the LDEF local horizontal plane) display similar results for crater diameters >50 μm. Below this diameter threshold, ESEF (generally nadir-facing) flux tends to fall off while both Aragatz and PIE exceed that of the remaining instruments by approximately an order of magnitude. Some portion of this apparent excess may be explained by secondary ejecta from a nearby solar array. Short-term population enhancement measured by PIE may be indicative of passage through a relatively fresh debris cloud (Maag 1996).

2.2 Data Analysis

2.2.1 The Maximum Likelihood Estimator (MLE)

Data obtained from instruments do not usually contain all the information desired. This is especially true of orbital debris. Returned surfaces give crater distributions on oriented surfaces, but they do not reveal whether a fast, small particle, or a slower, larger one made a particular crater. The Haystack debris detections are not of sufficient quality to determine the particle's eccentricity accurately. In addition, these measurements represent statistical samplings of the population, and are thus subject to sampling error.

In the case of orbital debris, we know that the population to be measured consists of subpopulations in different types of orbits. If the parameter space to be measured is carefully chosen, then each of the subpopulations has a unique "fingerprint" in the measurement space. The measurements represent samples from superpositions or convolutions of these fingerprints weighted by the relative abundance of the individual subpopulations. This can be written

$$m(z)\,dz = \left\{ \int dx\; n(x)\; h(z \mid x) \right\} dz$$

where m(z)dz is the distribution in the measured parameter z, n(x) is the distribution in populations x, and h(z|x)dz represents the probability that an object in a given population x will be seen with a given detection parameter z—the so-called instrument response function. This type of equation is a Fredholm integral of the first kind. For convenience, this equation can be approximated by a discrete form

$$m_j = \sum_i n_i \, h_{ij}$$

where each i represents a binned population.

In both sets of equations, the "m" distributions are measured, the "h" functions are computed using theoretical knowledge of the instruments and physics (e.g., cratering), leaving only the solution of the "n" distributions—the actual populations desired. Unfortunately, the direct inversion or deconvolution of this equation is generally very difficult. In addition, the limitations of statistical sampling make the direct solution impractical. However, there are ways to arrive at statistical estimates for "n" that are just as useful as the elusive "right" answer.

This type of problem is known as LININPOS problems—linear inverse problems with positivity restrictions ("positivity restrictions" because all of the potential debris populations contain a number of members greater than or equal to zero). One type of solution is to find a distribution for n_i that maximizes (or minimizes) some measure of the goodness-of-fit. This is called the MLE approach (Vardi and Lee 1993). For systems such as this one, a good choice for the goodness-of-fit parameter is the Kullback-Liebler information divergence:

$$\sum_j \left\{ m_j \ln\left(\sum_i h_{ij} \, n_i \right) - \sum_i h_{ij} \, n_i \right\}$$

Functionally, this is equivalent to maximizing the sum of the logs of the Poisson probabilities (equivalent to the product of the probabilities):

$$\ln\left(\prod_j P\left(m_j \mid \sum_i h_{ij} \, n_i \right) \right) = \sum_j \ln\left(\frac{e^{-\sum_i h_{ij} n_i} \left(\sum_i h_{ij} \, n_i \right)^{m_j}}{m_j!} \right)$$

$$= \sum_j \left\{ m_j \ln\left(\sum_i h_{ij} \, n_i \right) - \sum_i h_{ij} \, n_i - \ln(m_j!) \right\}.$$

The MLE is computed using the EM method. This method is powerful because it is a simple iterative method that is easily programmed and linearly converges toward the best fit, although sometimes very slowly. The iteration starts with an initial guess $n_i^{(0)}$:

$$n_i^{(1)} = n_i^{(0)} \sum_j \frac{m_j\, h_{ij}}{\left(\sum_k n_k^{(0)}\, h_{kj}\right)}.$$

In order for this method to converge, h_{ij} needs to be normalized:

$$\sum_j h_{ij} = 1.$$

The effects of this normalization can be removed at the end of the computation.

For this analysis, we decided to bin the populations in a way to simulate the continuous character of the distributions. One way to do this is to use "hat" functions that, when added together, form a smooth distribution. These are good for any function that is believed to be highly variable, such as inclination distributions.

$$f(x) = \begin{cases} 0 & x \le x_1 \\ \dfrac{x - x_1}{x_2 - x_1} & x_1 < x \le x_2 \\ \dfrac{x - x_3}{x_2 - x_3} & x_2 < x \le x_3 \\ 0 & x_3 < x \end{cases}$$

Another basis set to use is a series of normal distributions offset by 1 σ

$$f_k(x) = \frac{1}{\sqrt{2\pi}\sigma} \exp\left[-\frac{(x - (x_0 + k\sigma)^2)}{2\sigma^2}\right],$$

where σ is the standard deviation of the normal distribution. While these basis functions may seem odd, they are very good at fitting functions that change smoothly over logarithmic scales, such as size distributions.

2.2.2 Primary Data

2.2.2.1 Space Surveillance Network

It is generally believed that the SSN catalog does not provide a complete coverage of objects all the way down to 10 cm in size in the LEO region. This can be seen from Figure 2-8. The cumulative size distribution (N_{cum}) of all LEO-crossing objects (from the SSN catalog at the beginning of 1999) as a function of diameter is shown as the top curve. When it is separated into two components (non-breakup and breakup), the level-off of the breakup fragment component just above 10 cm is a clear indication that the coverage is incomplete at 10 cm (due to the sensitivity limit of the radar). The characteristic of the level-off appears to be the same even

when the breakup fragment component is further divided into components with different altitude, eccentricity, and inclination (triangles and circles in Figure 2-8).

To account for the incompleteness problem, we apply a simple bias correction to the SSN catalog objects to form the 10-cm population. It is based on the following two arguments: (1) the current breakup fragments are dominated by explosion fragments, and (2) the size distribution of explosion fragments follows a simple power law that, when plotted on a logarithmic (N_{cum} vs. size) chart, mimics a straight line (Johnson et al. 2000). The ORDEM2000 10-cm population is obtained by increasing the contribution of catalog breakup fragment and real 8x,xxx objects by 13% to where the bias-corrected straight line intersects the 10-cm line (see Figure 2-8) plus all known non-breakup objects.

We take the ORDEM2000 1-m population directly from the SSN catalog without any modification.

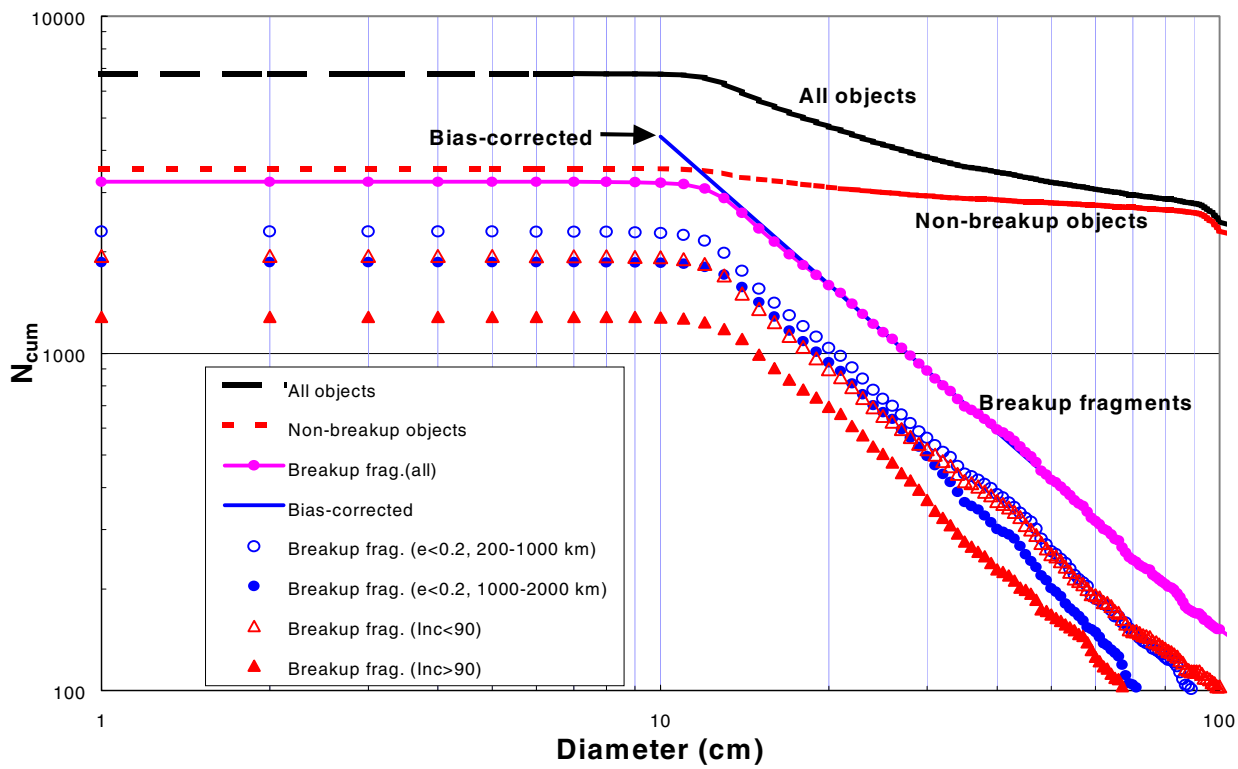

Figure 2-8: Cumulative size distribution of LEO-crossing SSN objects in 1999.

2.2.2.2 Long-Duration Exposure Facility

To transform the particle size and velocity into an equivalent crater size, we use the crater diameter equation of Cour-Palais (for this discussion, see Zhang and Kessler 1993):

$$P = 5.24\, D_p^{19/18}\, H^{-1/4} \sqrt{\frac{\rho_p}{\rho_t}} \left(\frac{v \cos\theta}{v_s} \right)^{2/3} .$$

In this equation, P is the crater depth (cm), D_p is the particle diameter (cm), H is the Brinell hardness of the target material, and ρ_p and ρ_t are the densities (g/cm^3) of the particle and the target surface. In addition, v is the speed of the particle, θ is the angle the particle strikes the surface relative to the local normal direction, and v_s is the sound speed in the material. We investigated a number of different equations in order to best fit the empirical data. Watts et al. (1993) have created a set of equations that describe penetration depth and crater width, but these equations were difficult to match up with data such as Hörz et al. (1995). Instead, we used the empirical data of Hörz et al. (1995) to arrive at reasonable crater depth/width (P/D_c) ratios.

Fortunately, for the modeling of the cratering on the surface of LDEF, the exact cratering formula is not nearly so critical as the choice of impact velocity and angle. As these angles and velocities are all computed in the EM algorithm (see Section 2.2.1), the results should closely reflect reality.

The cratering equation predicts the true crater diameter at the level of the pre-impact surface. Unfortunately, the vast majority of the LDEF data consists in the "lip" diameter of the craters—a value larger than the "true" crater diameter. Researchers (cf. Kessler and Zhang 1993) usually quote a ratio of lip diameter to crater diameter of ~4:3. There is some disagreement about this exact value in the sources, but these numbers appear to give good overall results for LDEF. Note that if the crater was elliptical such that two crater diameters were given, the crater diameter was assumed to be the average of the two values. Table 2-6 lists the material constants of the surfaces used for the calculation.

Table 2-6: LDEF Material Properties Used in the Computations

Material	Density (g/cm^3)	Sound Speed (km/s)	Brinell Hardness	P/D_c
Aluminum 6061-T6	2.7	5.1	95	0.58
Aluminum 1100	2.7	5.1	23	0.58
Aluminum 2024-T81	2.7	5.2	47	0.58
Gold (annealed)	19.32	3.24	25	0.4

For the LDEF EM fits, we divided the cratering population n_i into meteoroids and debris. Application of the meteoroid flux presented some difficulties. The Grün model (Grün et al. 1985) makes the assumption that the meteoroid velocities can be characterized by a single value—in this case 20 km/sec. While this may be adequate for randomly oriented surfaces, it does not work well when trying to apply the meteoroid flux to various oriented surfaces adding in the motion of the spacecraft and the effects of gravitational focusing. The solution chosen was to use the Grün mass distribution to define the relative flux of meteoroids as a function of mass, and use the NASA velocity distribution model (Kessler et al. 1991) to define the distribution in velocity in interplanetary space. We applied the effects of gravitational focusing and spacecraft motion using the Liouville's Theorem method of Matney (2000). Because the Grün mass

distribution was calibrated using a single velocity, we applied a single scaling factor to the Grün flux to adjust it for the NASA velocity model. This scaling factor was allowed to be adjustable during the fitting process until the best meteoroid fit was obtained. The fit to the space-facing face of LDEF as well as the other faces indicates this factor should be about 1.5. This means that, if a user wishes to use the Grün flux with the NASA velocity distribution, this velocity-dependent "Grün" flux needs to be multiplied by 1.5.

The true meteoroid velocity distributions are highly directional, relative to the motion of the Earth, but the NASA velocity model averages over all directions. Fortunately, the orbital motion of LDEF averaged over meteoroid directions such that the isotropic assumption is valid for this study.

The most difficult aspect of using the LDEF data is how to set up the problem in such a way as to infer debris fluxes at other altitudes than that sampled by LDEF. The first step was to "create" debris from sources—in this case, intact satellites from the SSN catalog.

We constructed a model in which the particles were "created" at a constant rate proportional to the area of the parent spacecraft and propagated (under the influence of atmospheric drag, radiation pressure, and gravitational perturbations) to see if they intersected the LDEF. If they did, the collision rate was computed. Using this method, the parameters to be fit are the debris size-dependent production rates at the parent spacecraft. There were a number of simplifying assumptions: all objects create particles at the same rate only proportional to the area of the parent, the production rate is constant with time, the particles all come off with similar densities, and they come off with minimal velocities. However, using these assumptions, one can construct a self-consistent model of the low-Earth small particle environment that projects the populations into regions which LDEF cannot directly sample.

The debris families were split into two populations: one of parents with high-eccentricity near-28-deg-inclination orbits and the other with all other satellites. We tried a number of other combinations, but this was the simplest combination that gave reasonable matches. These two populations were further subdivided into size families based on the "normal" basis functions described in Section 2.2.1.

We binned the crater data for m_j in crater size bins and LDEF experiment—12 intercostals, 12 longerons, 14 Humes plates (including space-facing and Earth-facing surfaces), CME aluminum, and two CME gold plates (one for debris and one for meteoroids). We assume all craters on the space-facing and Earth-facing Humes plate to be meteoroids only. The m_j bins were compiled to represent the cumulative numbers—the number of craters of the given size and larger. This procedure is necessary to ensure the EM method fit cumulative distributions.

We had to choose a mass density for the meteoroid and debris particles to use in the cratering equations. The meteoroids were assumed to have a density of 2.5 g/cm^3, and the debris particles were assumed to have aluminum densities of 2.8 g/cm^3. The velocities of the meteoroids ranged from 0 to 72 km/sec outside the Earth's gravitational field.

The modeled debris populations were computed with sizes between ~1 µm and ~2000 µm, although for the model we rejected the highest and lowest size values—the highest because of lack of detections, and the lowest because they were too small to produce craters in the size range observed. The result of the MLE procedure was a production rate that can be applied to all objects in Earth orbit to project into regions and times in which LDEF did not observe. It also gives an estimate of the high-eccentricity to low-eccentricity ratio and the inclination distributions for smaller particles.

Figures 2-9 to 2-14 summarize the fitting results to the LDEF crater distributions. Figure 2-9 gives the measured crater distributions on the space-facing Humes experiment, thought to consist only of meteoroid hits. The fitted curve shows the Grün meteoroid flux with the NASA velocity distribution after the fitting factor of 1.5 has been applied.

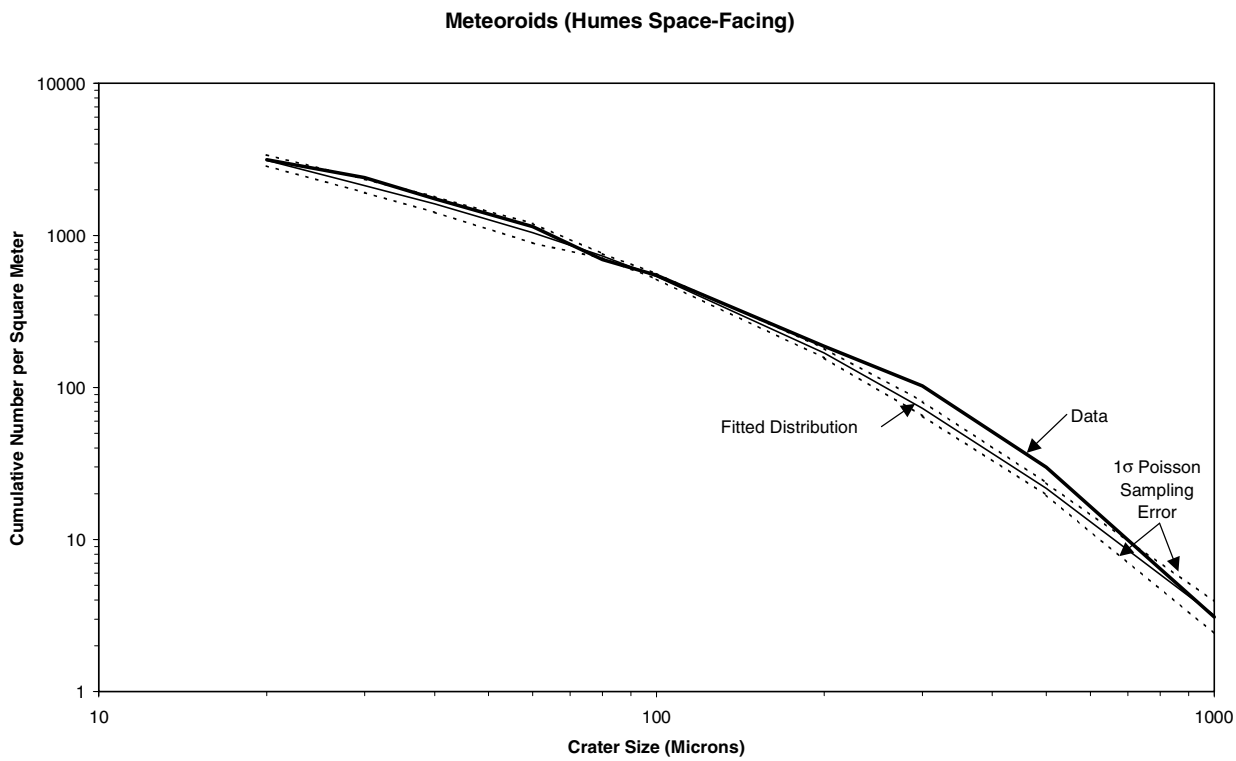

Figure 2-9: Crater feature distribution on the space-facing Humes surface along with the LDEF meteoroid fit. This fit was derived by using the Grün mass flux distribution combined with the NASA velocity distribution and solving for the Earth's gravitational focusing and the motion of the LDEF spacecraft. In order to fit the data, this "modified" Grün distribution was multiplied by a factor of 1.5.

Figures 2-10 and 2-11 show examples of the fits to the Humes and intercostals surfaces as a function of yaw angle. Figure 2-12 shows the fit to the CME gold surface split out by craters that were debris only and those that were meteoroids only (meteoroids + unknowns). Figures 2-13 and 2-14 show the overall fit to the CME aluminum surface. Figure 2-14 shows the data broken out by debris only and debris plus unknowns. The true number of debris hits is somewhere between these two extremes. The fitted debris population clearly lies between these two extremes. In addition, it appears that the largest "unknown" craters are due to debris, while the smallest "unknown" craters appear to be dominated by meteoroids.

In summary, we were able to make reasonable fits to a number of different surfaces, some with quite different material properties, over a wide range in feature size using a minimal number of fitting assumptions. In the process, we were able to establish a reasonable distribution of small particles over a wide span of orbital parameters and altitudes.

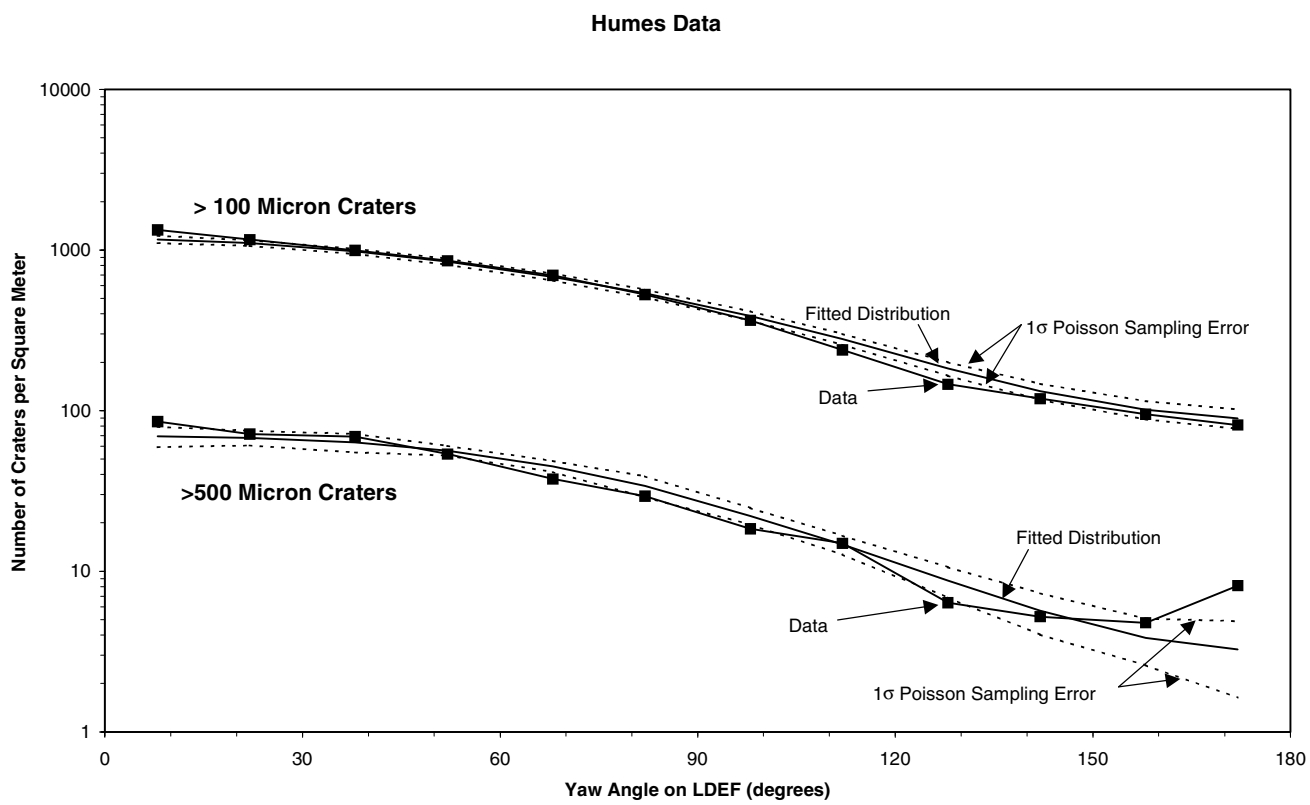

Figure 2-10: Crater feature distributions at two different limiting sizes on the various Humes surfaces along the LDEF sides as a function of yaw angle. Both the fit and the data represent a mix of meteoroids and debris.

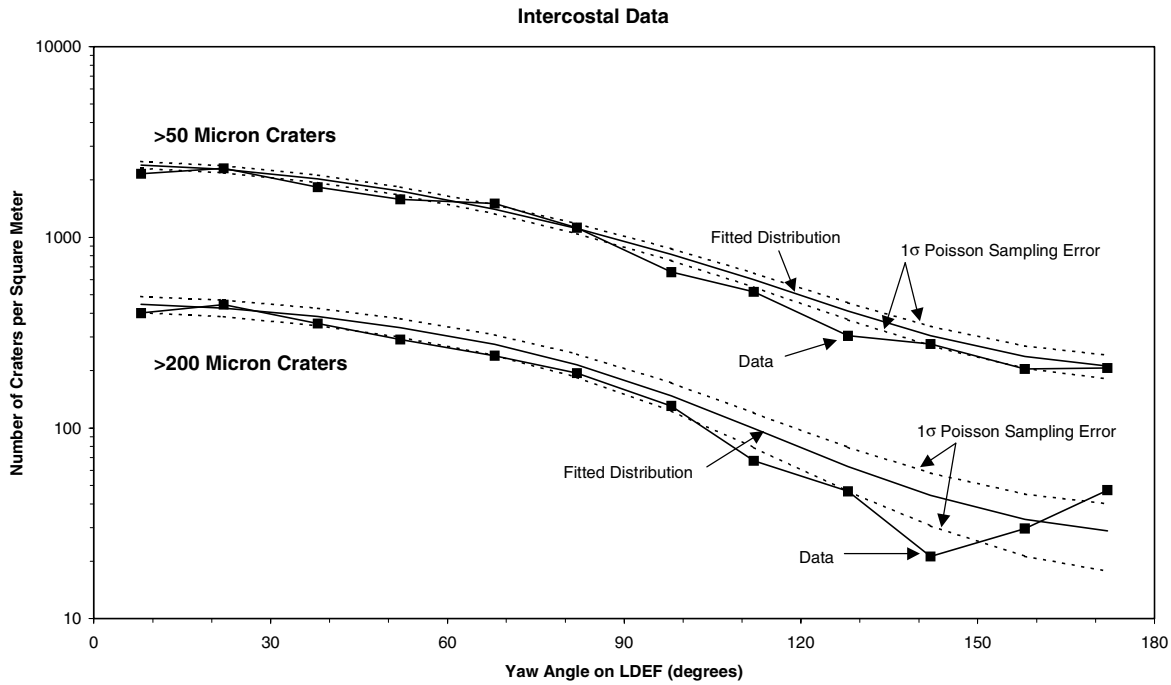

Figure 2-11: Crater feature distributions at two different limiting sizes on the various intercostal surfaces along the LDEF sides as a function of yaw angle. Both the fit and the data represent a mix of meteoroids and debris.

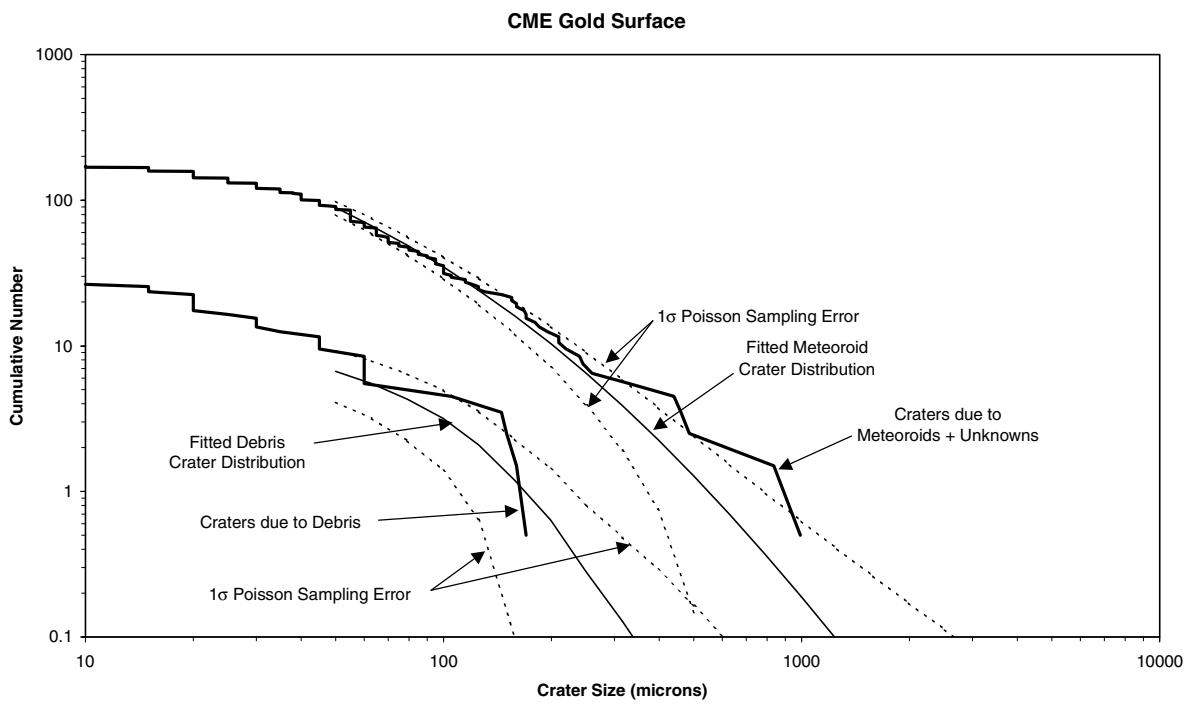

Figure 2-12: Crater feature distributions on the CME gold surface on the rear side of LDEF broken out by craters made by debris only and meteoroids only (meteoroids + unknowns). This is the only LDEF surface that can unambiguously determine between meteoroids and debris (based on reasonable assumptions). The fitted curves are also shown for debris only and meteoroids only.

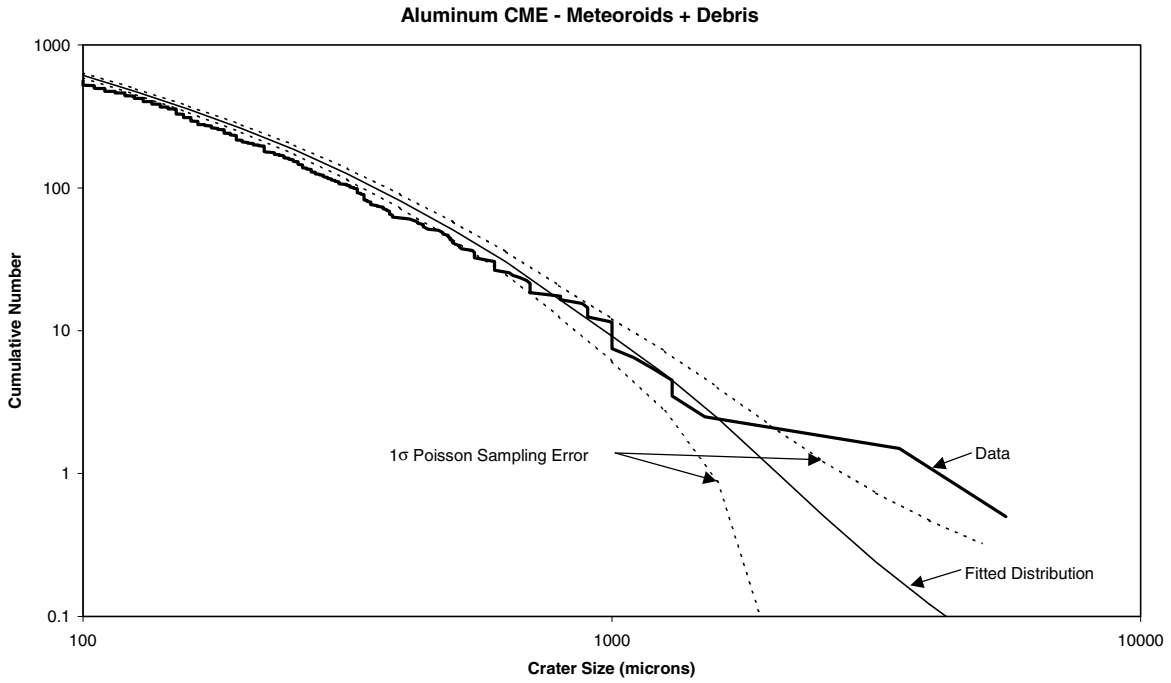

Figure 2-13: Total crater feature distributions on the CME aluminum surface compared to the fit.

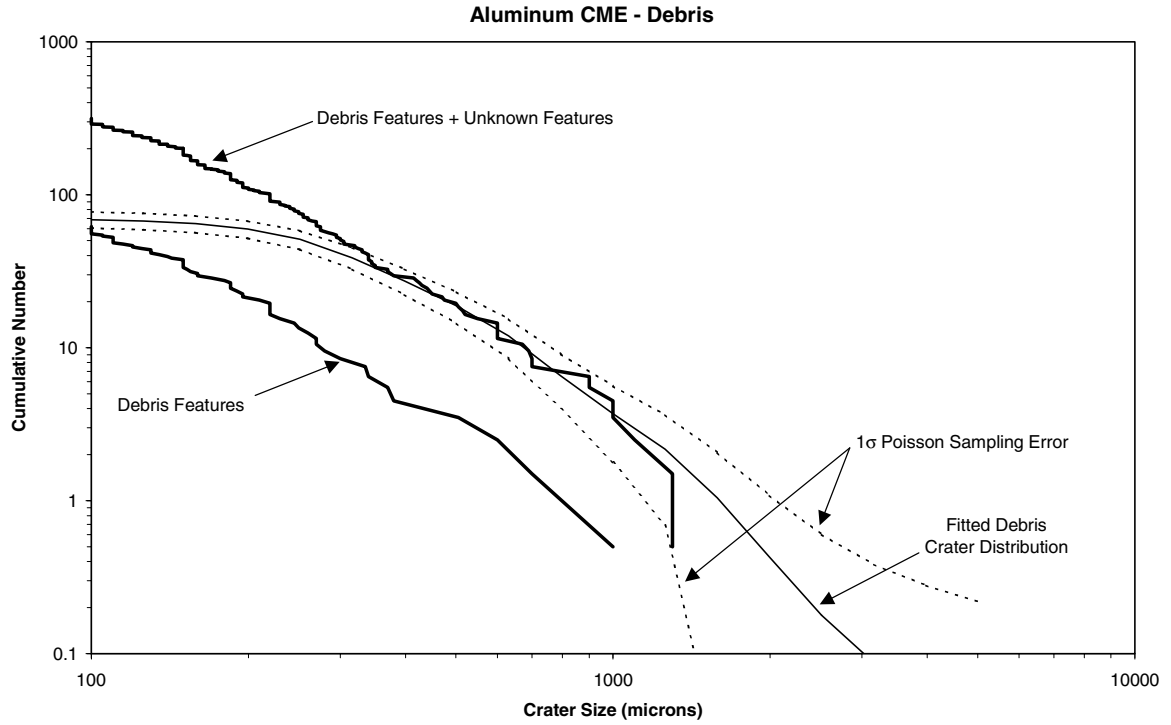

Figure 2-14: On the CME aluminum surface, craters identified as "unknowns" could be due to either meteoroids or debris. The true debris crater distribution should lie somewhere between "debris only" and "debris + unknowns." As can be seed in this figure, the fitted debris distribution stays between these two extremes. The fit also implies that the largest "unknown" craters are caused by debris, but the smallest ones are dominated by meteoroids.

A few comments need to be made at this stage concerning mass density of small particles. The populations derived from LDEF were computed by assuming the debris are aluminum spheres with mass density of 2.8 g/cm^3. Thus for applications using ORDEM2000 (e.g., penetration risk calculations), the particles should be assumed to be aluminum spheres. While this choice is somewhat arbitrary, as long as similar assumptions are used to convert the fluxes based on size into damage, the assumptions should give reasonable results.

2.2.2.3 Long-Range Imaging Radar ("Haystack")

For the Haystack data, the populations to be fit consisted of distributions in perigee altitude, eccentricity, and inclination. The 75-deg east stare mode can distinguish inclinations between about 42-deg and 138-deg inclination. The 10-deg and 20-deg south stare modes can distinguish orbits with inclinations down to about 25 deg and up to about 155 deg (the exact value varies with altitude), but the south stare modes cannot distinguish between inclinations and the supplement of the inclination (180 deg minus the inclination). Under the assumption that the 1-cm population imitates the gross orbital distributions of the catalog population, then the populations in inclination can be limited further. The population actually computed was based on the following orbit families:

25 deg < i < 42 deg, perigee altitude < 1275 km
42 deg < i < 121 deg, perigee altitude < 2000 km

Orbits with inclinations in excess of 121 deg were simply assumed to not exist. The low inclination orbits are not assumed to be nonexistent, only unobserved. They are estimated and added to the model populations at a later stage.

The data sets consist of range and range-rate pairs for each of the Haystack pointing directions (for all objects with RCS values that indicated they were greater than or equal to 1 cm in size based on the SEM). This forms a very high-resolution data set (much higher than the crater data), so both the data and populations were binned into many segments. The number of bins created problems in terms of the EM matrix size and run time, but yielded useful results.

The calculations showed a number of populations derived from the Haystack data. There are high-eccentricity populations at low inclinations, and concentrations of circular orbits at 28-deg, 65-deg, 82-deg, and 100-deg inclination. These populations are consistent with those derived from earlier analysis of the Haystack data and consistent with our current knowledge of the environment. This method gives the first analytical values for the ratio of elliptical to circular orbit populations in the 1-cm size range.

Figures 2-15, 2-16, and 2-17 show comparisons of the distributions estimated from the Haystack data with the catalog populations.

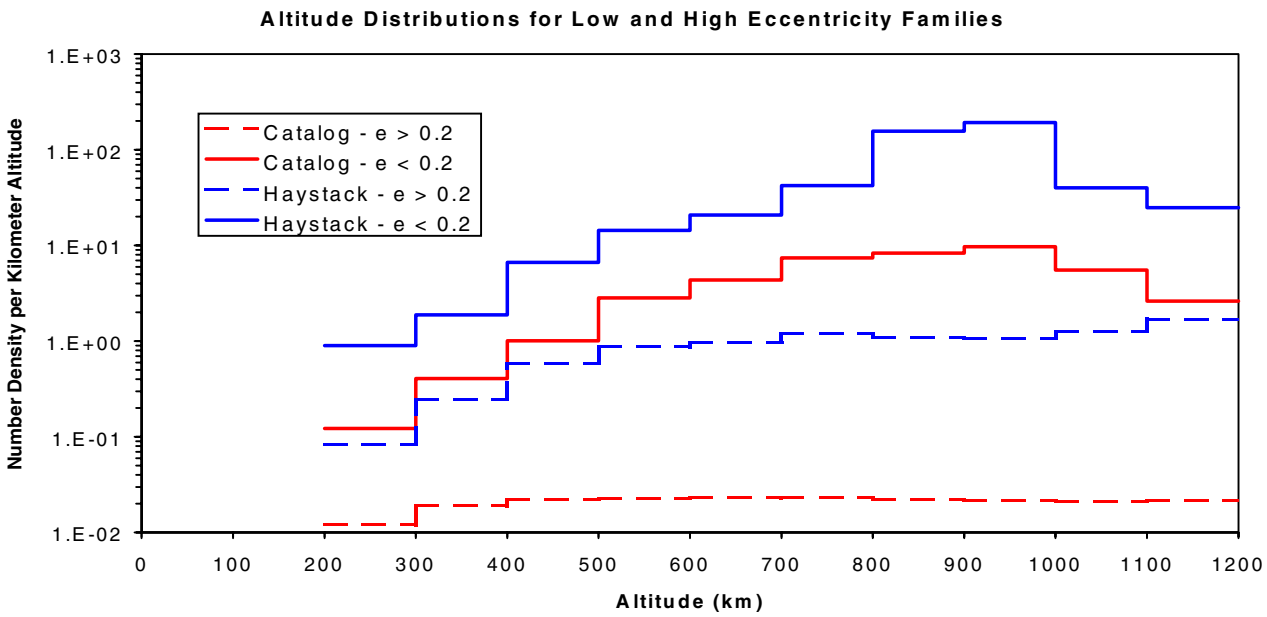

Figure 2-15: The orbit families estimated from the Haystack data using the EM method have been broken out by eccentricity and the spatial density with altitude is shown in comparison to the equivalent populations in the catalog. Note the high population of circular orbits between about 800 and 1000 km altitude in the low-eccentricity population. This is thought to be composed of RORSAT sodium-potassium debris and is a dominant feature in the Haystack data.

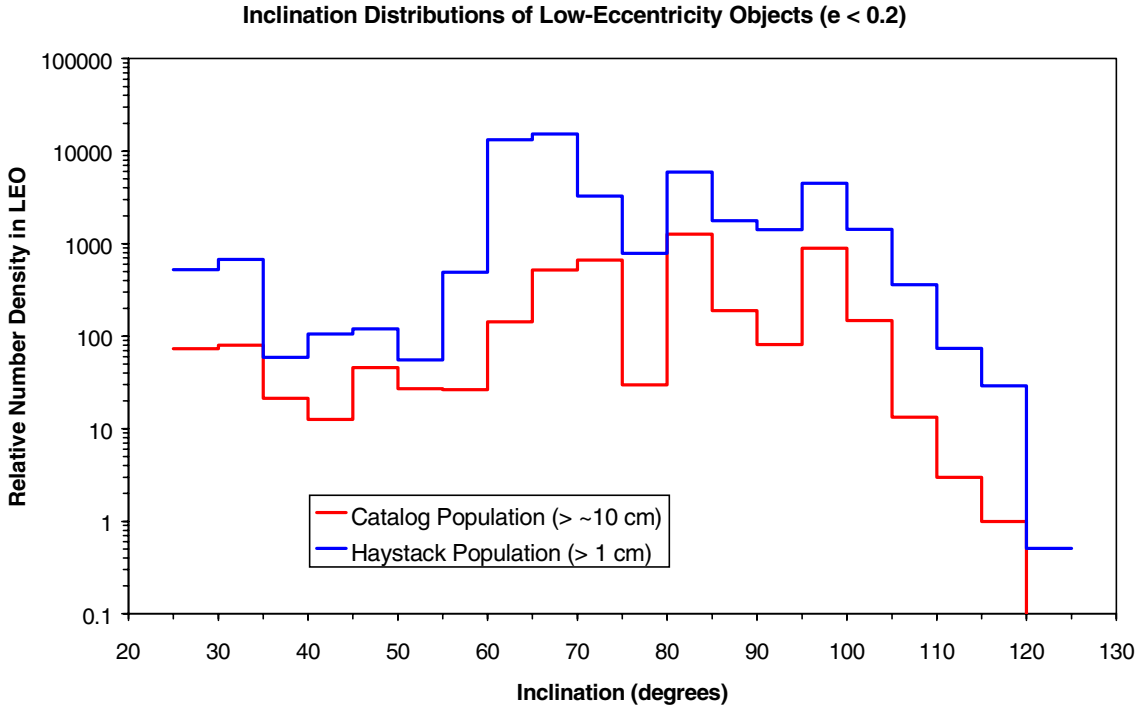

Figure 2-16: The orbit families estimated from the Haystack data have been broken out by inclination for the low-eccentricity population. Again note the RORSAT sodium-potassium population centered at 65 deg inclination in the Haystack data.

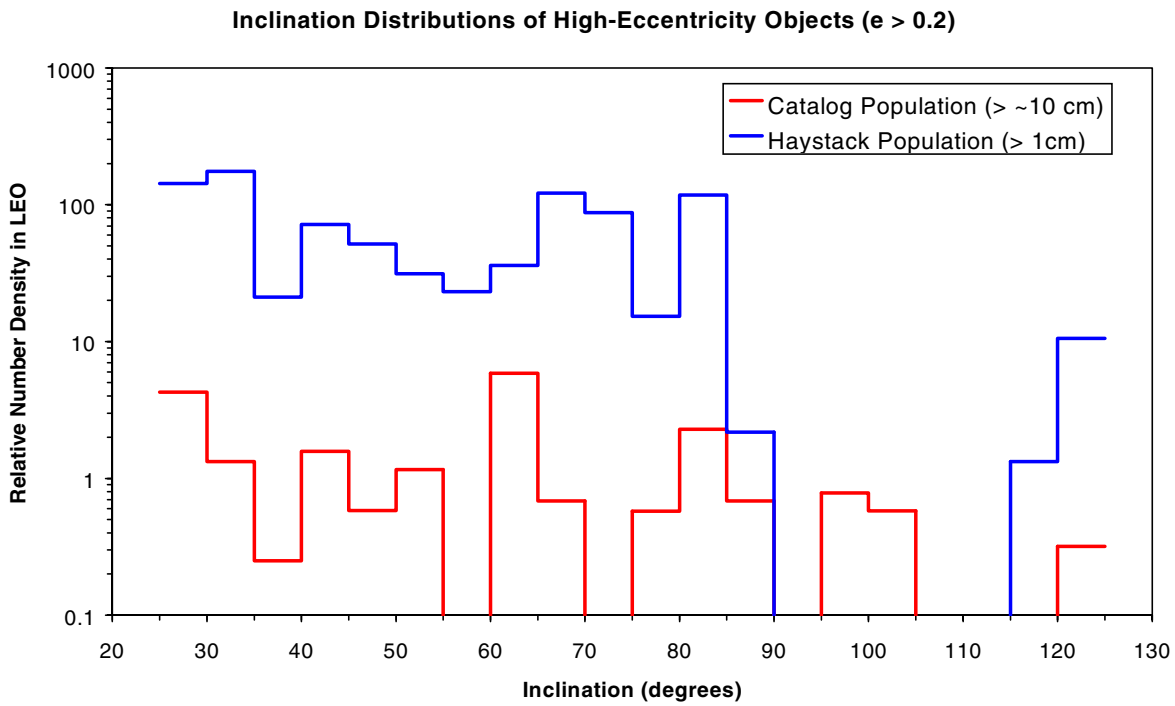

Figure 2-17: The orbit families estimated from the Haystack data have been broken out by inclination for the high-eccentricity population. The 1-cm Haystack population shows a relatively high relative population of elliptical orbits, especially at low inclinations.

2.2.3 Secondary Data

We used the secondary data sets to take the size orbit populations determined by the primary data set and make any necessary adjustments to modify the model to more closely reflect reality.

2.2.3.1 Shuttle Data

There are two ways to analyze cratering data. One is to try to back out a population using averaging techniques to remove the effects of velocity and size. The other is to use a model flux population, complete with details of velocity and direction, and to try to match the feature distribution on the target. This is the procedure we used to analyze the data sets.

The ORDEM2000 environment based on the primary data was carefully run against all the Shuttle missions in the study. Using the detailed pointing timelines and the cratering equations provided with the data, it was possible to make detailed predictions of the feature distributions seen in the Shuttle data. It soon became clear that the population of small particles derived from LDEF was underpredicting the feature distributions seen in the Shuttle data.

This presented a quandary. The populations were derived from a specially designed experiment to measure the orbital debris environment in the late 1980s, and a data set taken over multiple periods in the 1990s was giving significantly different results. In addition, the Shuttle data represented a data

set that closely resembled the true risks posed by the debris environment. We chose to stay with the inclination and eccentricity distributions fit by LDEF and to alter the spatial densities to reflect the higher numbers seen in the Shuttle data. Table 2-7 summarizes the population adjustment factors. Note that the best fits were found by adjusting only the high-eccentricity orbit populations.

Table 2-7: Table of Values Used to Adjust the Environment Based on the STS Data Fits

Population	Adjustment Factor
10 µm, high-eccentricity	35
10 µm, low-eccentricity	1
100 µm, high-eccentricity	10
100 µm, low-eccentricity	1
1 mm, high-eccentricity	6*
1 mm, low-eccentricity	1

* The 1-mm corrections are applied after the 100 µm populations are adjusted and the interpolation is computed.

There are many possible explanations for the discrepancies, but for the purposes of the model, it was simply assumed that the small-particle production rate in highly eccentric orbits went up in the 1990s. As will be seen in Section 4, this procedure provided results consistent with a number of different experiments.

2.2.3.2 The Goldstone Radar

To a first approximation, we compute the 1-mm populations by simple interpolation between the 1-cm and 100-µm fluxes—interpolating the orbit distributions linearly, and the spatial densities logarithmically. However, the Goldstone data provide a method to check these numbers.

We used the method described in Section 2.1.8 to compute predicted RCS distributions (values of RCS that Goldstone measures) for various altitudes. We then adjusted the interpolation values for the 1-mm population in order for the modeled distributions to fit the observed Goldstone distributions. For the most part, the only regions that needed adjusting were the RORSAT altitudes between 800 and 1000 km altitude. In the 1-cm population, these objects dominate the distributions. However, it appears that the population of RORSAT sodium-potassium particles falls into the background at around 1 mm. This may be due to the sublimation of the particles or their loss due to atmospheric drag.

The adjustments to these populations are summarized in Table 2-8. Note that the Goldstone data is the only data set used that samples the populations of particles in the approximately 2-6-mm range at these altitudes. The resulting fit is shown in Figure 2-18.

Table 2-8: Table of Values Used to Adjust the 1-mm Environment Based on Goldstone Data Fits

Altitude Bin	1-mm Population Adjustment Factor
800-850 km	0.5
850-900 km	0.25
900-950 km	0.25
950-1000 km	0.5

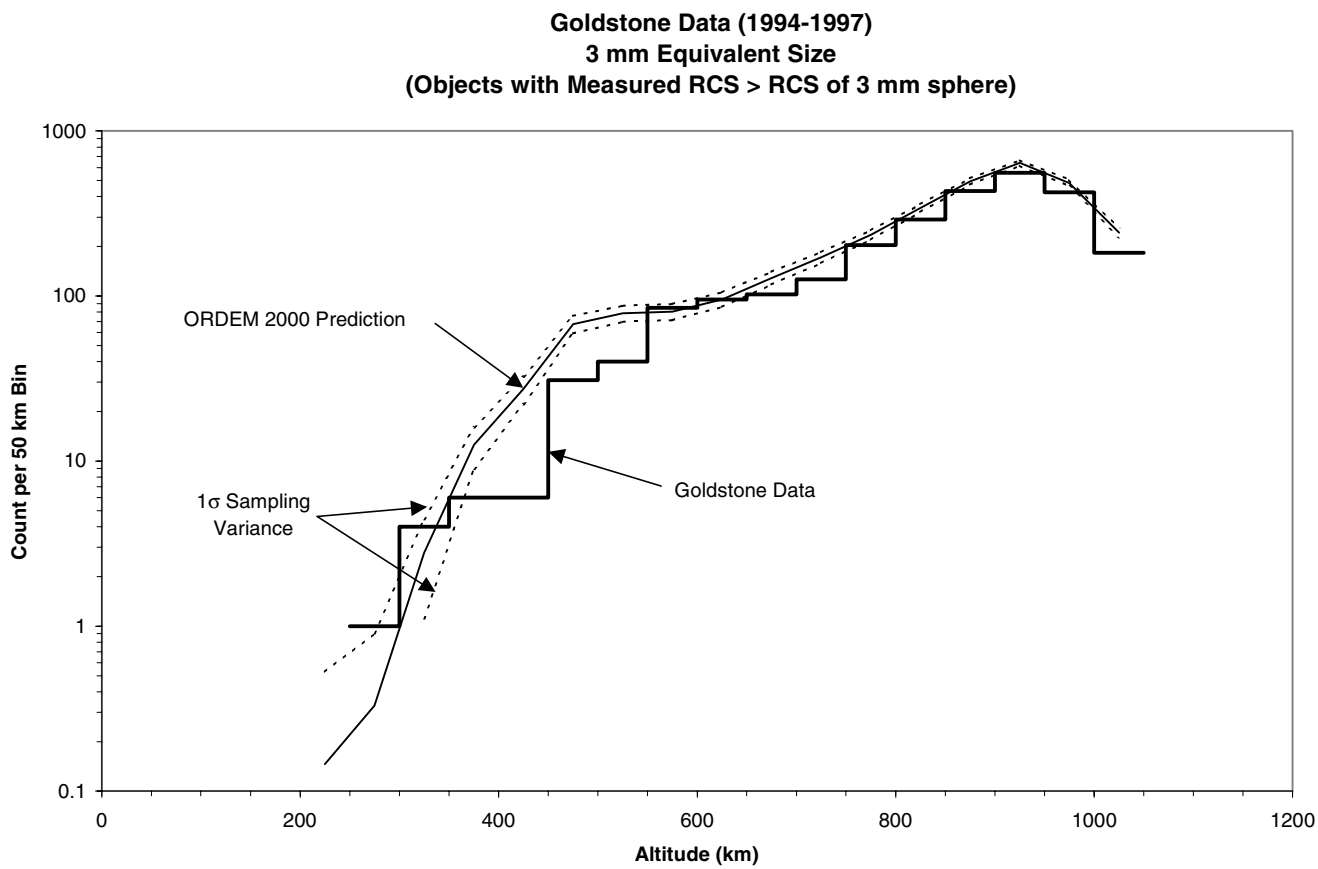

Figure 2-18: The Goldstone data give some indication of the populations of debris in the 1-mm to 1-cm size range. The ORDEM2000 prediction is based on a model of the Goldstone beam and represents the expected number of objects the radar would measure as having RCS values greater than or equal to that of a 3-mm sphere. Goldstone can only detect objects with this measured RCS out to about 1000 km.

2.2.3.3 HST Solar Array Data

We used original data taken from McDonnell et al. (1998b), consisting of tabulated values for a cumulative number of impacts, sorted by decreasing size of impact feature and the associated flux. The data have been repeatedly analyzed for different features, residue chemistry, etc. Comparison data are from the McDonnell et al. (1998a) Summary Report and from Drolshagen (personal communication, 1997), Drolshagen et al. (1997), and Paul et al. (1997). The latter three references were some of the first generally available to the scientific and engineering community. Analyses were conducted using, initially, the Cour-Palais (1982) relationship between conchoidal feature diameter (D_{co}) and the particle (impactor) diameter (d_p), and the Fechtig/Gault lunar rock impact equation (Fechtig et al. 1977; Gault et al. 1972). This latter relation was applied to the entire size spectrum of observed HST solar array impacts. McDonnel et al. (1998b) utilized the Taylor et al. (1998) damage equation for soda-lime and borosilicate glasses:

$$D_{co} = 10^{-0.21} d_p^{1.28} \rho_p^{0.44} v_p^{0.66} (\cos\theta)^{0.62},$$

where D_{co} is the conchoidal feature diameter (μm), d_p is the impactor diameter (μm), ρ_p is the projectile density (g/cm^3), v is the relative velocity (km/sec), and θ is the angle with respect to surface normal. Note that uncertainties in the exponents of the coefficient and variables have been suppressed here.

This equation is based on the assumption of a semi-infinite target. For HST-SA, this assumption holds for D_{co} less than about 300 μm. For larger sizes, the assumption of a semi-infinite surface fails. For features with D_{co} larger than about 2 mm, one can use a thin target assumption as described below. For intermediate feature sizes, no adequate cratering equation exists. Consequently, these data were not fitted.

Thin-target assumptions require two steps to elaborate the relationship between D_{co} and hole diameter D_h, and a relationship between D_h and d_p. The first is described in McDonnell et al. (1998a):

$$D_{co} = 1.080 D_h + 1.335,$$

where units of both the diameters are in (mm). This equation was fit to calibration shot data collected during the HST-SA analysis. Burt and Christiansen (2001) give the attendant relationship between D_h (mm) and d_p (cm):

$$d_p = 0.169(D_h + 0.169)\rho^{-1/3} v^{-2/3} (\cos\theta)^{-2/3} \quad .$$

Here, all variables are as defined before. This latter equation is derived from impacts onto actual HST-SA samples.

To present the least ambiguous analysis possible, all data analyzed are from the solar cell side of the flexible solar array. As European analysts have adopted a standard nomenclature, this

surface shall be referred to as the front-top surface, comprising the front of the solar array (i.e. the side mounting the solar cells), and the top array (the flexible array blanket which was on "top" of the bottom array when rolled within the array dispenser cassette. This strategy presented the best opportunity to readily analyze the data, and was representative of all four surface data sets as presented in McDonnell et al. (1998a,b).

As with the STS data, the detailed flux distribution on the HST-SA was integrated to give an estimate of feature distribution. We assumed the panels to be random-tumbling plates relative to the orbital debris environment. In addition, we looked into shadowing by the main body of HST, but this only altered the cratering flux by a small amount over the total solid angle. Unlike the STS data, there were insufficient chemical data to adequately remove meteoroid features. The resulting debris-only fits will underestimate the feature totals based on debris plus meteoroids. However, we will show in Section 4 that the results are adequate to demonstrate that the ORDEM2000 environment as modified by the factors above is consistent with this data set.

We looked into adding or subtracting the meteoroid environment based on the flux used for LDEF, but solar panels by their nature maintain a fixed or nearly fixed orientation with respect to the Sun. The meteoroid flux currently employed is based on the assumption of isotropic flux. This assumption is not accurate to describe the meteoroid flux in the near-Earth environment. For example, it is known there is an enhancement of meteoroid flux in the Sun/anti-Sun direction. In addition, we need to account for direction/velocity relationships. The isotropic meteoroid flux (as used for LDEF), applied to the HST-SA using gravitational focusing and spacecraft motion, gave meteoroid cratering fluxes higher than were seen for the complete debris plus meteoroid data. The actual meteoroid cratering flux on solar panels remains an open question at this stage.

2.2.3.4 The European Retrievable Carrier Data

Data for EuReCa are derived from examinations of the 10 solar panel segments, as described and tabulated in McDonnell et al. (1998a,b). We did not consider the MLI blankets and/or the satellite name plate in this work.

The general analysis strategy adopted for the EuReCa solar array was similar to that used in the HST-SA analysis. However, the thicker, rigid structure of the EuReCa solar panels obviated penetrations of the complex, stratified structure. Therefore, analysis was limited to the semi-infinite target region of admissibility as described in Section 2.2.3.3. Section 4 shows comparisons to ORDEM2000 results.

2.2.3.5 Aerogel Impact Experiments Aboard the Mir *Space Station*

Due to the immaturity of analyses concerning cratering phenomena in the Aerogel panels deployed by the MEEP experiment, and concerns about the apparent violation of several experimental controls, e.g. MEEP orientation with respect to the *Mir* velocity vector, we did not perform an in-depth analysis. Rather, we include Panel 1 and 2 data (Hörz et al. 1999) in

following sections dealing with comparisons between ORDEM2000 and the observed environment for a general, or qualitative, comparison only.

2.2.4 Solar-Related Effects Modeling

2.2.4.1 Projected Solar Activity for Atmospheric Drag

Solar activity directly influences the orbital debris environment by heating the Earth's upper atmosphere, principally at the extreme ultraviolet wavelengths. Because these wavelengths are not observable at ground level, the solar flux at 10.7-cm wavelength is used as an analogue. Atmosphere models then use these flux values to estimate the exospheric temperature, which controls upper atmospheric density and, hence, satellite drag.

This work consisted of two portions. The first activity was to assemble a FORTRAN subroutine that would contain relevant solar activity models. We tested the subroutine in the EVOLVE 4.0 code to examine the sensitivity of the environment to different solar models. The second activity dealt with examining the historical solar activity to assess the relative accuracy of various solar activity models.

We used two models in this study, in addition to historical (1957-2000) solar activity archived by the National Oceanic and Atmospheric Administration (NOAA). These are referred to as the NOAA model (in conjunction with the Australian Ionospheric Prediction Service) and the NASA Marshall Solar Activity Future Estimation (MSAFE) model.

Figure 2-19 gives results from the first task. In this figure, models are used out to the end of their prediction cycle, and then repeated in a cyclic fashion. The second task compared the NOAA model with the MSAFE model. Data used in this analysis were taken from the NOAA Space Environment Center website and a paper describing the MSAFE model (Vaughan et al. 1999), respectively. In addition, since we are concerned with the veracity of a given model's predictive capabilities (given that all predictions are phenomenological in nature), historical NOAA predictions were taken from copies of Solar-Geophysical Data.

The chosen analytical technique was to compare predictions made at solar maxima and minima with NOAA and MSAFE predictions. We recorded differences between the predicted solar activity and the observed solar activity, and also tabulated a frequency distribution in these differences. We employed both χ^2 and Kolmogorov-Smirnov (Sachs 1984) goodness-of-fit testing on both the differences and the frequency distribution in difference. Goodness-of-fit testing indicates that the NOAA predictions performed slightly better than did the MSAFE predictions for solar cycles 20, 21, and 22. Thus, a solar activity model predicated on the NOAA/Ionospheric Prediction Service forecast appears to offer a better estimate of the future solar activity at this time.

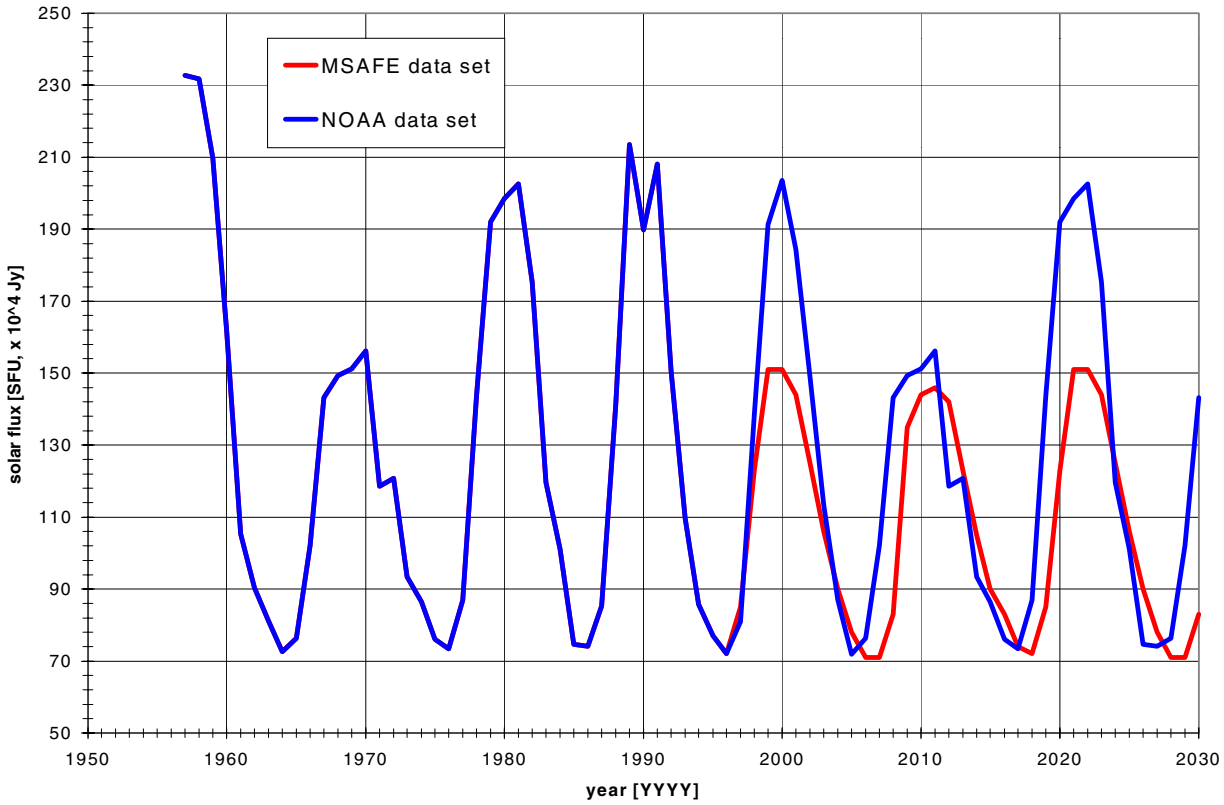

Figure 2-19: A comparison of historical and projected solar activities.

2.2.4.2 Solar Radiation Pressure

For particles smaller than about 1 mm in diameter, the effects of solar radiation pressure can become important. Solar radiation pressure typically causes the eccentricity of an orbiting object to oscillate. This usually shortens the lifetime of small debris by lowering their perigee into the atmosphere faster than would be expected from atmospheric decay alone. For debris sizes for which solar radiation pressure is important, the overall effect is to alter the altitude distributions. Circular orbit populations with lifetimes controlled by atmospheric decay typically have spatial densities (at lower altitudes especially) that vary inversely proportionally to the local density of the atmosphere. Solar radiation pressure can cause this distribution to be different.

In order to include the effect of solar radiation pressure, we use a simple propagation model to simulate the creation of small particles in the 10-µm to 1-mm size range. For the model, we assumed that these small particles were created from intact objects due to some regular process like micrometeoroid impacts or material degradation. The model is used to simulate the relative size-dependent orbit distributions of the particles. For sources, we use the historical catalog using only intact objects and weight each source object by its approximate surface area. A series of orbit "snapshots" is created for each intact object that defines its orbital parameters at regular intervals of time. At each time step, a particle with random size is "created," having the same orbit as its parent at each initial time. Each particle is then propagated independently under the influence of

solar radiation pressure and atmospheric drag to specific reference times. We used the total population of small particles at each of these reference times to define the size-dependent orbit distributions at those times. We used the in situ data—specifically from LDEF— to calibrate the relative numbers in each population based on eccentricity, inclination, and size.

Once the population production rates are scaled to the LDEF data (representing conditions in the mid-1980s), it is a simple matter to project those populations into the future using the same model. For launch traffic after 1999, we used a catalog for 1999 and scaled the area weighting for each object using the total number of future intact objects derived from EVOLVE. In other words, the orbit distributions are frozen for 1999, but the production rate varies as the projected future population of intact objects varied. However, as was described above, the production rate in the 1990s appears to be different than that in the 1980s as measured by LDEF. This empirical effect has been added to fit the data sets. Because of the differing behaviors of elliptical and circular orbits under the influence of solar radiation pressure, we created separate high- and low-eccentricity time histories for the 10-µm and 100-µm populations.

We project into regions with no, or little, impact data by using the scaled populations to extrapolate to those regions. While we do not directly know the small particle populations at higher altitudes, the populations we do know reflect the distribution of debris at higher altitudes whose orbits have decayed into the measured region. In other words, the orbit populations at lower altitudes indirectly reflect the orbit populations at higher altitudes that have decayed down. If we have modeled the decay process correctly using atmospheric drag and solar radiation pressure, then we should be able to reconstruct the populations at higher altitudes. One other factor that helps in this reconstruction is that for particles less than 1 mm in size, the time scale of decay is rather short—no more than a few years in the most important cases. Therefore, it does not take long for changes at high altitudes to start affecting populations at low altitudes. This increases our confidence that the LDEF measurements are accurately reflecting conditions at higher altitudes as well—at least for the relative orbital parameter distributions for altitudes less than about 1000 km.

2.2.5 EVOLVE Auxiliary Modeling

An engineering model, such as ORDEM2000, is not an ideal tool to predict the future debris environment. The major factors controlling the future debris environment include the launch traffic, types of vehicles, deorbit control, solar activity, and the dynamical evolution of debris particles under the influence of various perturbations and atmospheric drag. It is very difficult to implement all the effects explicitly in an engineering model. However, since a spacecraft program can span several decades from planning to end-of-life, it is useful to have a projection function included in an engineering model. A simple future projection function (1991 to 2030) is implemented in ORDEM2000. For debris 1 cm and greater, the function is based on the spatial density variation, at each altitude bin, between 1991 and 2030, from the NASA orbital debris evolution model EVOLVE 4.0 (Krisko et al. 2000).

The first step in EVOLVE is to model historical launches and breakup events, including explosions and collisions. Breakup fragments are then propagated forward in time numerically

with other intact objects. The gravitational force of Earth and its J_2 perturbation, solar-lunar perturbations, and atmospheric drag are all included in the propagator. The intact object and debris populations since 1957 are calculated until the end of 1999. The spatial density or number of objects of a given size and greater, at a given altitude and at a given time, from EVOLVE can then be compared with radar, optical, or in situ debris measurements. Once the current debris environment is modeled properly, EVOLVE takes an assumed launch traffic and an assumed solar activity projection and uses a Monte Carlo approach to model future on-orbit explosions and collisions and predict the future LEO debris environment.

To obtain the spatial density variation of debris particles greater than 1 cm, a special EVOLVE simulation has been performed. The historical part of the simulation was based on all known breakup events up to the end of 1999. We used a business-as-usual future launch traffic that repeated the 1992 through 1999 traffic (Section 2.2.6) and the NOAA solar activity projection (Section 2.2.4) in the future projection mode in EVOLVE. The spatial densities of objects greater than 1 cm, 10 cm, and 1 m at each 50-km bin between 200- and 2000-km altitude were recorded from the output.

The spatial densities at four selected altitude bins between 1991 and 2030 are shown in Figures 2-20 to 2-25. The future projections in Figures 2-23, 2-24, and 2-25 are from EVOLVE. Those in Figures 2-20 and 2-21 are produced by the method described in Section 2.2.4.2. The 1-mm population in Figure 2-22 represents the interpolation between the 100-µm and 1-cm populations as described in Sections 2.2.3.1 and 2.2.3.2.

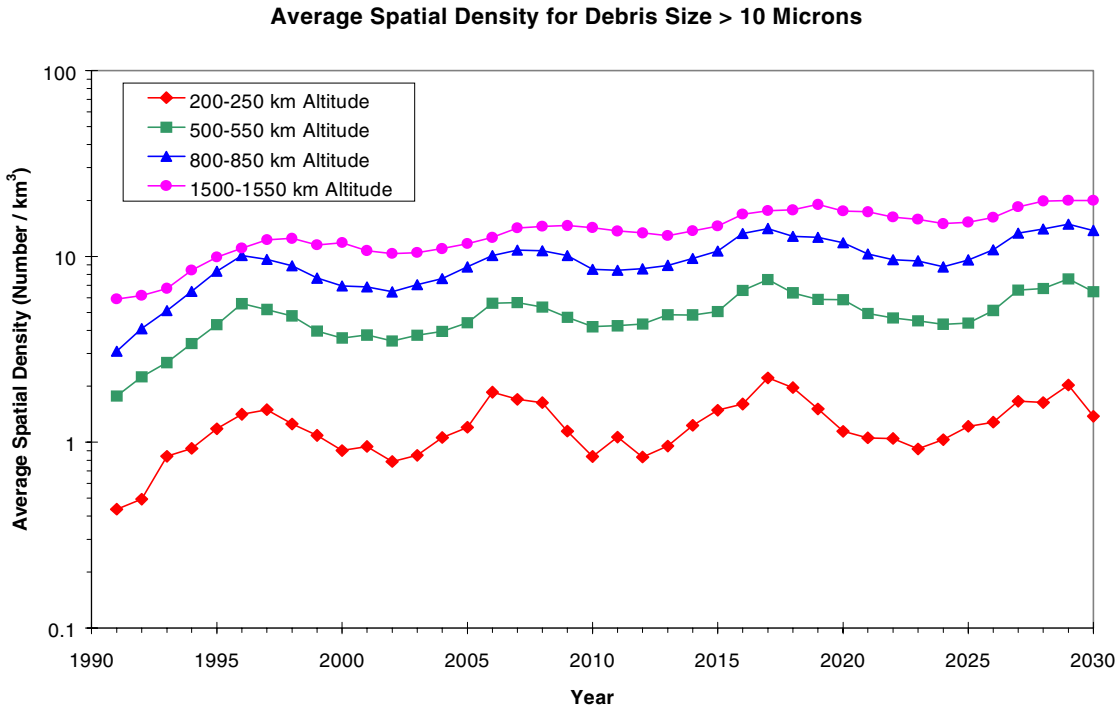

Figure 2-20: Spatial density variation between 1991 and 2030 for debris >10 µm in size. The densities are benchmarked from in situ data in the 1980s and 1990s, and the future projections are estimated from the small-particle production model described in the text.

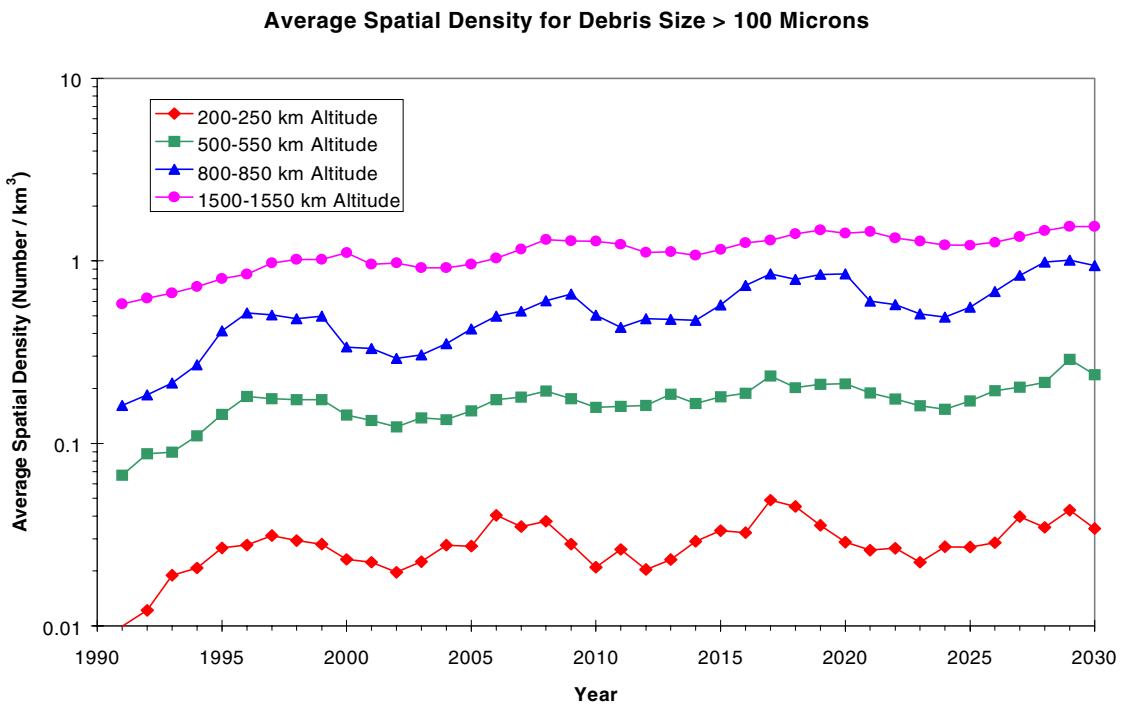

Figure 2-21: Spatial density variation between 1991 and 2030 for debris >100 µm in size. The densities are benchmarked from in situ data in the 1980s and 1990s, and the future projections are estimated from the small-particle production model described in the text.

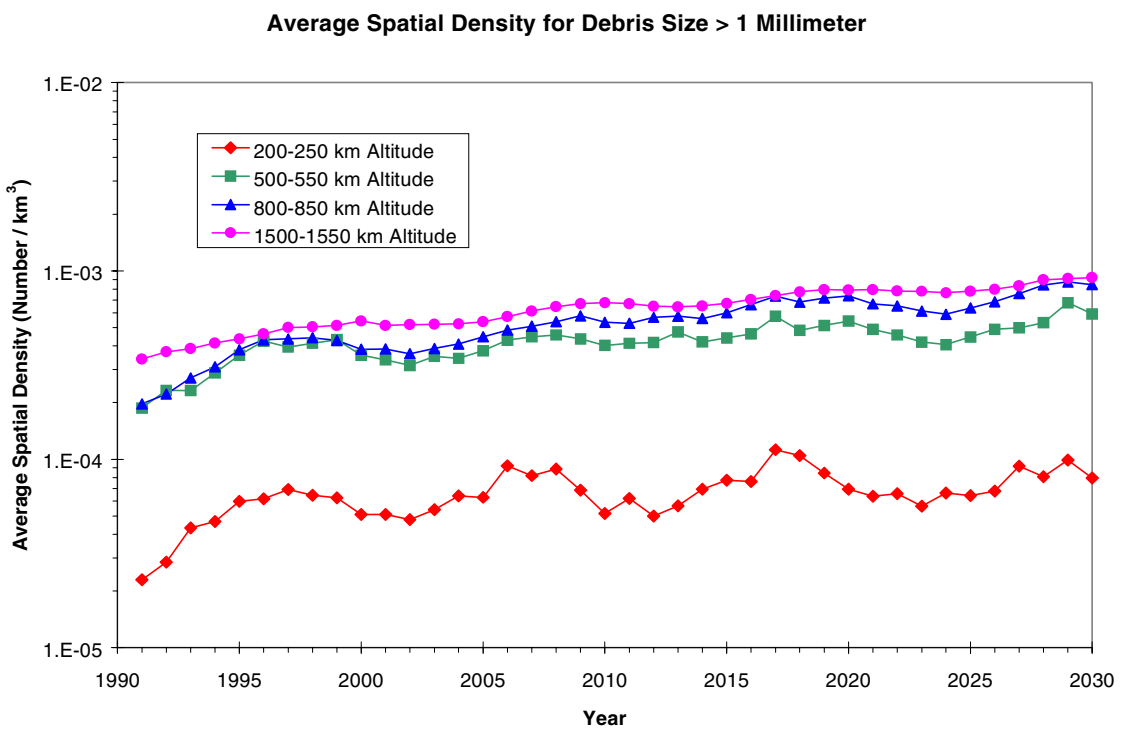

Figure 2-22: Spatial density variation between 1991 and 2030 for debris >1 mm in size. The densities are interpolated between the values obtained for 100-µm sizes (Figure 2-21) and 1 cm sizes (Figure 2-23), with the more elliptical orbit populations adjusted to match data from the 1990s.

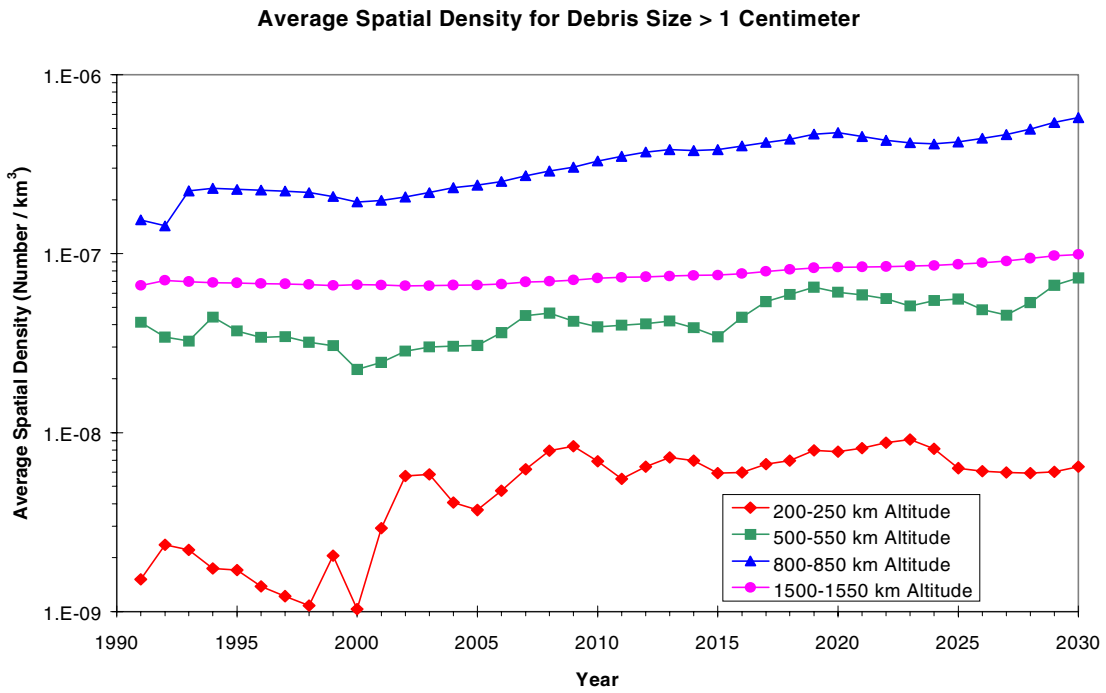

Figure 2-23: Spatial density variation between 1991 and 2030 for debris >1 cm in size. The densities are benchmarked from Haystack data in the 1990s and the future projections are estimated from EVOLVE.

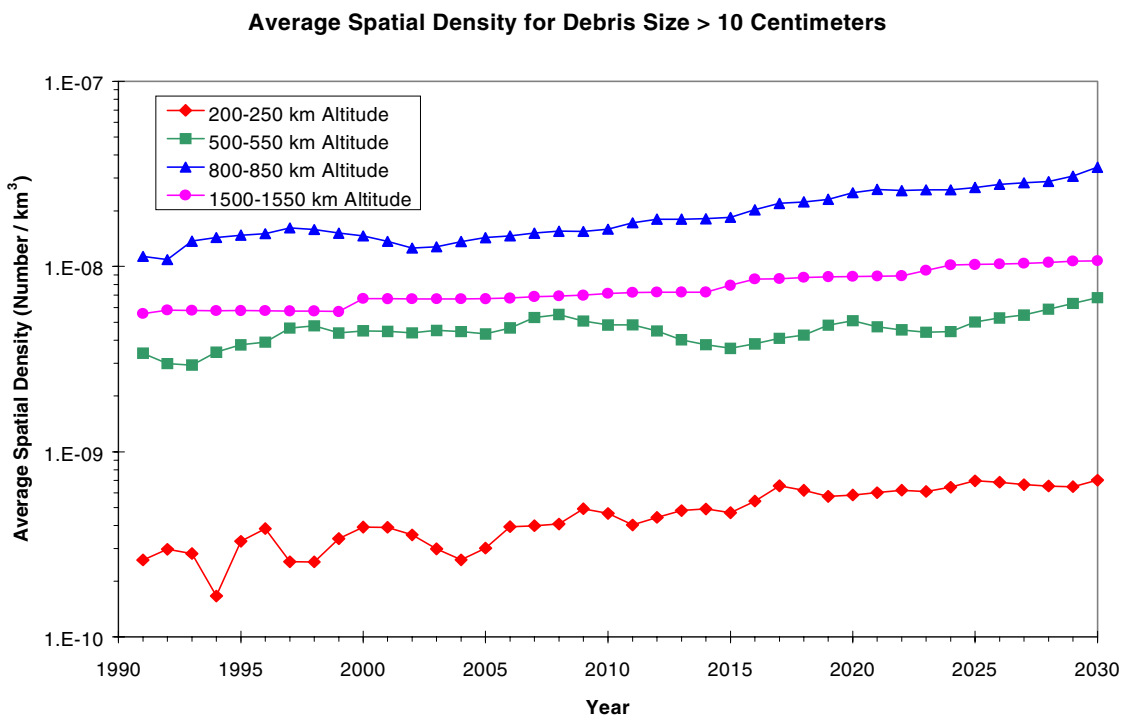

Figure 2-24: Spatial density variation between 1991 and 2030 for debris >10 cm in size. The densities are benchmarked from U.S. Space Command data and the future projections are estimated from EVOLVE.

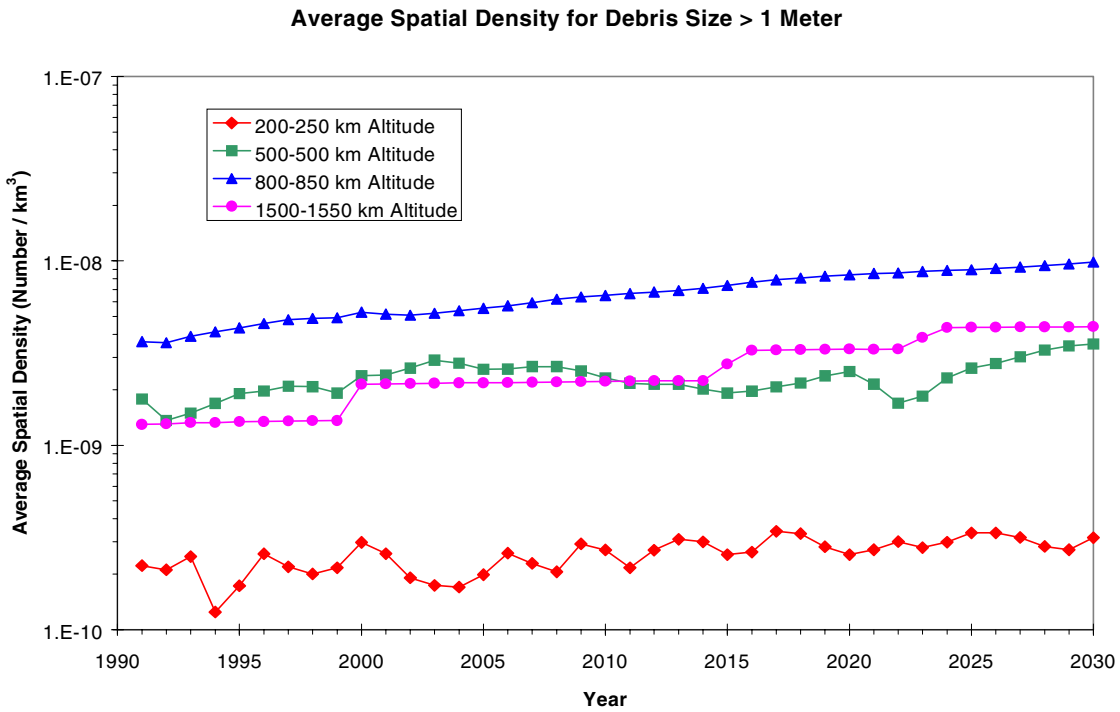

Figure 2-25: Spatial density variation between 1991 and 2030 for debris >1 m in size. The densities are benchmarked from U.S. Space Command data and the future projections are estimated from EVOLVE.

2.2.6 Future Launch Traffic Model

Many investigators have attempted to divine future space launch traffic with only limited success. Among the reasons for overall failure are the development of new technologies and/or launch vehicles, nonviable military or commercial developments, and changes in the socio-economic or military structure of the originating nation or international entity. Industry projections may in some cases be proprietary and in any case seldom extend beyond four years past the current date. Thus, the investment of a significant effort in prognosticating the future launch traffic was not regarded as a worthwhile portion of the overall ORDEM2000 upgrade effort.

Rather, the approach utilized by the NASA EVOLVE long-term debris evolution model was adopted. This approach models future space launch traffic by cycling through the last eight years of historical space launch traffic. In ORDEM2000, we used traffic spanning the years 1992-1999 to project the current environment out to the year 2030. Figure 2-26 shows hstorical and projected traffic.

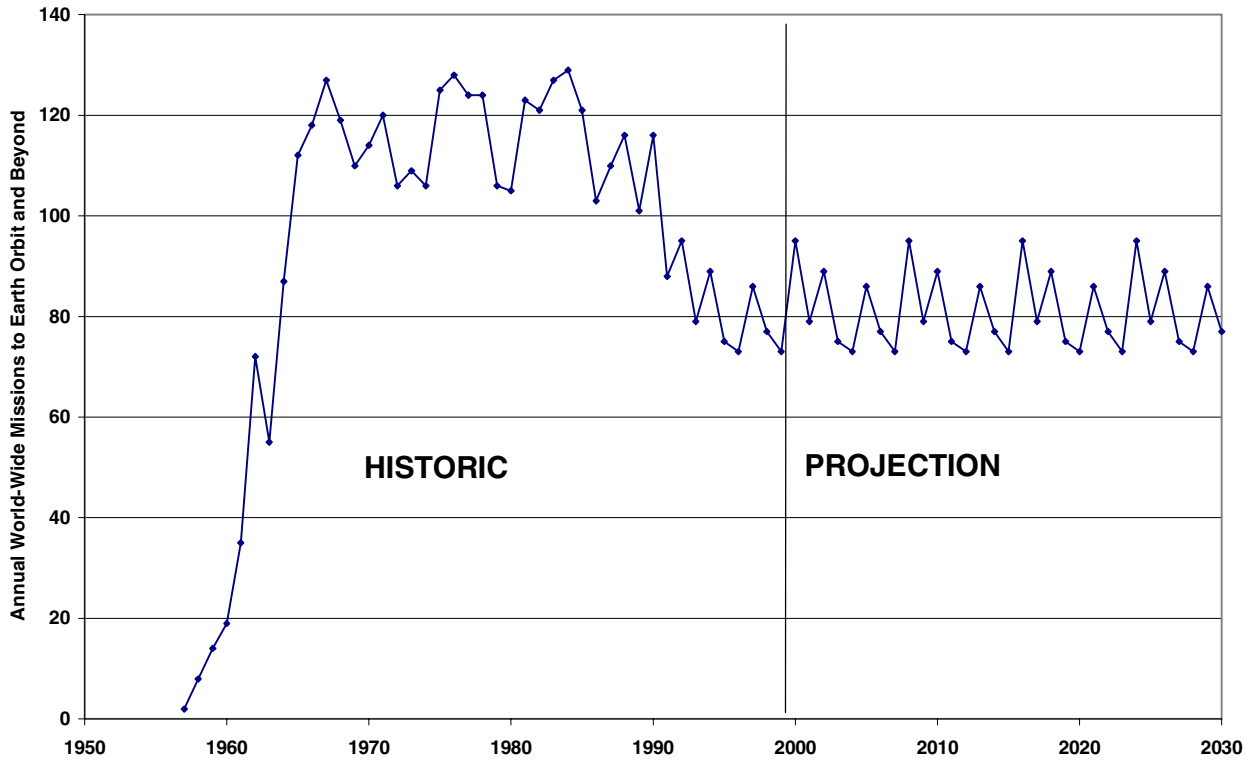

Figure 2-26: Historical and projected launch traffic.

The reader should note that launch rate is not indicative of debris production either historically or over the period of the projection. This is because debris production is not uniform over the population, i.e. all events do not produce identical numbers of debris and all members of the population are not subject to the same probability of fragmentation. The historical number of fragmentation events not traceable to the design or the practices and procedures used by a particular vehicle class is relatively small.

2.2.7 Extension of Data Sets up to 2000 km Altitude

The data sets available to use do not have complete coverage. Radar and telescope data do not adequately measure low-inclination orbits. Returned surfaces only sample at the altitude of the spacecraft. Each type of experiment only measures a certain size regime at a particular time. None tell us what the future is going to be like.

For extrapolations into the past and into the future, the time projections outlined above are used to estimate how the populations evolve. This allows populations estimated from data taken in the past to be “projected” to the reference date.

There are several key regimes for which we are missing data. The first is the 10- and 100-µm population above about 600-km altitude. The method used to estimate these populations at higher altitudes is described in Section 2.2.4.2.

The next region for which data are missing is the 1-cm population with inclinations below about 25 deg. There is another similar gap for altitudes above about 1200 km with inclinations less than about 43 deg. These represent a true gap in our knowledge of the LEO environment due to limitations in the radar coverage. We estimate the 1-cm populations in these regions by using orbit distributions in similar regions where we had data and scaling the numbers to the intact population. For example, one can estimate the elliptical orbit population at 7-deg inclination by scaling the ratio of the 1-cm to 10-cm populations for 28-deg inclination elliptical orbits and multiplying the scaling factor times the catalog population in 7-deg elliptical orbits.

We also have a lack of detailed information about the 1-mm population. The 1-mm populations were found by interpolating the log spatial densities between the 100-µm population and the 1-cm population. We assume the time-dependence factors and velocity distributions to be the linear average between these two populations. The justification for this was that we expect some fraction of the 1-mm population to be due to breakup fragments, and the rest due to surface degradation. So we made an "even mix" of 100-µm particle (believed to be primarily surface degradation) and 1-cm particles (believed to be primarily breakup debris). These simple averages are adjusted using the Goldstone data (see Section 2.2.3.2).

3. ORDEM2000 Debris Environment Model

Once a debris population is characterized in terms of size and orbital parameters, one can build a LEO debris environment model from the population to describe the debris spatial density and velocity distribution in space. This step is one of the major differences between ORDEM2000 and the previous model ORDEM96. Figure 3-1 outlines the different approaches of the two models. Once a debris population is derived from existing data, ORDEM96 simplifies the population into 6 inclination bands and 2 eccentricity families. The six inclinations chosen are 7 deg, 28 deg, 51 deg, 65 deg, 82 deg, and 98 deg. Objects within each inclination band are assumed to have the same inclination rather than a distribution of inclinations. Objects with eccentricities less than 0.2 are considered to be on circular orbits (e = 0) while the rest are considered to be on elliptical orbits with eccentricities between 0.5 and 0.6. In addition, ORDEM96 assumes that the longitudes of the ascending node (Ω) and arguments of perigee (ω) of objects are randomly distributed in space. With additional approximations to the size distribution and orbital perigee distribution, a set of equations can be derived to represent the LEO debris environment (Kessler 1981, Kessler et al. 1996). One can then take the equations and calculate the impact flux on an orbiting spacecraft or the debris flux expected to be observed by a ground-based telescope or radar.

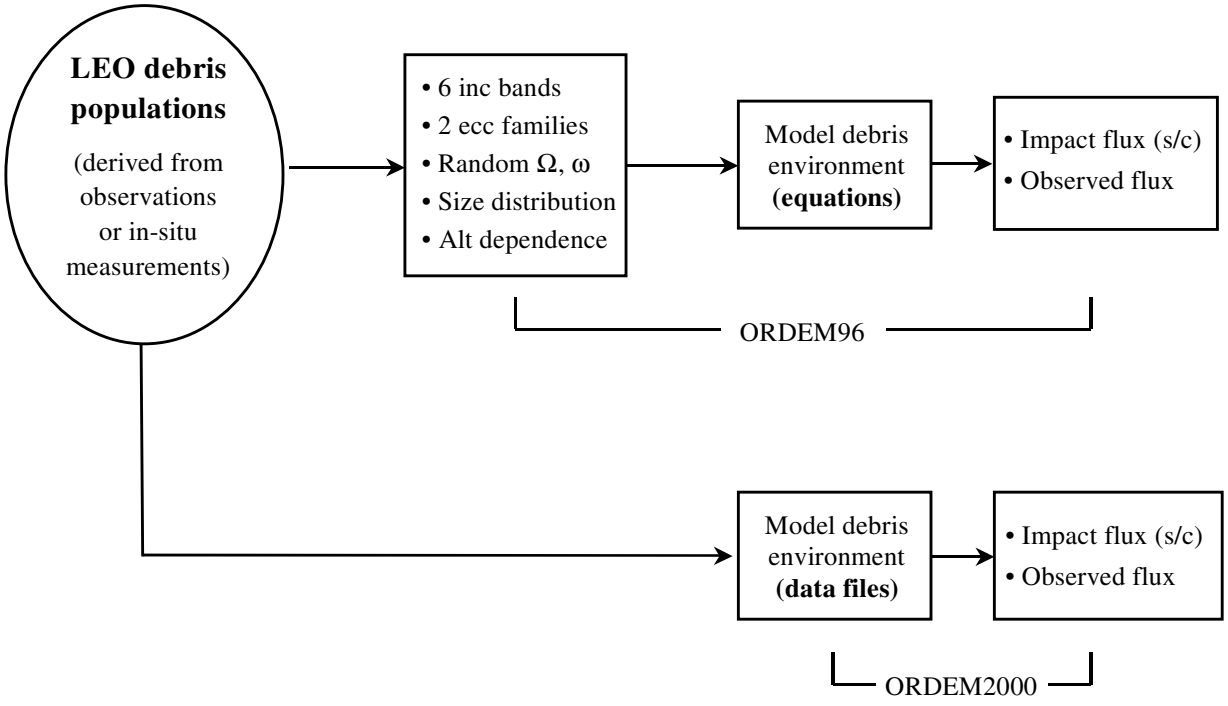

Figure 3-1: ORDEM96 and ORDEM2000 use different approaches to build the LEO debris environment model.

To fully utilize the debris populations derived from the data sources, ORDEM2000 adopts a different approach when building the debris environment model. The approach essentially transfers the computer burden of determining debris spatial density and velocity distribution from being *part of the model* to computer processing that is performed as a part of *building the model*. The advantage of this approach is that as the fidelity of the orbital debris data increases (i.e., we more accurately determine the size and orbit distributions of debris), no approximations are required to include all of this data in the environment model.

The ORDEM2000 debris environment model is a finite element model (Section 3.1). It describes the spatial density, velocity distribution, and inclination distribution of debris particles at different latitudes and altitudes. The debris environment is represented by a set of pre-processed data files. No assumptions regarding debris particles' inclinations, eccentricities, or orientations in space (longitudes of the ascending node and arguments of perigee) are required in this approach. However, a decision was made to randomize the objects' ascending node longitudes. For most objects in LEO, the ascending nodes are randomized, but many intact objects in Sun-synchronous orbits have preferred ascending nodes. Most debris in Sun-synchronous orbits, however, are in orbits with randomized ascending nodes. Also, if an object with a randomized ascending node encounters an object with a preferred ascending node, the collision calculations are equivalent to the case where both objects are random. Consequently, the assumption of randomized ascending nodes will generally be adequate.

3.1 A Finite Element Model for LEO Debris Environment

The region between 200- and 2000-km altitude is divided into (5 deg × 5 deg × 50 km) cells in longitude (θ), latitude (90 deg-φ), and altitude (r), respectively (Figure 3-2). When a debris population is derived from observations, the resident time of each debris particle within each cell is calculated using the fractional time that it spends in that cell. For example, if a debris particle spends 3% of its orbital period within a given cell, 0.03 "object" is assigned to that cell. Once the same procedure is completed for every debris particle in the population, the spatial density of this debris population within each cell is simply the sum of objects within that cell divided by its volume V_{cell}, where

$$V_{cell} = \iiint r^2 (\sin\varphi)\, dr\, d\varphi\, d\theta,$$

and r, φ, and θ are defined in Figure 3-2.

The velocity of a debris particle within a given cell is calculated in two steps. The first step is to convert its orbital elements to the velocity and position vectors in the geocentric equatorial system. The conversion is straightforward (e.g., Bate et al. 1971). The second step is to transfer the velocity components to a special local system via two coordinate transformations. The local system is a right-handed geocentric system where the x-axis points in the radial-outward direction, the y-axis points in the local east direction, and the z-axis points in the local north direction. The plane defined by the y-axis and z-axis is the local horizontal.

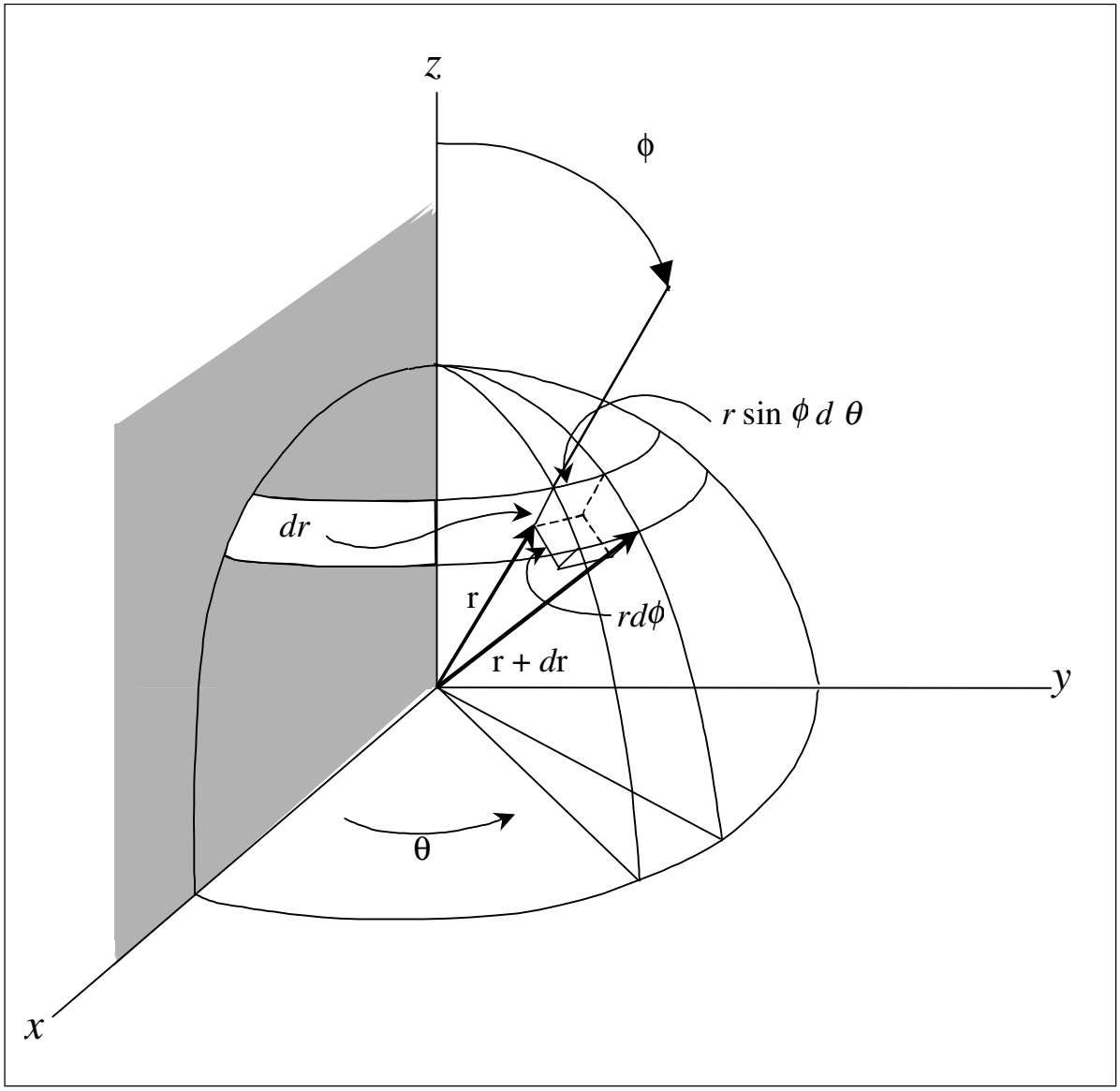

Figure 3-2: A finite element model.

Let (v_x, v_y, v_z) be the geocentric equatorial velocity components of a debris particle in a given cell. The components (v_{x2}, v_{y2}, v_{z2}) in the local system are calculated with the following two transformations:

$$v_{x1} = v_x \cos\theta + v_y \sin\theta$$

$$v_{y1} = -v_x \sin\theta + v_y \cos\theta$$

$$v_{z1} = v_z$$

and

$$v_{x2} = v_{x1} \cos(90-\phi) + v_{z1} \sin(90-\phi)$$

$$v_{y2} = v_{y1}$$

$$v_{z2} = -v_{x1} \sin(90-\phi) + v_{z1} \cos(90-\phi),$$

where θ and ϕ are defined in Figure 3-2.

The velocity distribution of debris particles within a given cell is calculated using all particles in the cell, weighted by their individual spatial densities. To reduce the size of the templates, only the velocity components in the local horizontal plane are recorded. This is justified since the radial velocity component is generally less than 0.1 km/sec while the horizontal velocity component is about 6 to 11 km/sec. The velocity distribution within each cell is stored in a magnitude-and-direction two-dimensional matrix, as shown in Figure 3-3. The magnitude ranges from 6 to 11 km/sec with an increment of 1 km/sec while the direction ranges from 0 deg to 360 deg with an increment of 10 deg. Each element in the matrix gives the fraction of particles with a velocity within the magnitude and direction specified by the position of the element. For example, the 2% element in Figure 3-3 indicates that 2% of all particles in this three-dimensional cell have their orbital velocity (in the local horizontal plane) between 6 and 7 km/sec with a direction between the local east and 10 deg northward. The sum of all elements in a matrix is always 100%.

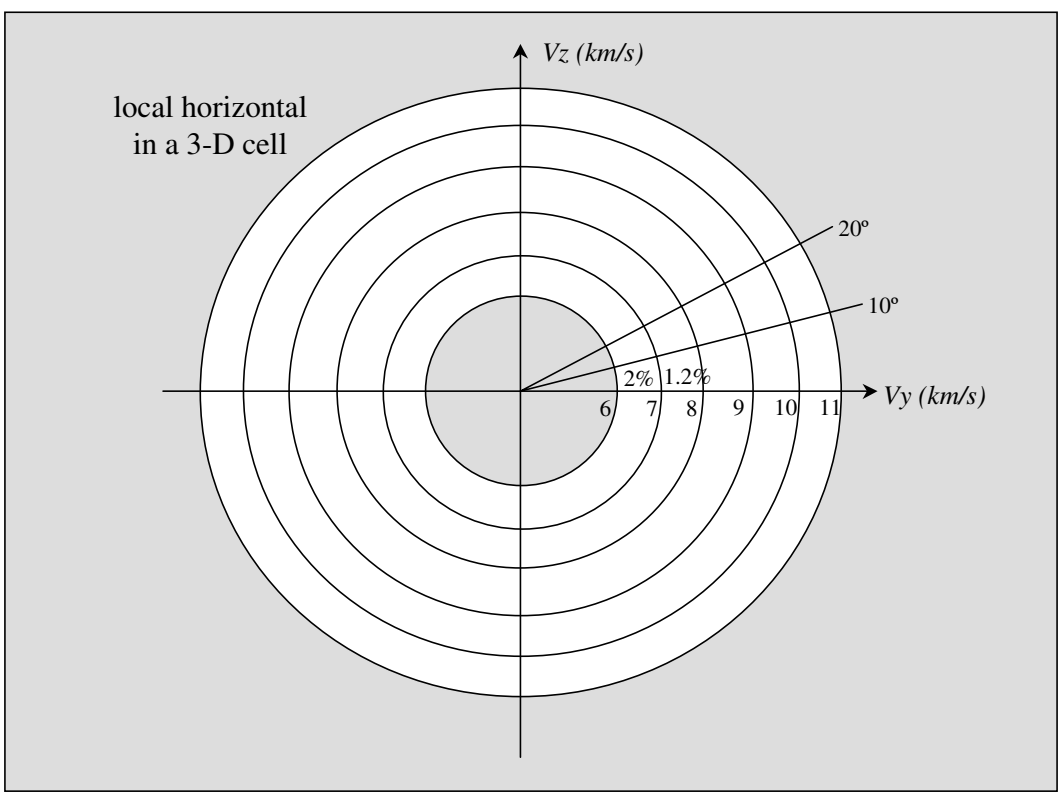

Figure 3-3: Velocity distribution matrix.

The inclination distribution of debris particles within each cell is also calculated and saved as part of the template files. The range is between 0 deg and 180 deg with an increment of 2 deg.

Figure 3-4 shows a spatial density map of the 100-µm population from the finite element model. It is the distribution of objects (number/km^3), between 800 and 850 km altitude, as viewed from the center of the Earth. The x-axis is the projected longitude (-180 deg to 180 deg) in the sky while the y-axis is the projected latitude (-90 deg to 90 deg).

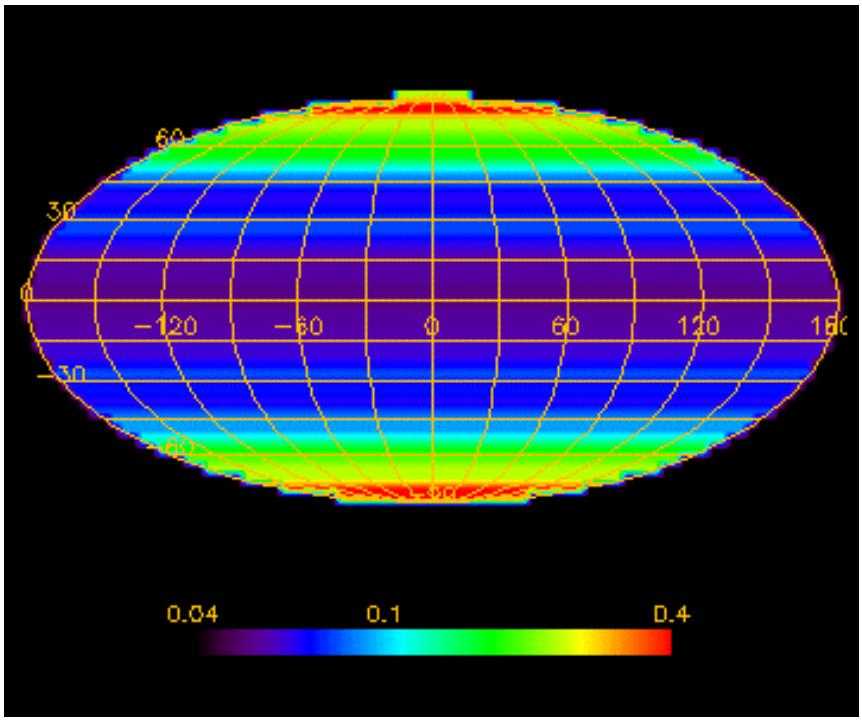

Figure 3-4: Color-coded spatial density distribution (no/km^3) of 100-µm objects, between 800 and 850 km altitude, as viewed from the center of the Earth.

3.2 Applications of the Debris Environment Model

The spatial density, velocity distribution, and inclination distribution files ("template files") form the basis of ORDEM2000. The model has two application modes: (1) a ground-based telescope/radar mode and (2) an orbiting spacecraft mode. The two options require different input parameters and produce different output files. Once the option and input parameters are defined, the model extracts information from the template files and performs the calculations as described below.

3.2.1 For a Ground-Based Observer

For an observer using a telescope or radar (such as Haystack) to observe orbital debris from the ground, two options are available: a vertical staring mode and an arbitrary pointing mode. The vertical staring mode requires two parameters: the geographic latitude of the instrument and the time of the observation (between years 1991 and 2030). The user can specify the names of the output files containing spatial density and average orbital velocity of objects of 6 fixed sizes (≥10 μm, ≥100 μm, ≥1 mm, ≥1 cm, ≥10 cm, ≥1 m). The user also has the option to obtain the surface area flux of any arbitrary size objects. The surface area flux is defined as the number of objects passing through the beam width, per unit area, per unit time. The inclination distribution and velocity distribution files at various altitudes are also available for additional analyses. The arbitrary pointing mode requires four parameters: the geographic latitude of the instrument, the time of the observation (between 1991 and 2030), and the pointing direction in terms of azimuth and elevation angles. The standard output is the surface area flux of particles of the six standard sizes.

3.2.2 For an Orbiting Spacecraft

To calculate the flux on an orbiting spacecraft, the user first has to specify the orbit of the spacecraft. The model "flies" the spacecraft through the environment and then selects template files along the orbit for the calculation. The orbit options include selecting the semimajor axis and eccentricity or the perigee and apogee altitudes of the orbit. Additional input parameters include the orbital inclination and argument of perigee of the orbit and the time of the mission (between 1991 and 2030). An additional parameter, N_{seg}, is also required. The model divides the orbit of the spacecraft into N_{seg} segments in equal mean longitude (i.e., equal time) and then calculates the flux, from particles of the six different sizes, on the spacecraft at each segment. The output results are stored in a flux table. It includes the altitude and latitude of the spacecraft at each segment and the fluxes from particles of six different sizes at that location. At the end of the table, fluxes averaged over N_{seg} segments are also given. A cubic spline interpolation (Press et al. 1992), in log(flux) vs. log(diameter) space, is applied to the output to get the flux from any arbitrary size debris between 10 μm and 1 m. As with any finite element model, one does not have smooth transitions between cells. This may create unnecessary misunderstanding for spacecraft designers with various altitude options. To ensure smooth transition in altitude, a linear interpolation function in log(spatial density) has been implemented using the spatial density files of two adjacent cells in altitude. Since a spacecraft is assumed to have a spherical shape in ORDEM2000, the flux given in the spacecraft mode is the cross-sectional flux.

The model also includes an additional subroutine to compute the "butterfly" distribution of the flux on a spacecraft. The output file contains the fluxes broken down by direction and velocity relative to the target spacecraft.

4. ORDEM2000 Verification and Validation

4.1 Comparisons With Radar Observations

In this section, we compare ORDEM2000 predictions with the Haystack and HAX radar data. The radar data are taken from Settecerri et al. (1999) and Stansbery et al. (2000). Haystack data are believed to be complete for debris particles greater than about 1 cm in diameter while HAX data are complete for debris particles greater than about 5 cm in diameter. Figures 4-1 to 4-4 show the comparisons in 1999 for debris greater than 1 m, 10 cm, 5 cm, and 1 cm, respectively. Each error bar in the observed flux represents the 1 σ standard deviation. Each "error bar" in altitude simply indicates the altitude range where the flux was calculated. Figures 4-5 to 4-8 show comparisons with the 1998 radar data. Figures 4-9 to 4-12 show comparisons with the 1997 radar data. Overall, ORDEM2000 predictions compare well with the Haystack and HAX radar observations.

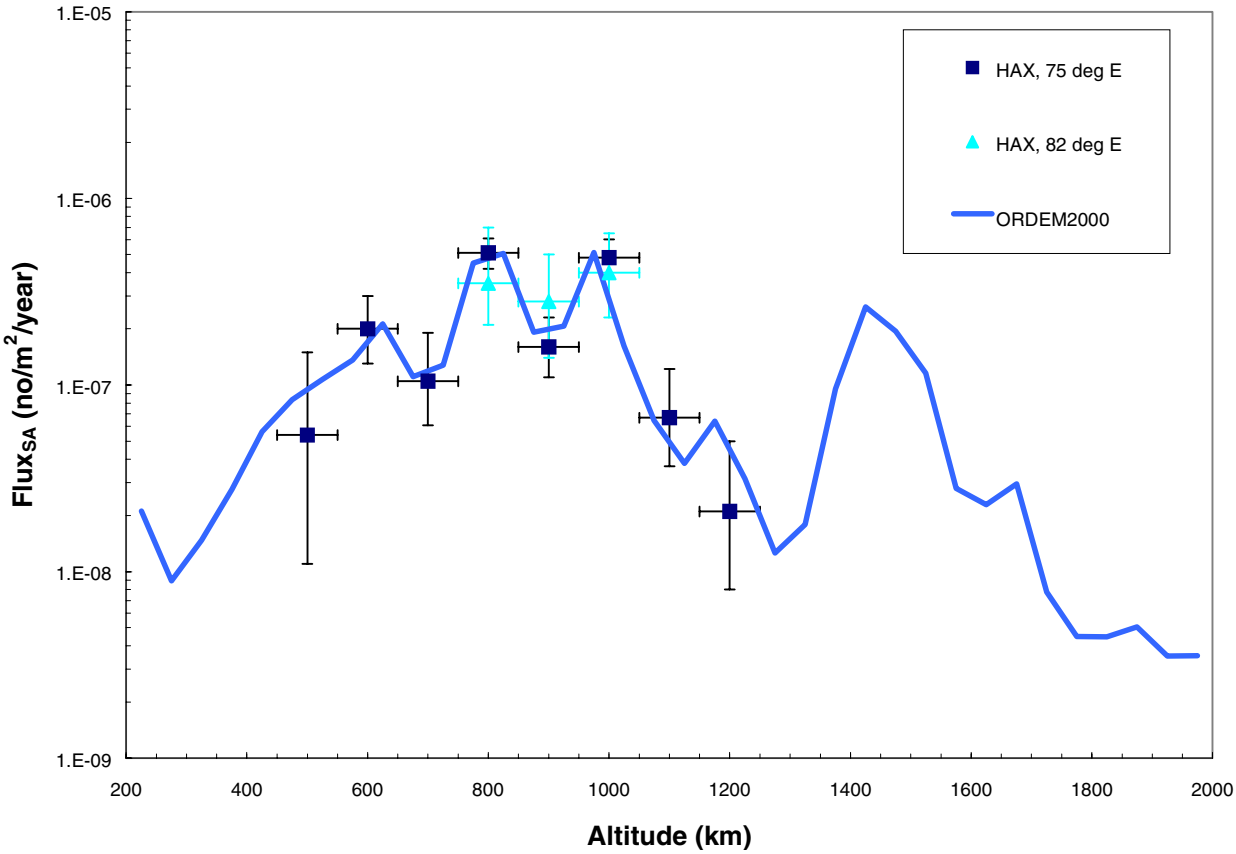

Figure 4-1: ORDEM2000 vs. HAX data (1999, objects ≥1 m).

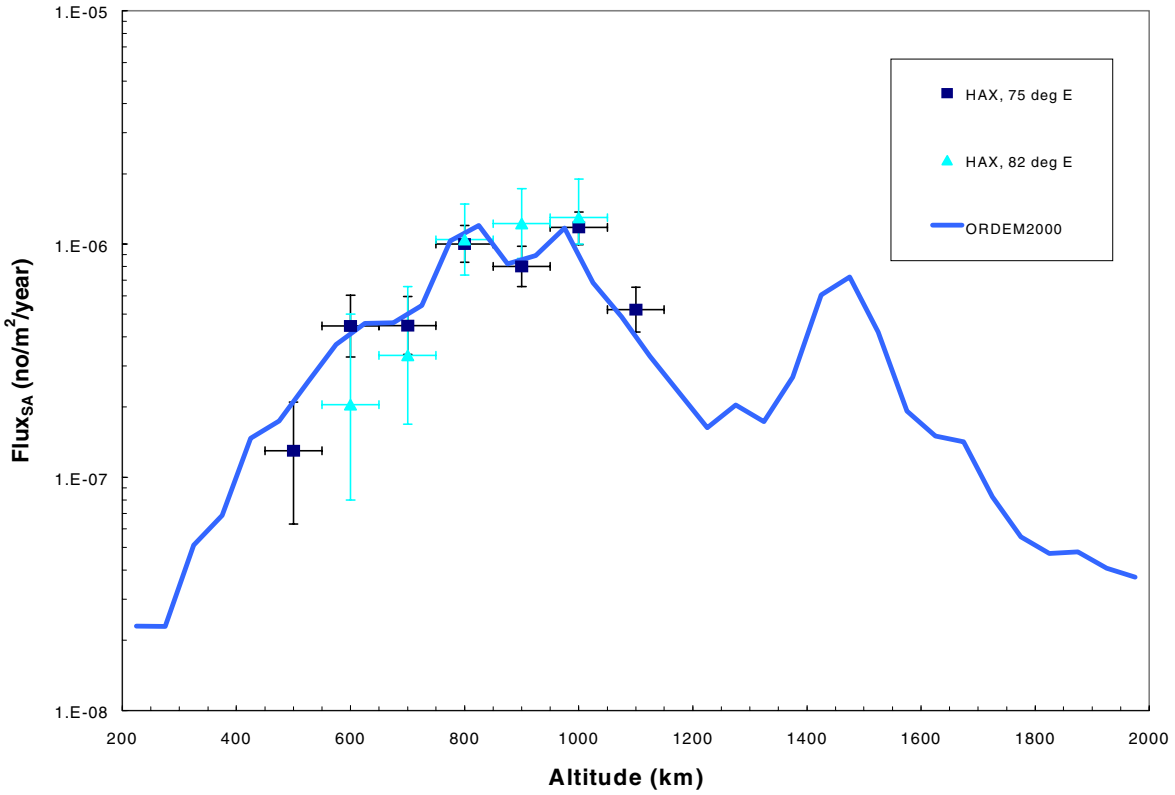

Figure 4-2: ORDEM2000 vs. HAX data (1999, objects ≥10 cm).

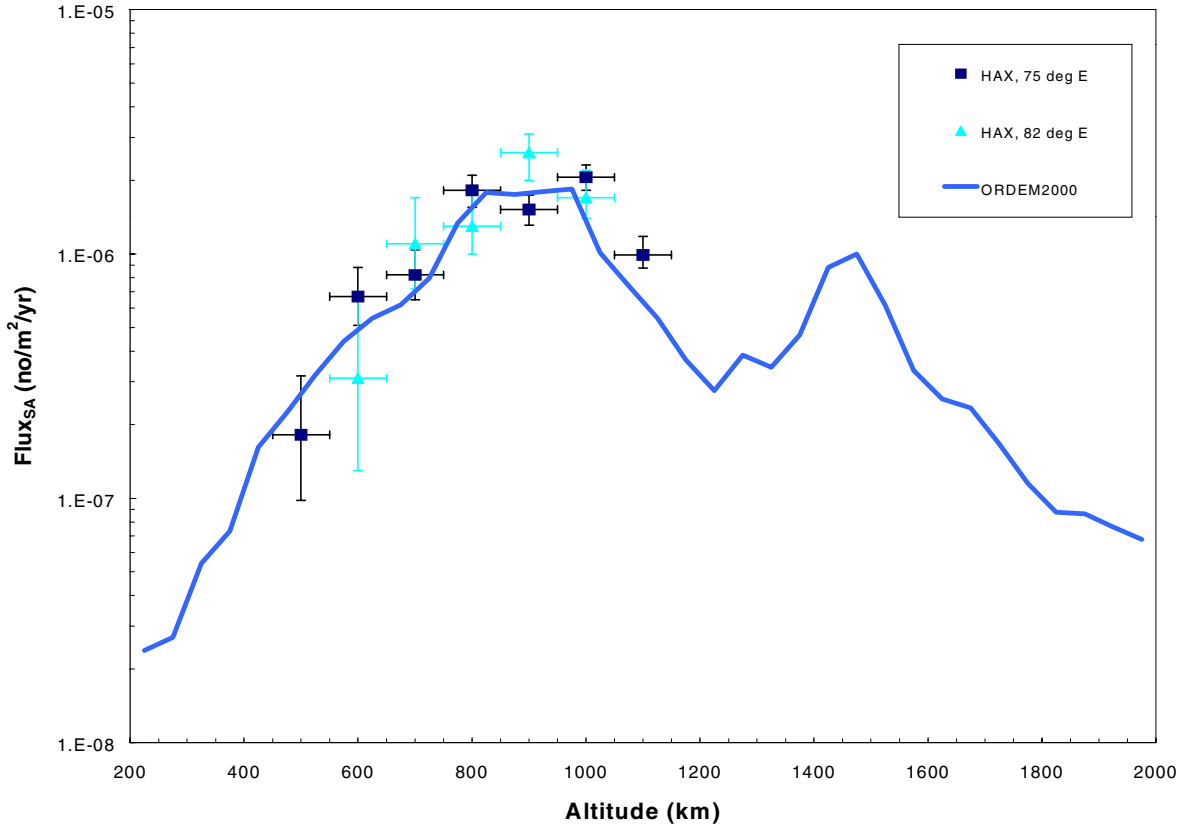

Figure 4-3: ORDEM2000 vs. HAX data (1999, objects ≥5 cm).

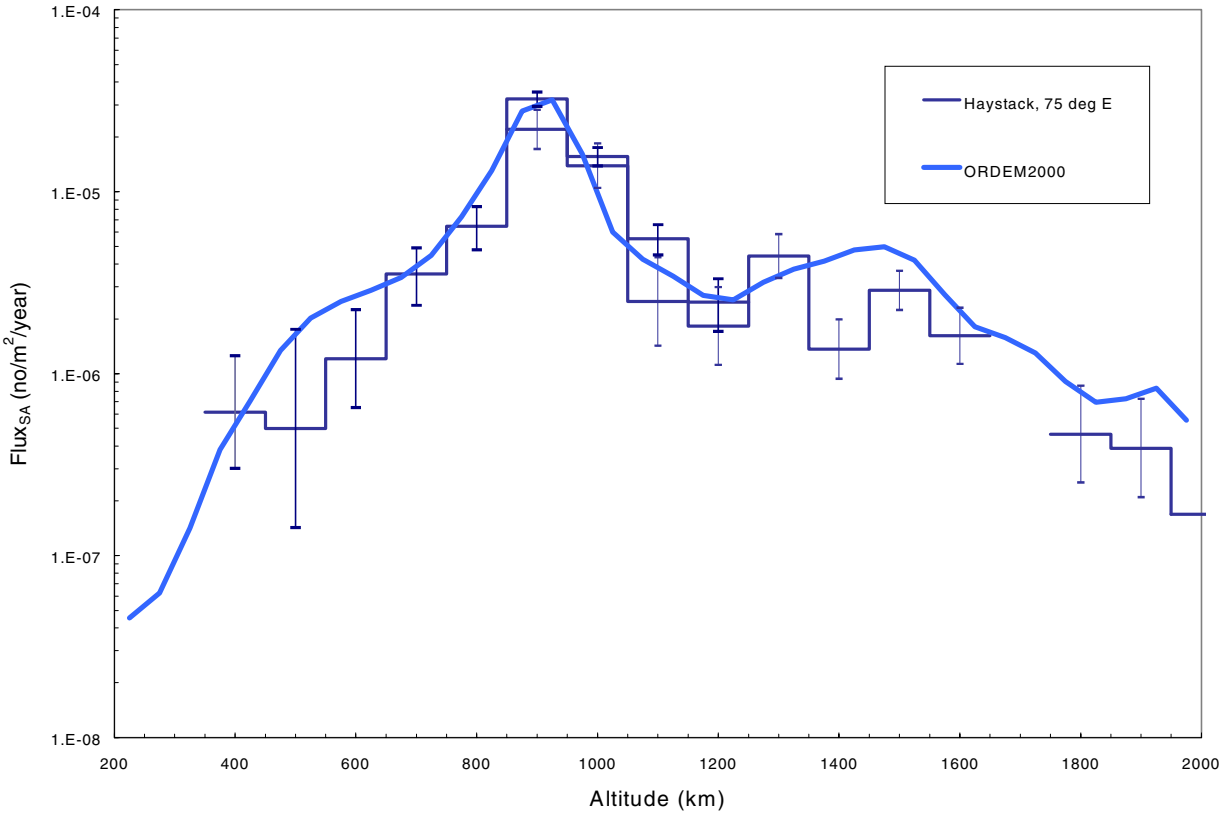

Figure 4-4: ORDEM2000 vs. Haystack data (1999, objects ≥1 cm).

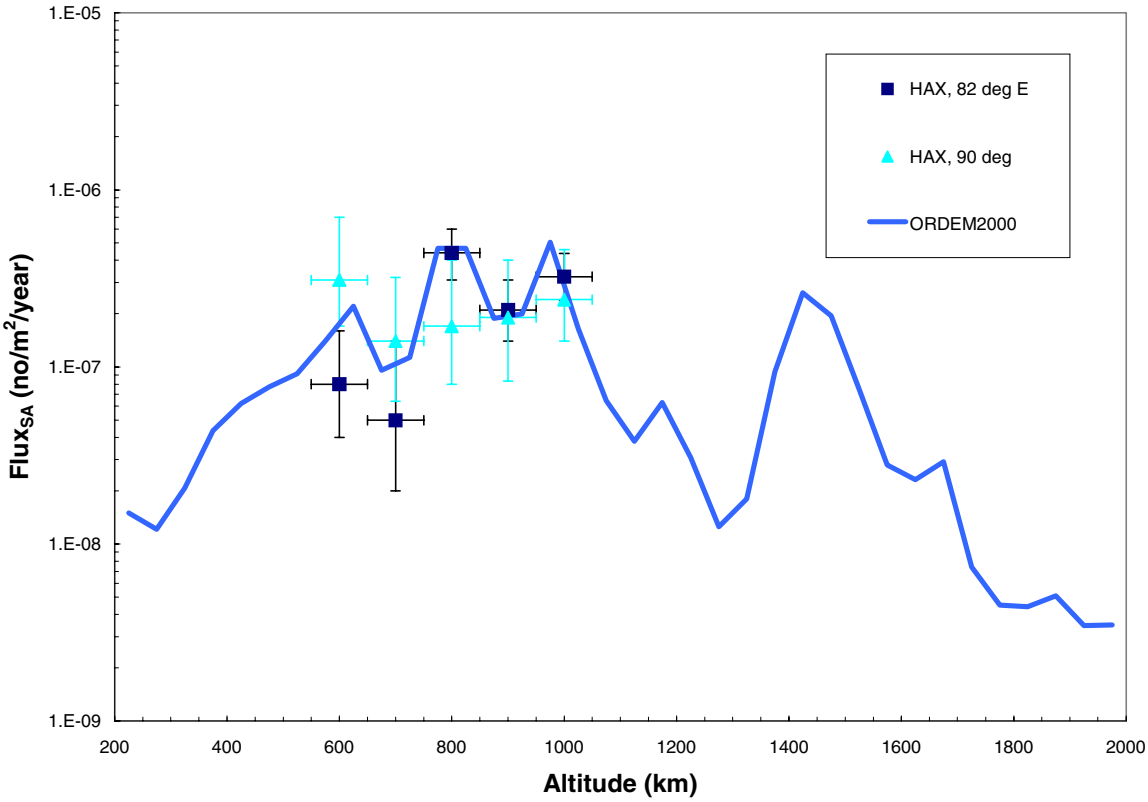

Figure 4-5: ORDEM2000 vs. HAX data (1998, objects ≥1 m).

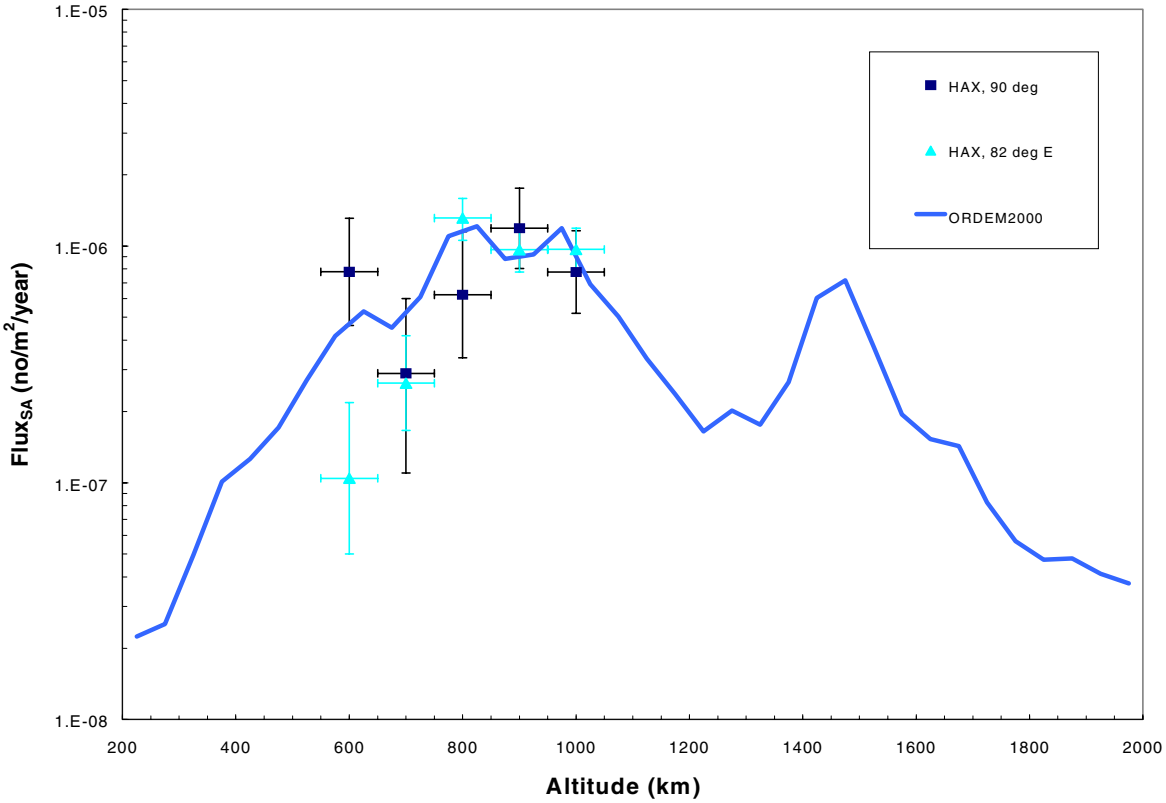

Figure 4-6: ORDEM2000 vs. HAX data (1998, objects ≥10 cm).

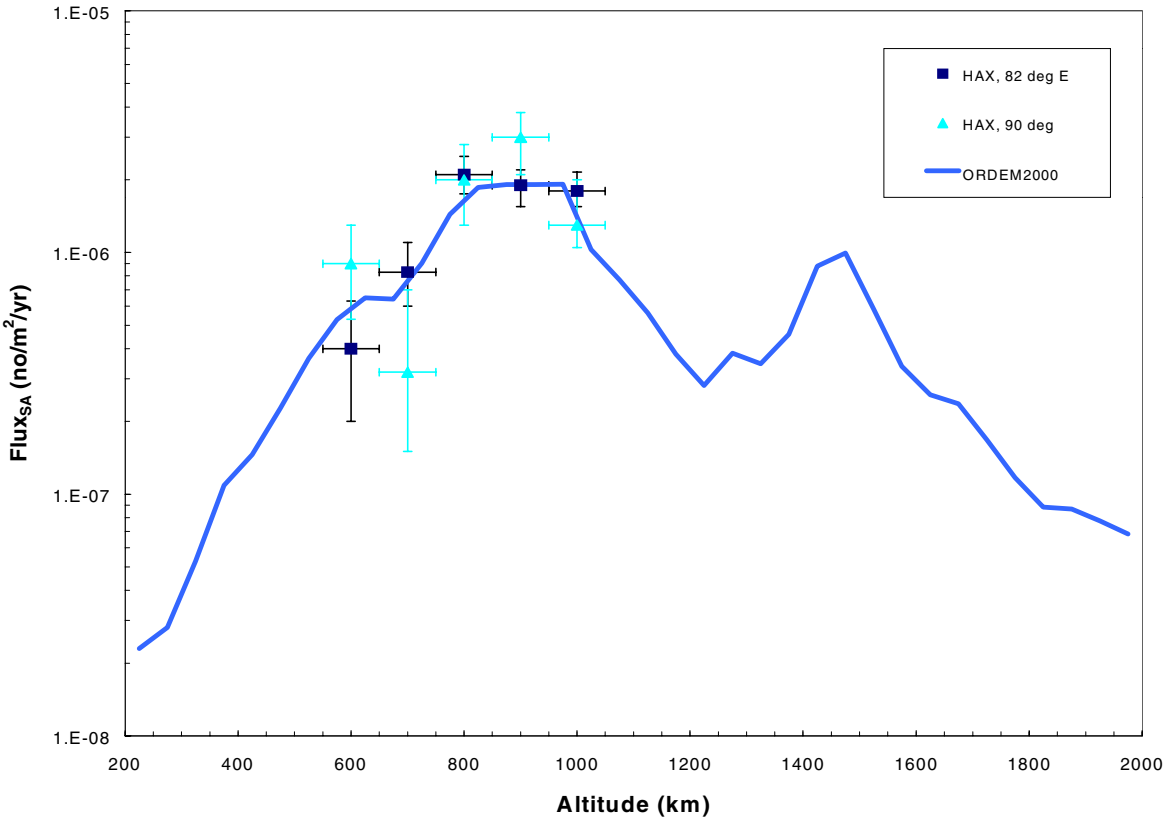

Figure 4-7: ORDEM2000 vs. HAX data (1998, objects ≥5 cm).

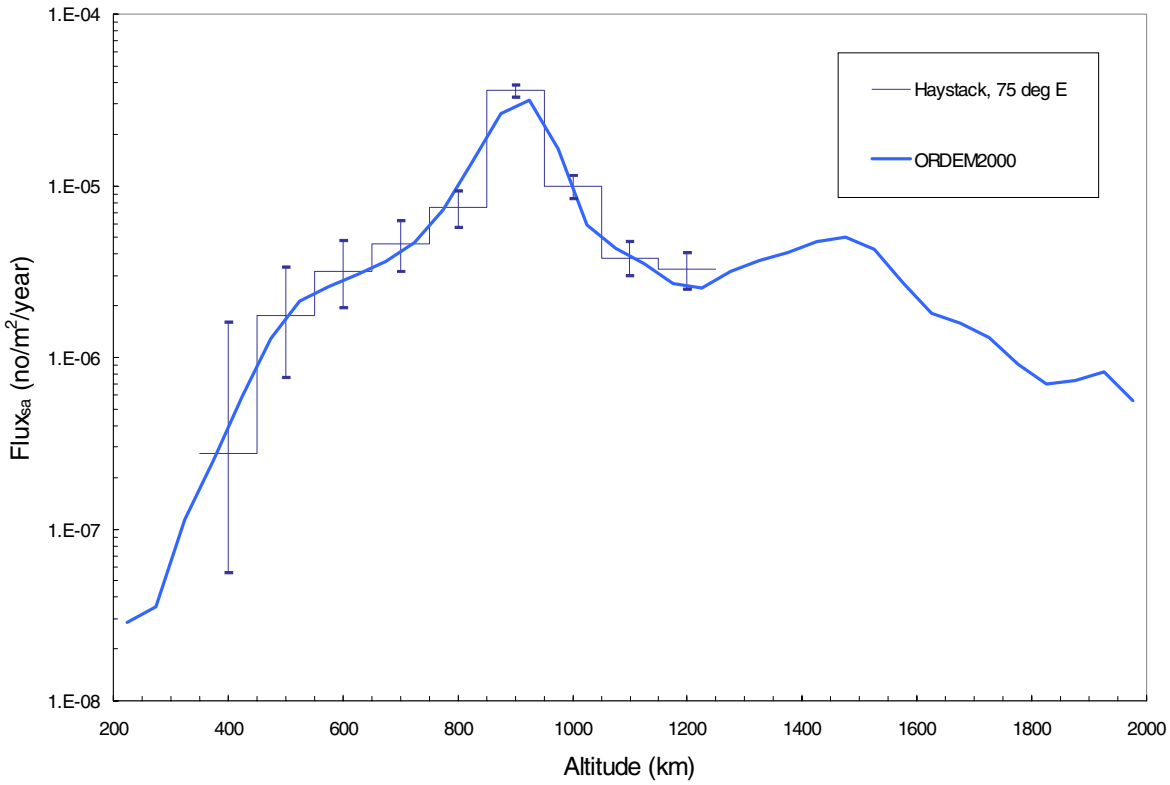

Figure 4-8: ORDEM2000 vs. Haystack data (1998, objects ≥1 cm).

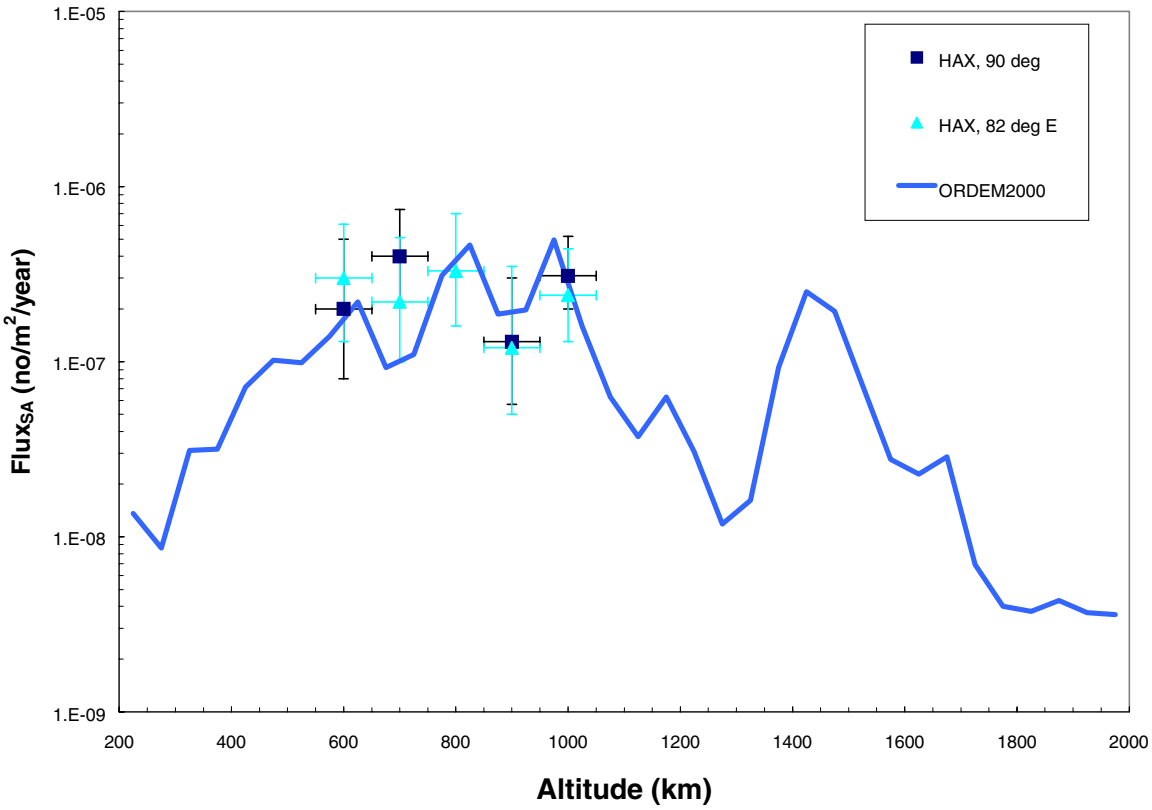

Figure 4-9: ORDEM2000 vs. HAX data (1997, objects ≥1 m).

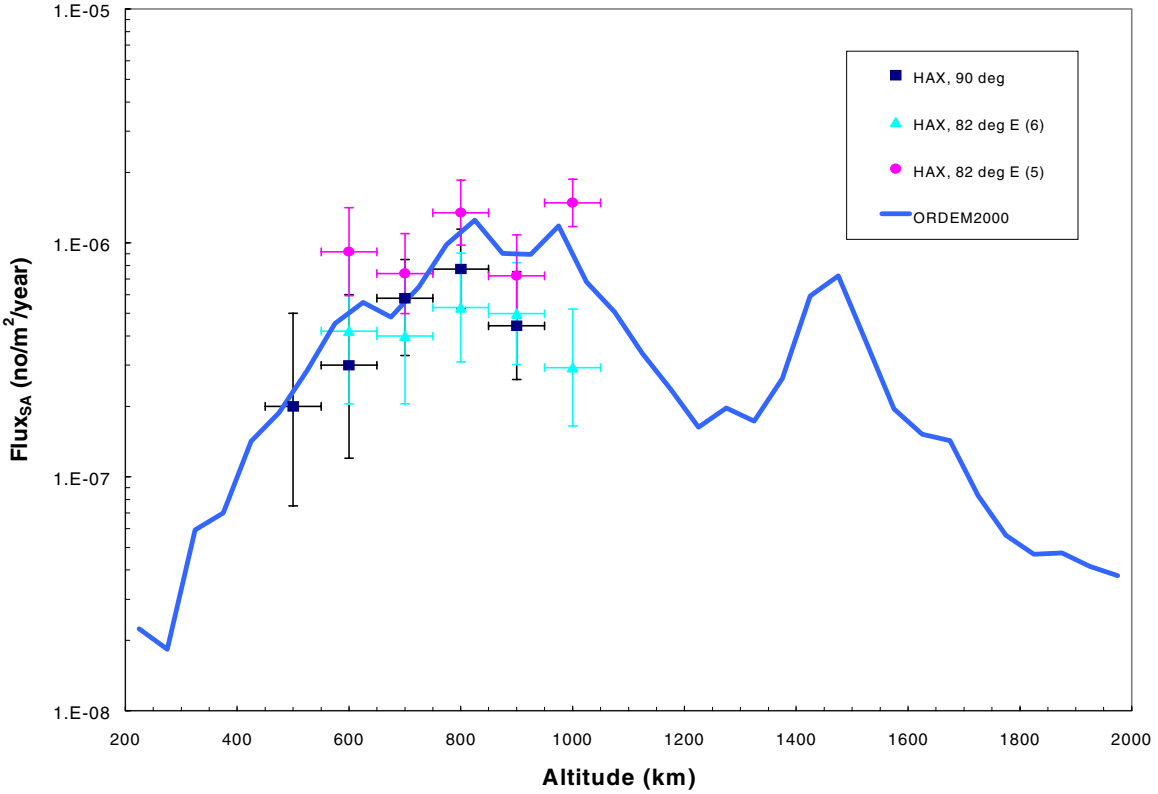

Figure 4-10: ORDEM2000 vs. HAX data (1997, objects ≥10 cm).

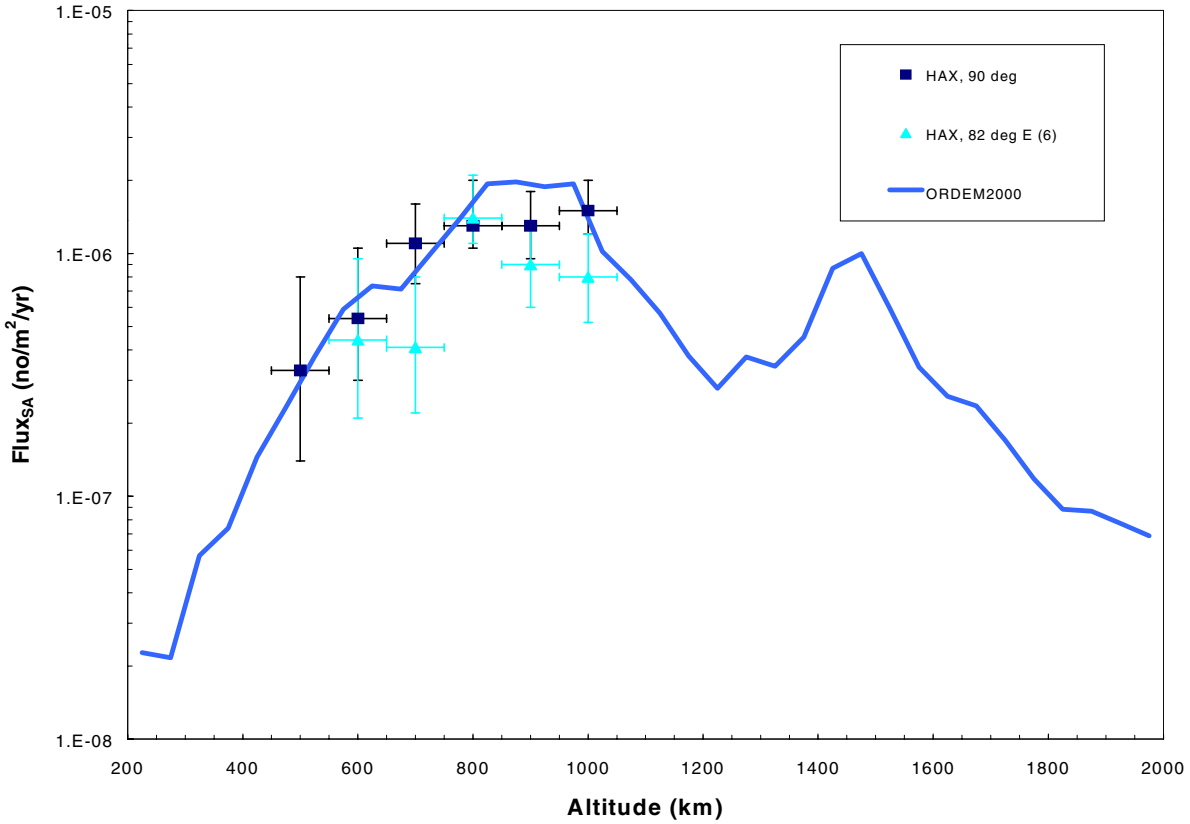

Figure 4-11: ORDEM2000 vs. HAX data (1997, objects ≥5 cm).

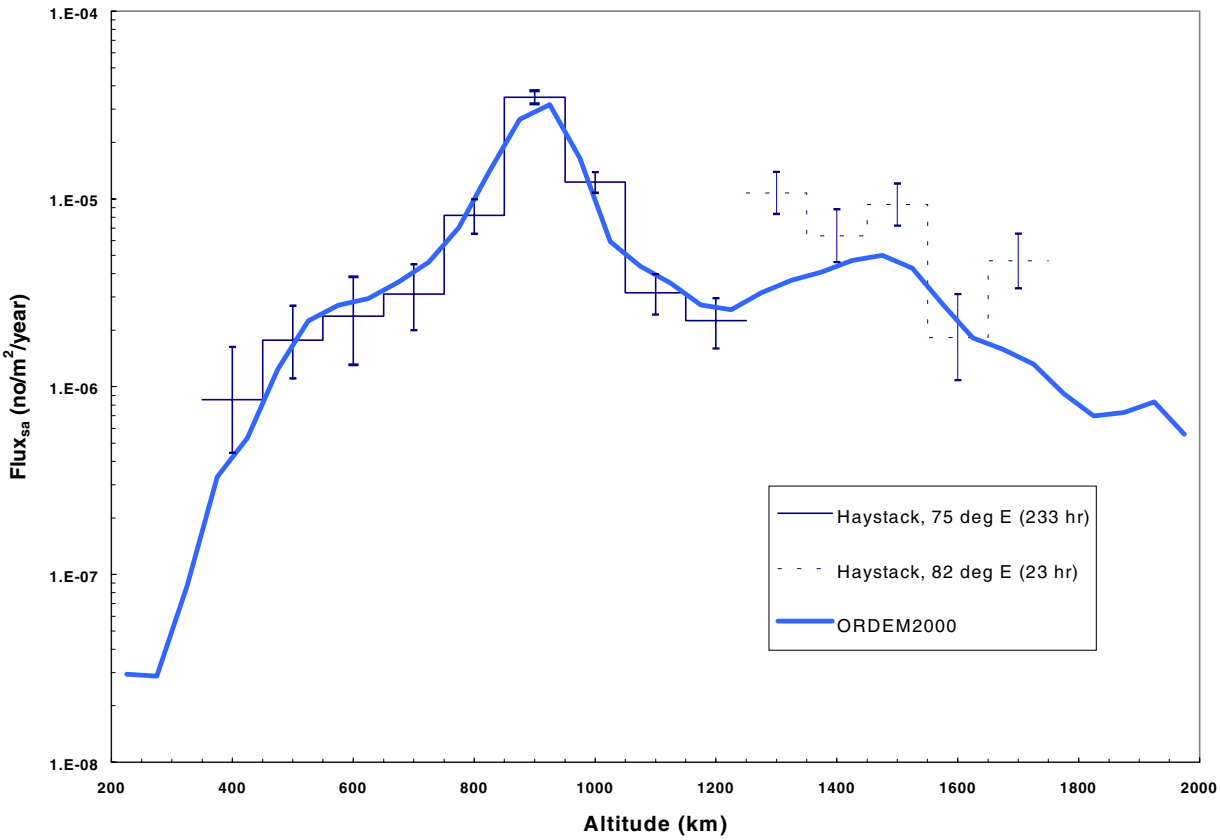

Figure 4-12: ORDEM2000 vs. Haystack data (1997, objects ≥1 cm).

4.2 Comparisons With In Situ Measurements

4.2.1 Space Shuttle

We can use the detailed timelines of the Shuttle missions in conjunction with ORDEM2000 to make predictions of the feature distribution. Figures 4-13 and 4-14 show the model fits after the empirical modifications described in Section 2.2.3.1.

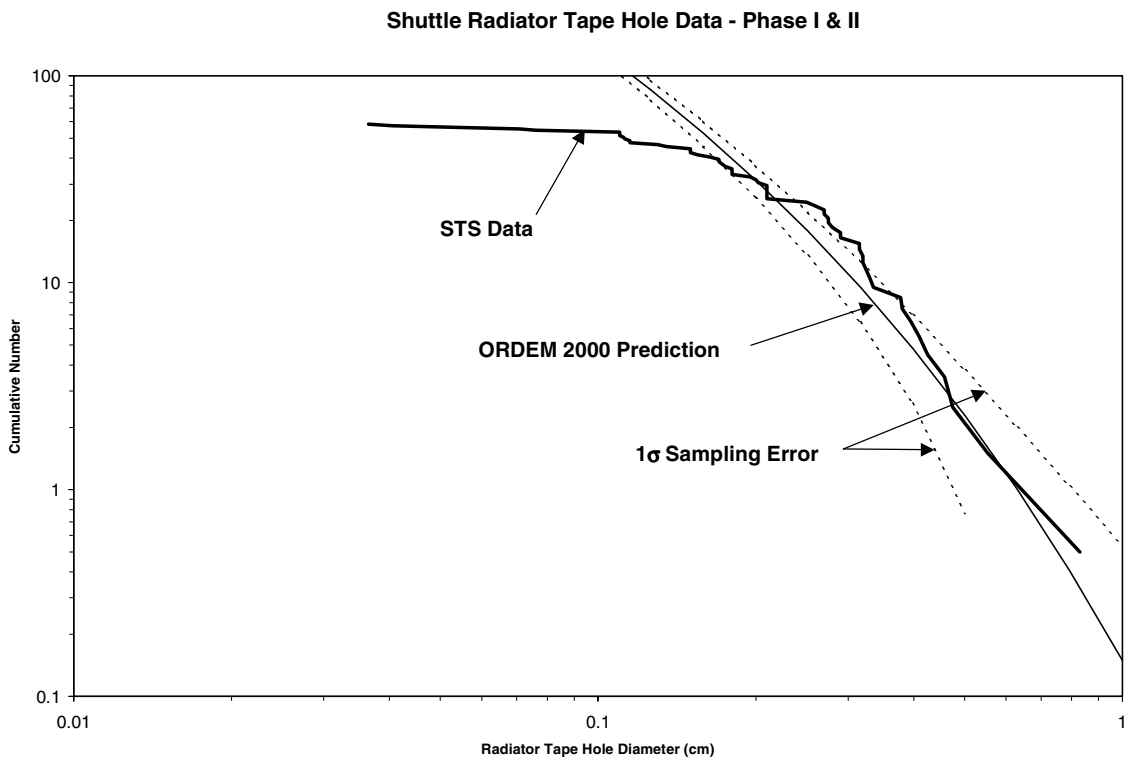

Figure 4-13: ORDEM2000 predictions of the Shuttle radiator tape-hole-diameter distributions. These data consist of those impacts known to be debris from their chemistry.

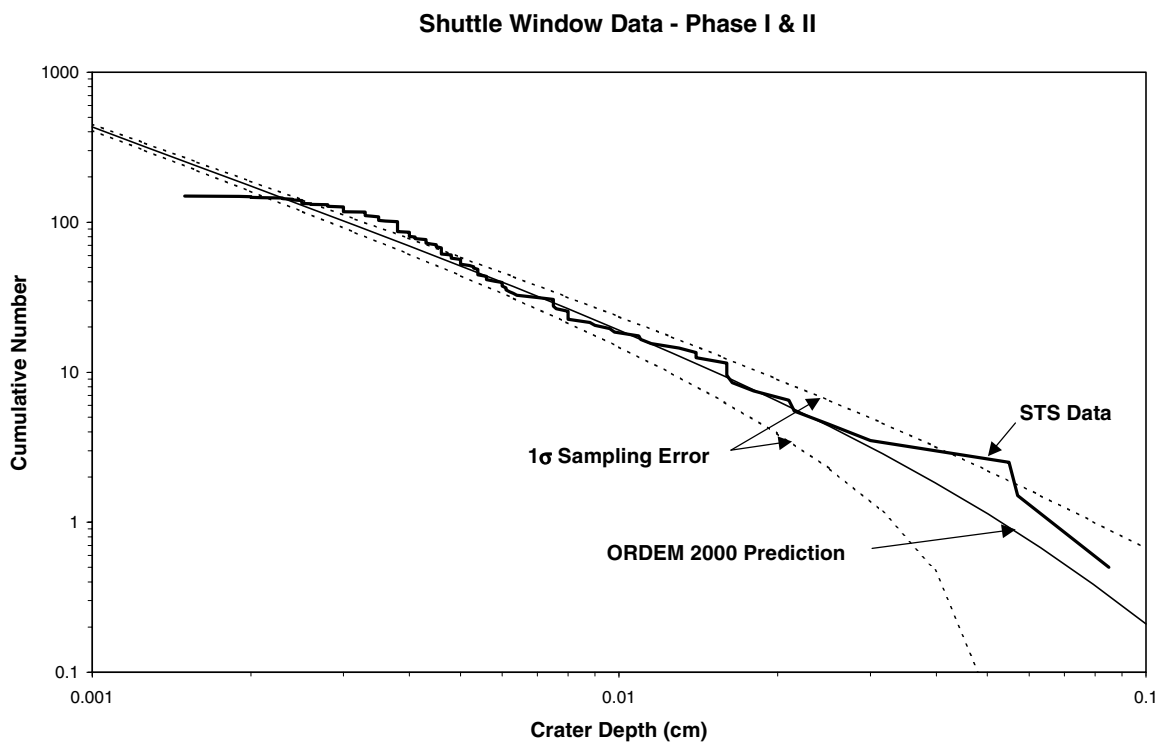

Figure 4-14: ORDEM2000 population predictions of the Shuttle window crater-depth distributions. These data consist of those impacts known to be debris from their chemistry.

4.2.2 HST Solar Array

Figure 4-15 shows the model fits to the HST-SA data. As described above, there are two fit regions. The semi-infinite assumption holds for features less than about 300 µm in size. The thin-target approximation holds for features larger than about 2 mm. Note that, for both curves, the model somewhat underpredicts the data, because the data do not have the meteoroids separated out. The resulting difference is consistent with our knowledge of the meteoroid environment.

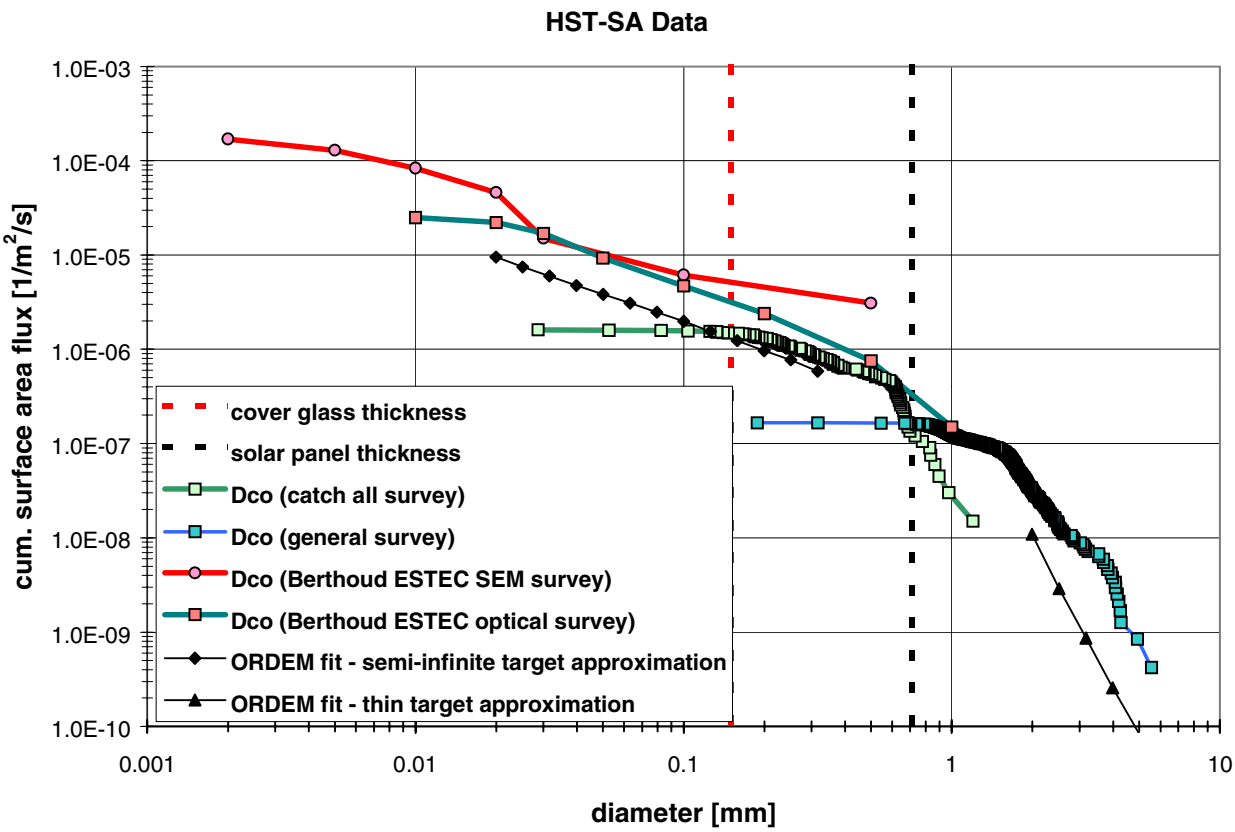

Figure 4-15: ORDEM2000 predictions of the HST conchoidal crater diameter (D_{co}) distributions. The two model curves represent the two cratering equation regimes described in the text. The data consist of both meteoroid and debris impacts, so the debris-only prediction is somewhat lower.

4.2.3 EuReCa Solar Arrays

Figure 4-16 shows the model fits to the EuReCa solar array data. As described above, the cratering equation for the semi-infinite approximation region is used. As with the HST-SA data, the data are a mixture of debris and meteoroids, so the debris-only model underpredicts the data.

Note that, for both HST-SA and EuReCa data, the model shows similar slopes. Qualitatively, the results are consistent with our knowledge of the relative contribution of the meteoroid flux.

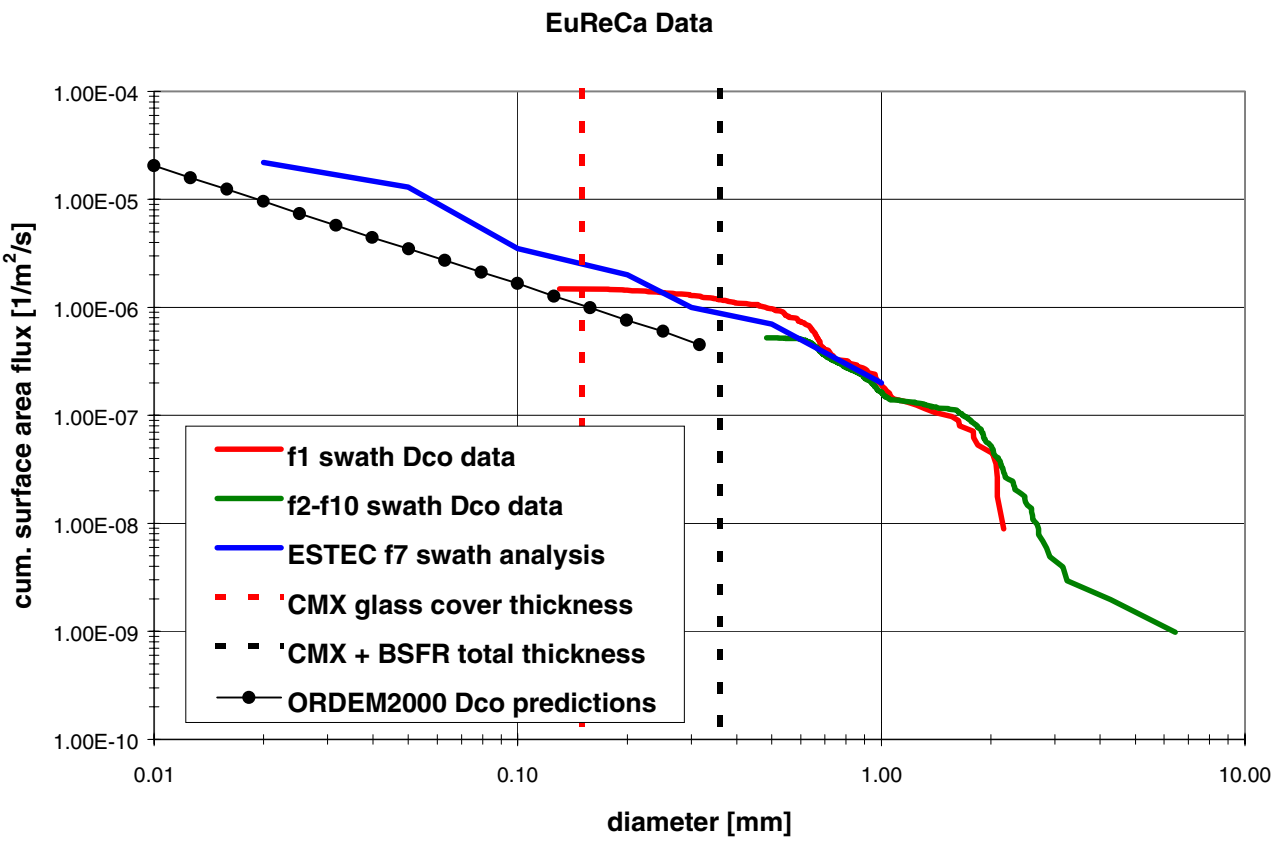

Figure 4-16: ORDEM2000 population predictions of the EuReCa conchoidal crater diameter (D_{co}) distributions. The data consist of both meteoroid and debris impacts, so the debris-only prediction is somewhat lower. The cratering equation is only good for D_{co} < 300 µm.

4.2.4 MEEP Experiment Aboard *Mir*

Figure 4-17 shows a comparison of MEEP's Plates 1 and 2 with ORDEM2000. As can be seen, ORDEM2000 is generally consistent with the MEEP data above 10 µm.

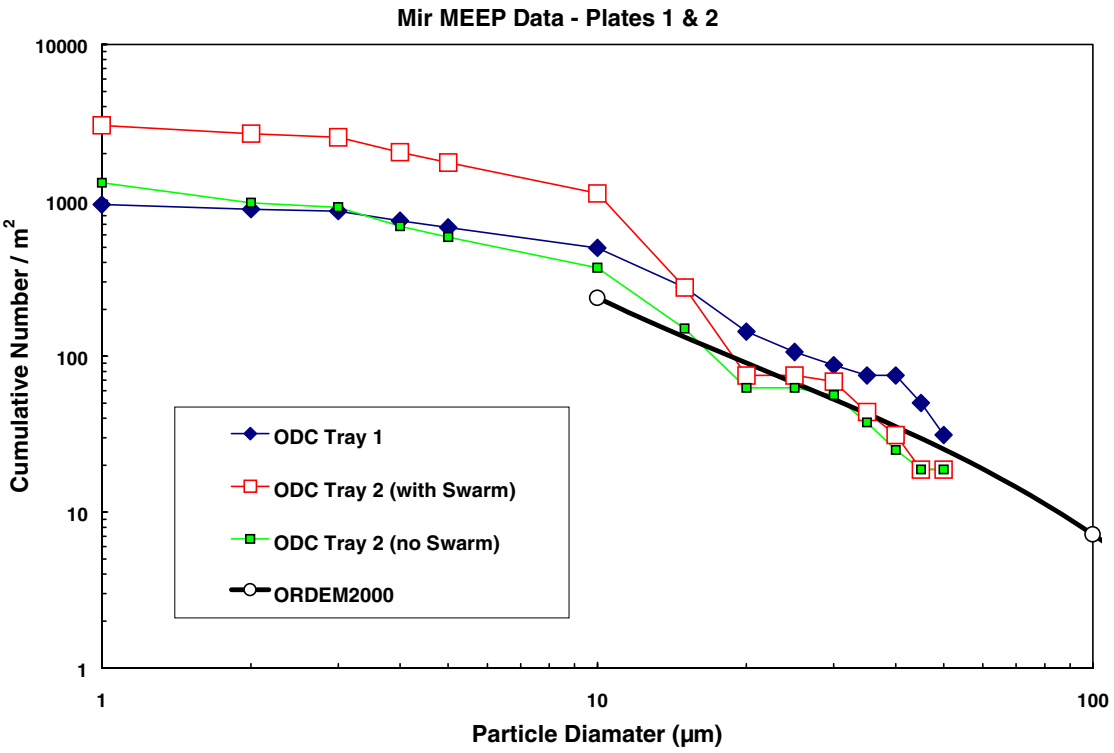

Figure 4-17: ORDEM population size predictions compared to the* Mir *MEEP size distribution estimates. There is, in general, good agreement.

4.3 Sensitivity Analysis

A potential problem with the ORDEM2000 finite element model for the environment is in the grid size of the cells. One can certainly make the cells smaller to increase the resolution. However, the physical size of the resultant template files may become unmanageably large. In addition, statistical noise will increase with decreasing grid size in a finite element model. It may produce unrealistic transitions between cells. On the other hand, one needs to make sure the grid size of the cells is sufficiently small to preserve important fine features in the environment. The template data files with the standard resolution in ORDEM2000 have a total physical size of about 14 MB. A sensitivity study has been performed to determine if the resolution is sufficient. New templates with (1 deg × 1 deg × 10 km) cell dimension and (0.1 km/sec × 1 deg) velocity distribution were created and implemented in the model. Average impact fluxes on a spacecraft with an ISS-type orbit (400 km × 490 km, 51.6-deg inclination, in 1999) were calculated using both the standard templates and the high-resolution versions. The comparison shows that there is no statistically significant difference between the two (Figure 4-18). Another study with a spacecraft of Shuttle-like orbit also shows similar results. These comparisons indicate that the grid size used in ORDEM2000 is reasonable.

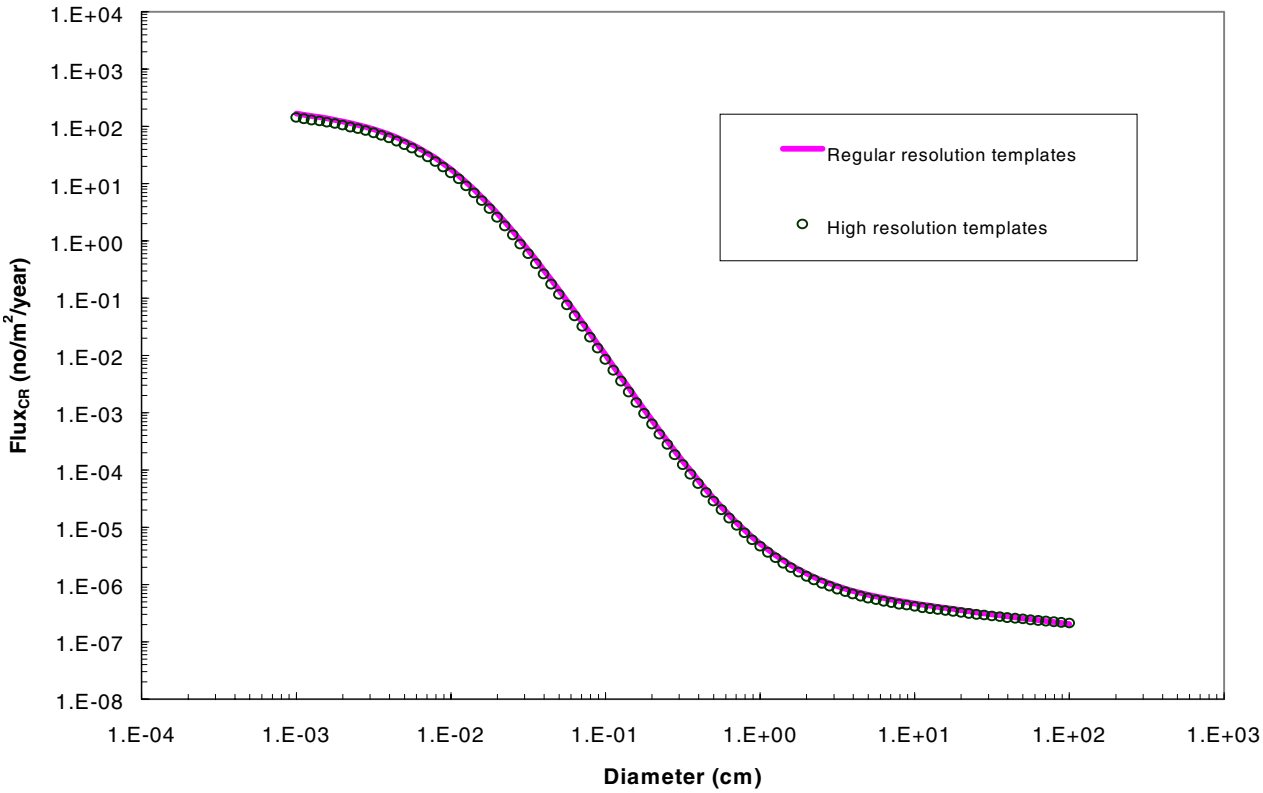

Figure 4-18: Predicted average cross-sectional area flux on a spacecraft with an ISS-type orbit. The difference between the prediction based on the ORDEM2000 regular resolution template files and that based on a special set of high-resolution template files is small.

5. ORDEM2000 Graphic User Interface

5.1 Introduction

ORDEM2000 has two major branches. The first one is for spacecraft and mission designers. The second branch gives orbital debris information as would be seen from a ground-based telescope or radar. Resultant plots and data files give estimates of object spatial density, flux, velocity, and inclination distributions.

The PC-based ORDEM2000 includes two programs, a GUI written in visual C++ and the main computational code written in FORTRAN. The template files that form the database of the model are stored in a subdirectory called "data." The user selects program options and enters input parameters using the GUI. The results of the FORTRAN computation are stored in a subdirectory named "results" but the location of the generated data files can be redirected to another directory for additional analyses.

The GUI graphing panels have a number of useful features worth mentioning. The output graph displayed within the GUI can be edited and exported to other programs. Each graphing panel offers the ability to alter the physical display by changing the labeling, the upper and lower bounds, and the scaling of the graph. Then the user can dump the graphic to the Windows clipboard, to the printer, or to a file. If the user is not pleased with the look of the graphic, the data underlying the graph can also be dumped to the Windows clipboard, to the printer, or to a file. The raw data results are tab-delimited for easy transfer into spreadsheets or visualization programs. The original files generated by the FORTRAN computation are also available.

5.2 Program Requirements

ORDEM2000 is designed to run on computers using Windows (95/98) and Windows NT. The expanded ORDEM2000 directory is around 16 megabytes. The GUI and FORTRAN program are both approximately 400 kilobytes.

5.3 Program Installation

Download the file called "ORDEM2000cmprss.zip" and double click on it or use a decompression program that recognizes zip files to install the program. The program can be installed on any of the local drives on your computer, in a directory path with no spaces. Downloading or decompressing the program will take several minutes. Further information can be found in the Readme.txt file in the ORDEM2000 directory.

5.4 Program Execution

As we indicated earlier, there are two ways to run the program: using the GUI and without the GUI. We will discuss each in turn.

5.4.1 Graphical User Interface-Based Computation

To start the GUI you need to double click the file "ORDEM2000.exe." A dialog panel like the one in Figure 5-1 should appear.

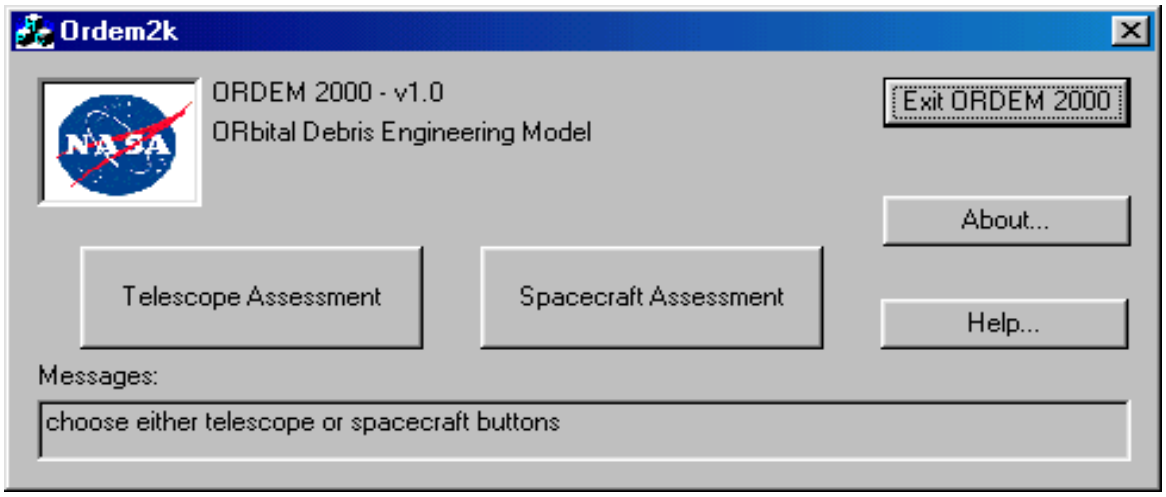

Figure 5-1: ORDEM2000 main panel.

Next, click on one of the various buttons to bring up additional dialog panels. The design of the program is such that you can only operate on the current, top-most window and you must exit it before you can operate on panels hidden beneath. Beyond the main panel are several basic panel types, most with a graphic icon in the upper left-hand corner, including Data Input panels, Computation Result panels, and Graphic Display panels.

We describe below two example sequences (telescope mode and spacecraft mode).

5.4.1.1 Example Telescope Assessment

Start up ORDEM2000.exe and in the main panel click on Telescope Assessment and the following panel should appear (Figure 5-2).

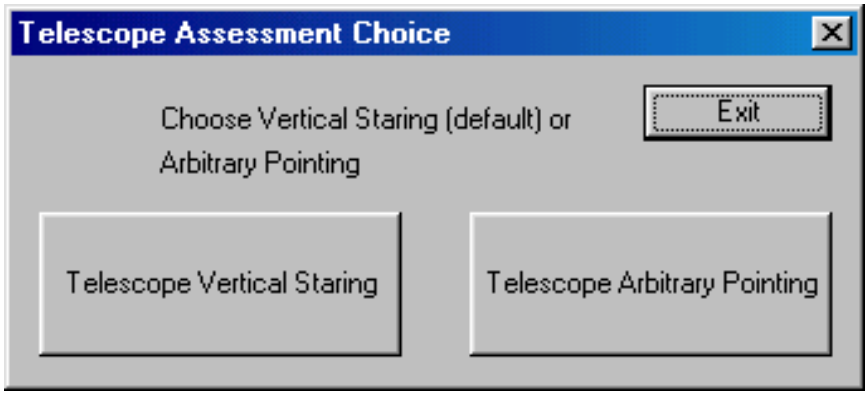

Figure 5-2: Telescope Assessment Choice panel.

Click on "Telescope Vertical Staring" to bring up the input panel, as in Figure 5-3.

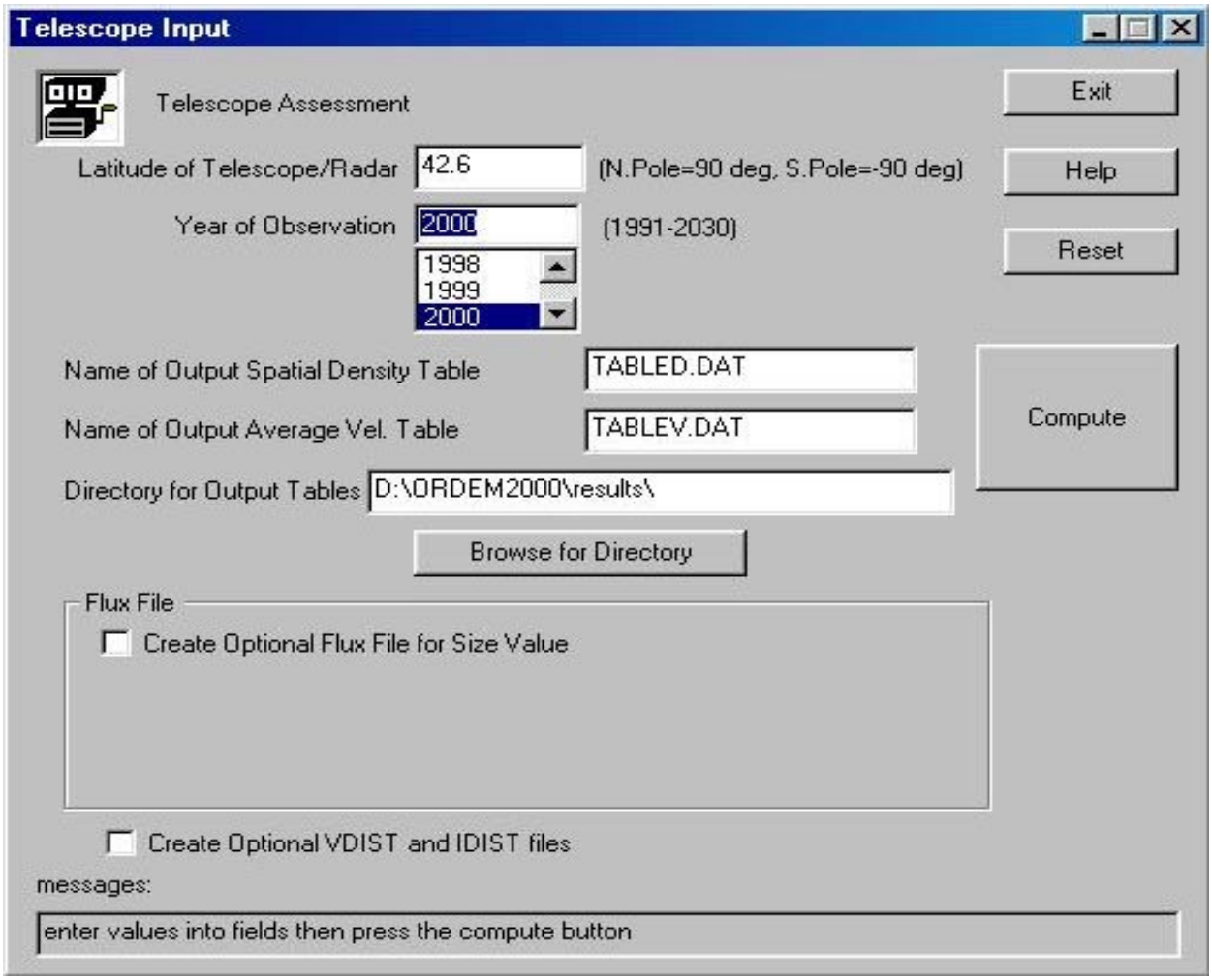

Figure 5-3: Telescope Input panel.

In this panel, you can input various variables. The program uses a complete set of default values for all variables so the computation can proceed with nothing other than pressing the large "Compute" button, or you can input new variables for any or all of the fields. One of the variables "Directory for Output Tables" can redirect the output files from the usual "results" subdirectory to any other directory on the computer. The directory listed in this field is where the Output Spatial Density and Output Average Velocity tables will be stored. Be aware that there are often data tables besides these two that are created and sent to the specified output directory. For example, if you click on "Create Optional Flux File for Size Value" or "Create Optional VDIST and IDIST files" you will get many additional files.

Once you have finished inputting parameters, press the "Compute" button and a DOS window will come up (Figure 5-4). This is the core FORTRAN computational code. It will show a percent progress line and, when finished, will give out some information concerning the files it has created. If you are using the GUI, you need not concern yourself with this information. To exit this window you need to hit Enter, which will cause the FORTRAN program to exit and return you to the GUI. If you get back the original input panel, you may see an error listing in the message text field at the bottom of the panel.

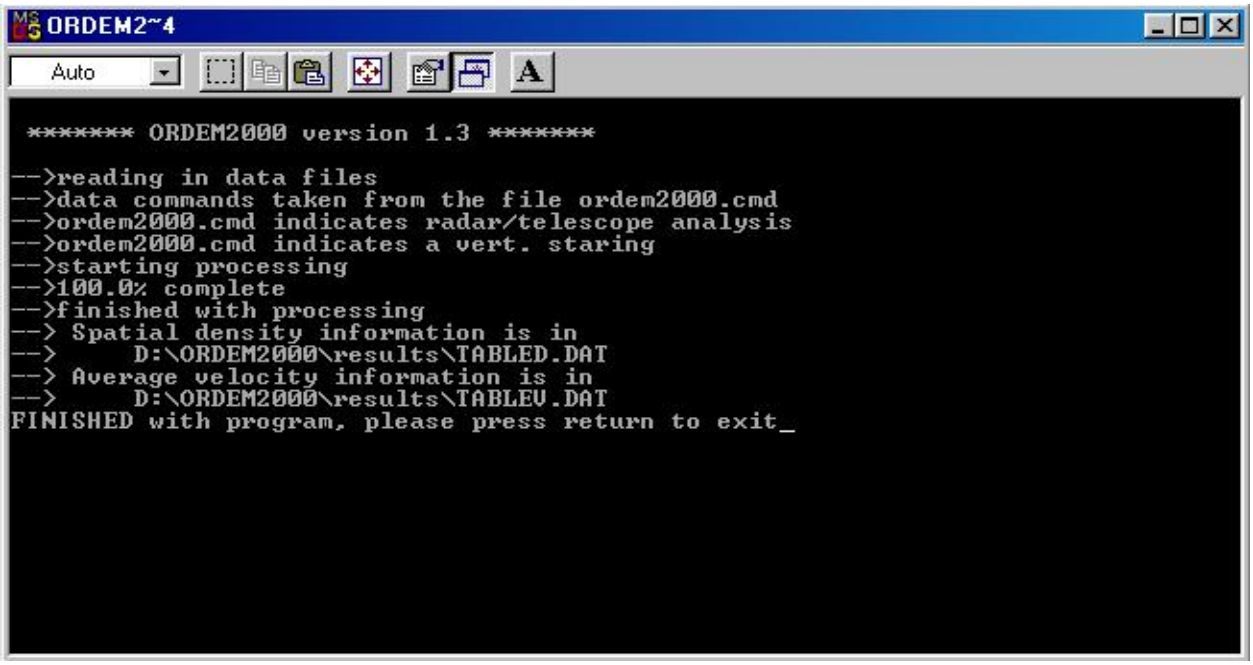

Figure 5-4: ORDEM2000_fort.exe window.

If the computation was successful, a new results panel will show up like that in Figure 5-5. In the results panel with the OK icon, you choose what results of the computation to graph. Select additional options here and move on to the last major panel type—a graph, or output, window. Figure 5-5 shows three large graph buttons, "Graph Vel Dstrb," "Graph Density," and "Graph Avg. Vel,"

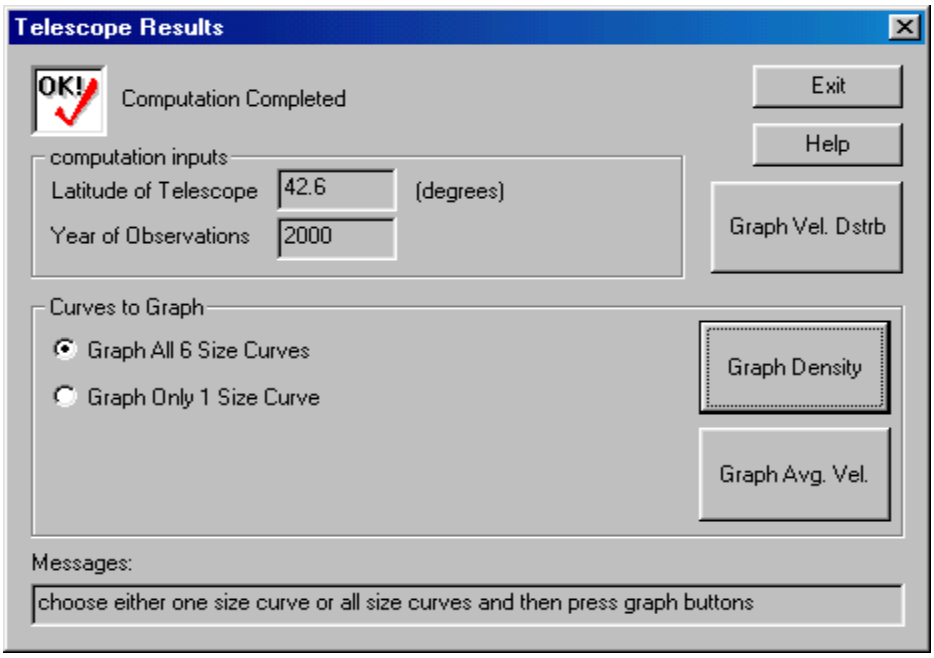

Figure 5-5: Telescope Results window.

The next step is to press the "Graph Density" button to bring up the panel in Figure 5-6.

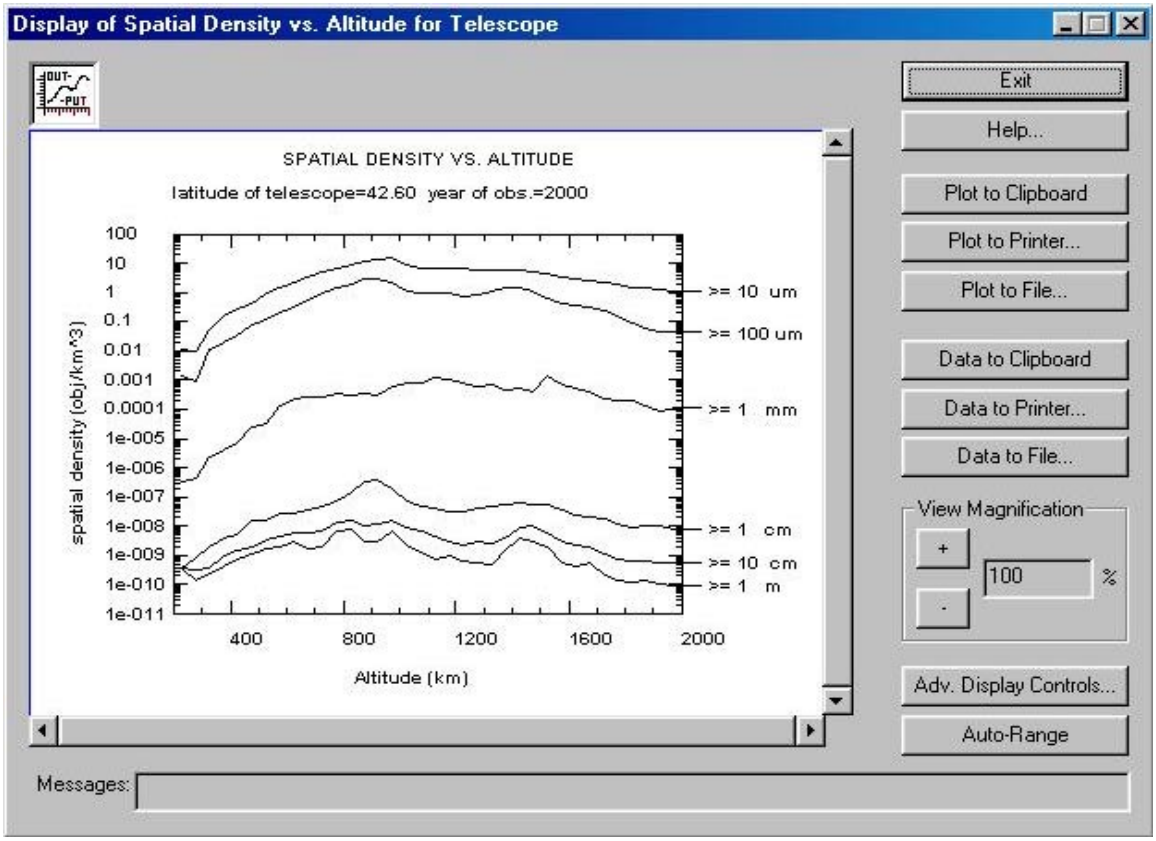

Figure 5-6: Display of Spatial Density vs. Altitude for Telescope.

The graph is displayed to the left and additional options are found on the right. Note that there are three "Plot to" buttons and three "Data to" buttons. The "Plot to" buttons copy the actual graphic as a series of line drawing commands to the Windows clipboard or to a file. In contrast, the "Data to" buttons send the actual numeric data that generated the plot to the same locations. The Data is tab-delimited, which means that it can be pasted directly into an Excel-style spreadsheet. Also of note is the "Advanced Display Controls" button, which allows you to change the title, labels, boundaries, and scaling of the plot, and the "Auto Range" button, which scales the plot so that the complete range of Y axis values is visible.

There are other panels besides inputs, results, and graphs, but they will not be discussed here. All but the most simplistic panels have a "Help" button with context-sensitive on-line documentation of what all the fields on that panel mean.

5.4.1.2 Spacecraft Assessment

Restart ORDEM2000.exe and, at the first main panel (Figure 5-2), click on Spacecraft Assessment. The panel in Figure 5-7 will appear.

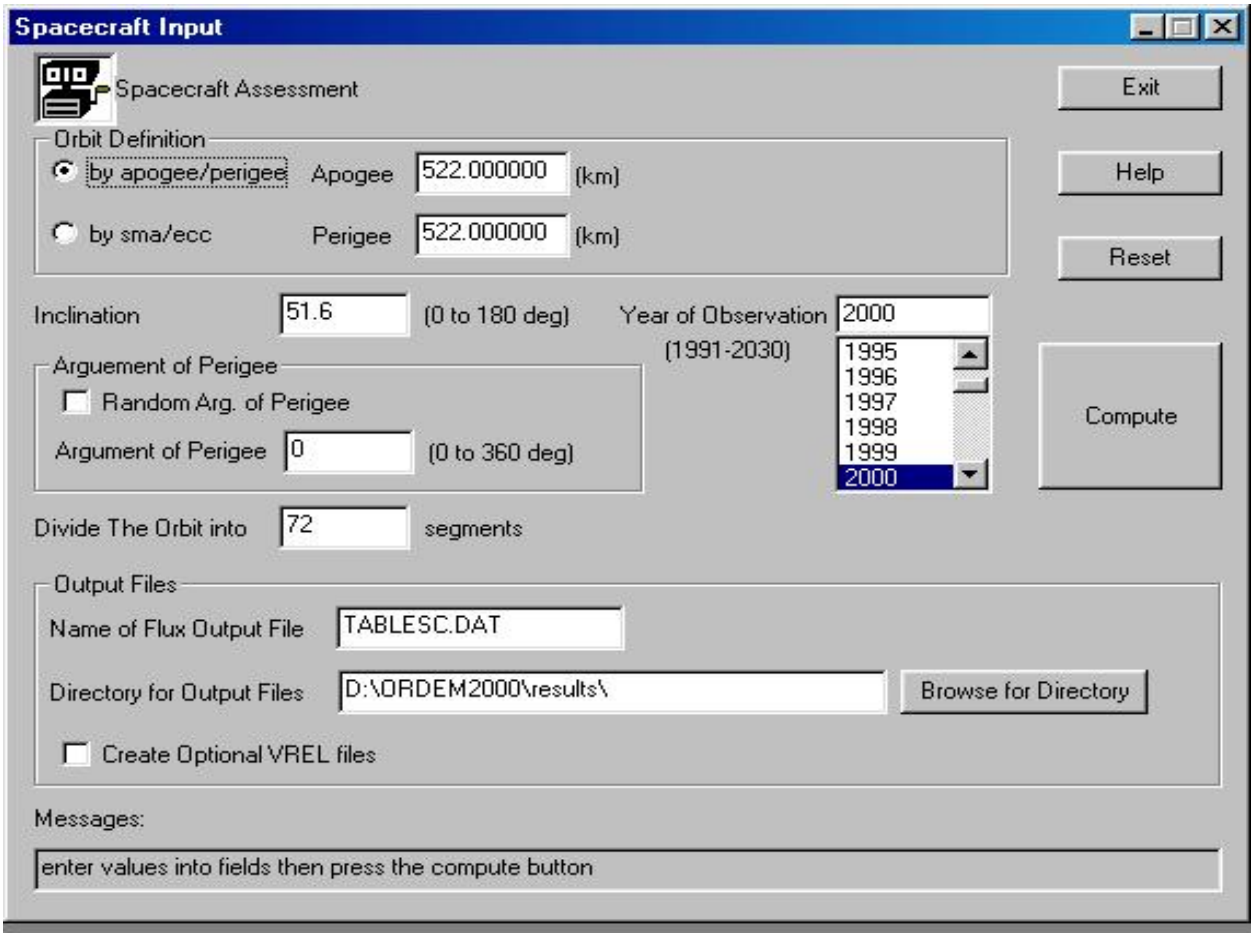

Figure 5-7: Spacecraft Assessment panel.

Once again, this panel is where input parameters are selected/entered. The user can select to define the orbit by semimajor axis and eccentricity or by apogee altitude and perigee altitude. The user can also enter other orbital elements and select the name of the output flux file and its location. Click on the Compute button to start the FORTRAN computation and you will see a DOS panel much like that found in Figure 5-8.

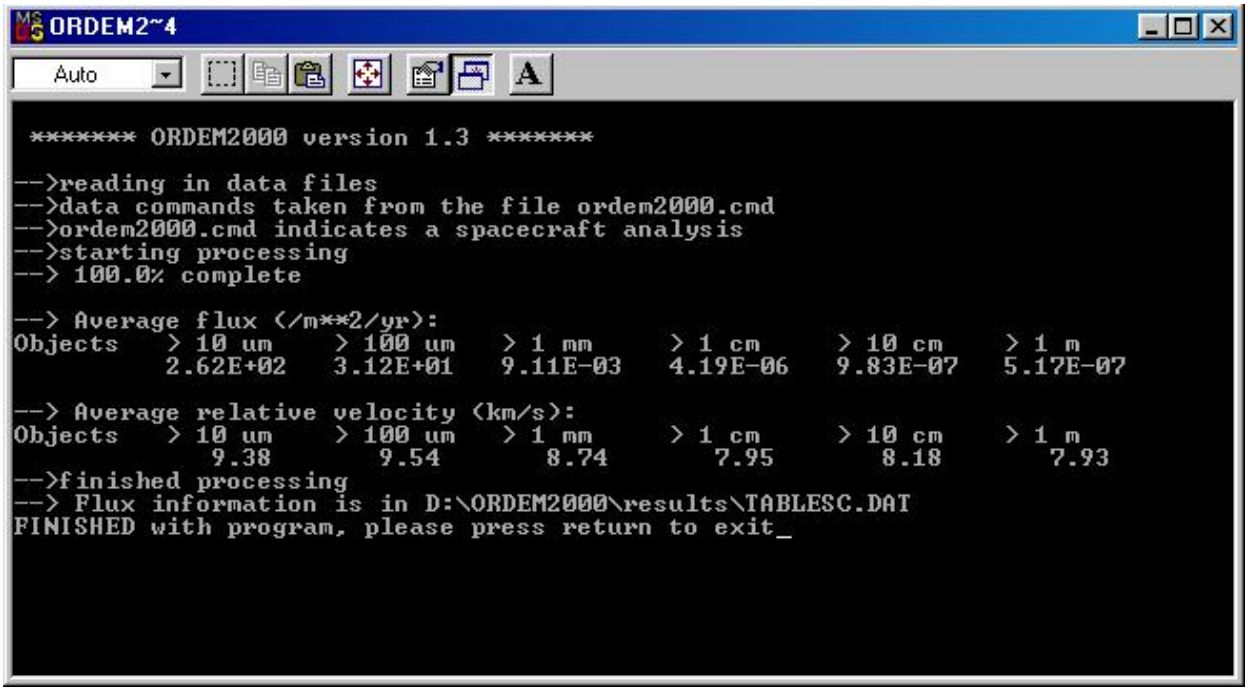

Figure 5-8: DOS computation panel.

Hit Return on the keyboard and, if the computation has gone correctly without error, the panel in Figure 5-9 will appear.

Two major graphs can be drawn from this results panel. You can graph a summary graph of average flux versus size of the debris by pressing on the "Graph Avg. Flux vs. Size" button (Figure 5-10). The more complicated graph is reached by clicking on the "Graph Flux over Orbit" button but before you do, notice the parameters that are in the same line drawn, grouping "Flux over Orbit Path." One can trace a flux curve for all debris of size greater than 10 μm to greater than 1 m. You can choose to plot all these curves at once or, if that produces too dense a graph, just one of the curves at a time. These plots can also be plotted versus a number of different orbital approaches. First, you can plot against orbital position. For high inclination orbits or high eccentricity orbits, you may want to plot against latitude or altitude.

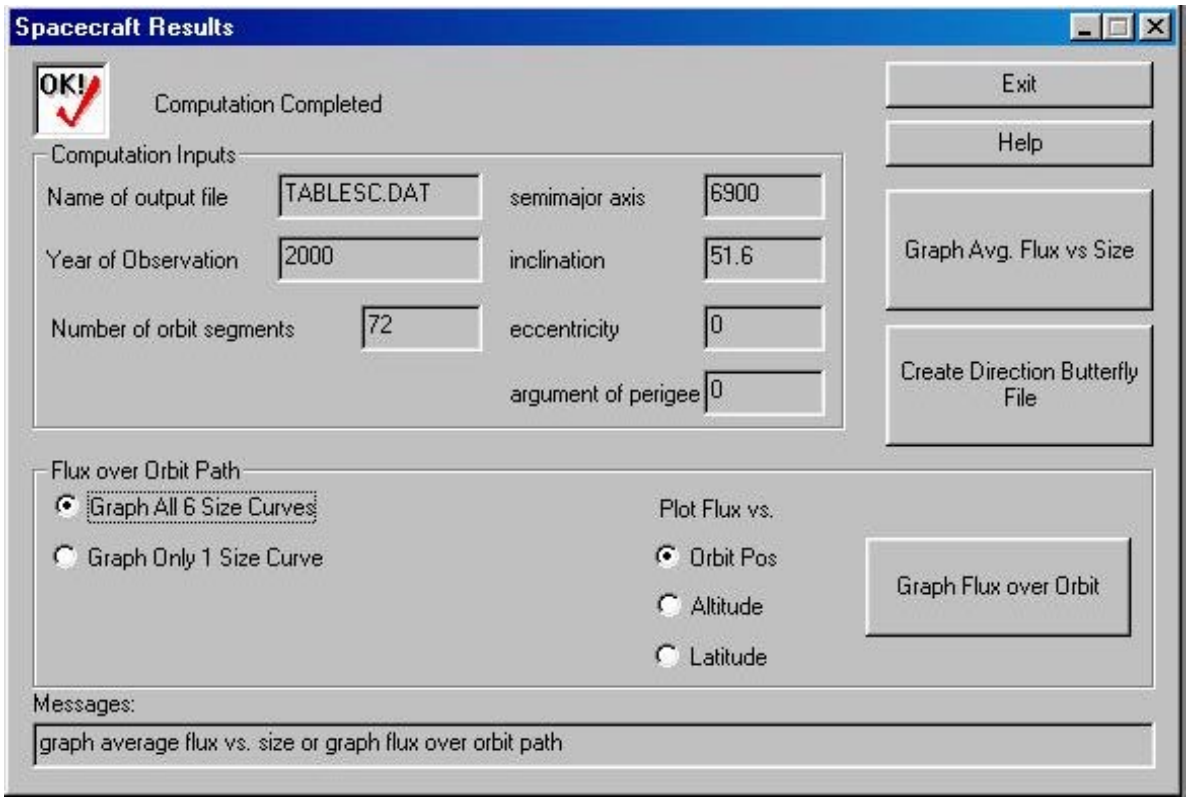

Figure 5-9: Computation completed panel for the spacecraft mode.

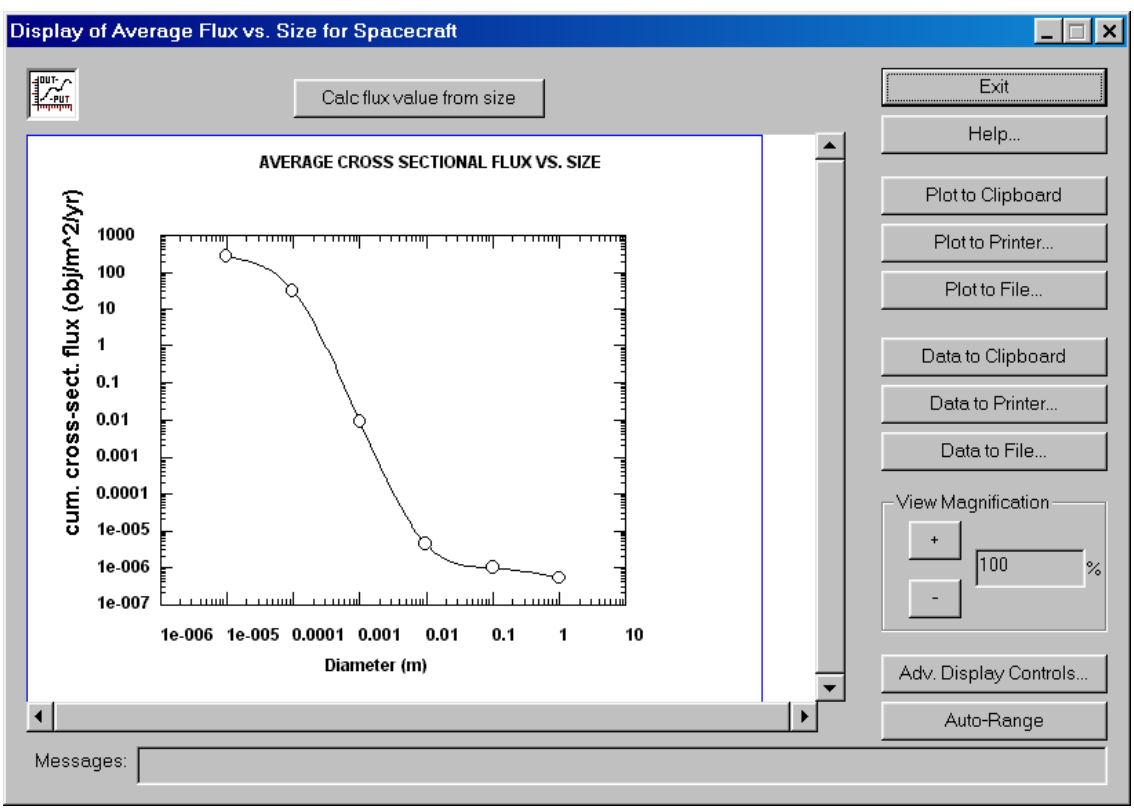

Figure 5-10: Graph of flux over orbit.

You can customize the look of this graph by adjusting the “Adv. Display Controls” button and the “Auto-Range” button.

Going back to the panel in Figure 5-9, pressing the “Create Direction Butterfly File” button will create the “Butterfly” file BUTTERFLY.DAT that summarizes the flux on a spacecraft broken out by yaw direction and relative velocity.

5.4.2 DOS-Based Computation

ORDEM2000 also allows for a second kind of computation where one completely bypasses the GUI and runs the program from DOS. This offers several advantages. First, those users who are more comfortable with DOS need not concern themselves with the GUI. Second, advanced users who are not interested in the simplistic graphs and want to create their own graphs or analyze some of the background output data files need not concern themselves with the GUI.

To understand this scripting basis, it is necessary to understand the communication between the GUI and the FORTRAN computation component. When the GUI is started, the program “ORDEM2000.exe” is loaded into memory and runs. When the input data is gathered together, it is written to a command text file called “ORDEM2000.cmd”. Next, the GUI starts up the FORTRAN program “ORDEM2000_fort.exe” and goes to sleep. The FORTRAN component immediately looks for “ORDEM2000.cmd,” reads it in, executes its commands, and creates the large number of output files in the designated results directory. When finished, it waits for the user’s “Enter” key command, and then quits execution. The GUI then reawakens and looks for the presence of a file “ORDEM2000.res” (res for results) which indicates that computation has finished. If there is no such file, an error is reported. If the file is present, the GUI assumes completion and goes on with its actions.

With this in mind, one can easily run the program in a DOS window. Simply edit the “ORDEM2000.cmd” file to the desired values and then enter the command “ordem2000”. There are actually two versions of this for Fortran computational DOS program. Version 1, ORDEM2000_fort.exe, runs with the GUI and requires the user to press the Enter key to terminate. Version 2, ordem2000.exe, has no Enter key and so will be useable for full DOS scripting. One can then run the program countless times by creating a DOS script and copying various files into “ORDEM2000.cmd” as needed.

There are several example cmd files provided in the distribution. See sc_ordem.cmd, tel_ordem.cmd, and tel2_ordem.cmd and use them as templates. Sc_ORDEM2000 is an example of spacecraft style assessment. Tel_ORDEM2000.cmd is a typical vertical staring telescope-type analysis and tel2_ORDEM2000.cmd is an example for an arbitrary pointing telescope analysis. These three files reflect the three major branches of panels inside the GUI as well. A rudimentary DOS batch file that does an example scripting is included, called “test_script.bat”.

5.5 Output Data File Names in the Program

Table 5-1 lists information on the various output files found in the results directory. There are three major branches of analysis in ORDEM2000, Spacecraft, Telescope Vertical Stare, and Telescope Arbitrary Pointing. Some of these files can be renamed within the program and some names are fixed. After being created, some of the files can be displayed or graphed within the program; others are for advanced users and are not graphed.

Some mention should be made concerning the name of certain groups of files. For example, the Telescope Vertical Staring computation creates a family of files with the name VDISTxyy.DAT where x and yy are actually variables distinguishing the files. The "x" indicates the size class. It ranges from "1" for 10 µm and greater to "2" for 100 µm and greater to "6" for 1 m and greater. The yy variable indicates the altitude bin from "1" for 200 km to "2" for 250 km to "36" for 1950 km. The same naming system is used for the IDIST files as well.

Table 5-1: Output Data Files

Type of Analysis	File Renameable?	File Graphed	File Name	Description
Telescope Stare	Yes	Yes	TABLED.DAT	Spatial density as a function of altitude and object size
Telescope Stare	Yes	Yes	TABLEV.DAT	Average orbital velocity as a function of altitude and object size
Telescope Stare	Yes	No	TABLEF.DAT	Surface area flux as a function of altitude of objects of a given size
Telescope Stare	No	Yes	VDISTxyy.DAT	Velocity distribution. x=size class yy=altitude range
Telescope Stare	No	No	IDISTxyy.DAT	Inclination distribution. x=size class yy=altitude range
Telescope Point	Yes	No	TABLEFX.DAT	Surface area flux as a function of altitude and size
Spacecraft	Yes	Yes	TABLESC.DAT	Impact flux on the spacecraft along its orbit
Spacecraft	No	No	VRELzzzz.DAT	Velocity components of the spacecraft and objects at zzzz-th location along the orbit
Spacecraft "Butterfly"	No	No	BUTTERFLY.DAT	Breakdown of fluxes in yaw direction and relative velocity bins in the spacecraft frame

6. References

Bate, R.R., et al., 1971. Fundamentals of Astrodynamics. Dover, New York.

Burt R.R., and E.L. Christiansen, 2001. Hypervelocity Impact Tests on Hubble Space Telescope (HST) Solar Array Cells, NASA JSC-28307.

Christiansen, E.L., 1998. Orbiter Meteoroid/Orbital Debris Impacts: STS-50 (6/92) through STS-86 (10/97), NASA JSC-28033.

Cour-Palais, B.G., 1985. Hypervelocity impact investigations and meteoroid shielding experience related to Apollo and Skylab. In Orbital Debris (D.J. Kessler and S-Y Su, Eds.), NASA CP-2360.

Drolshagen, G., et al., 1996. Optical survey of micrometeoroid and space debris impact features on EuReCa, Planet. Space Sci. **44**.

Drolshagen, G., et al., 1997. HST solar array impact survey: Revised damage laws and residue analysis, Adv. Space Res. **19**.

Drolshagen, G., 1997. Personal communication.

Efron, B., 1982. The Jackknife, the Bootstrap, and Other Resampling Plans, CBMS-NSF Regional Conference Series in Applied Mathematics, 38.

Fechtig, H., et al., 1977. Microcraters on lunar samples. In The Soviet-American Conference on Cosmochemistry on the Moon and Planets (J.H. Pomeroy and N.J. Hubbard, Eds.), NASA SP-370 part 2.

Gault, D.E., et al., 1972. Effects of microcratering on the lunar surface, Geochimica et Cosmochimica Acta, Supplement 3, **3**.

Goldstein, R.M., et al., 1998. Radar observations of space debris, Planet. Space Sci. **46**.

Graham, G.A., et al., 2000. Impact damage to space hardware: Identifying the culprits, Microscopy and Analysis.

Grün, E., et al., 1985. Collisional balance of the meteoric complex, ICARUS **62**.

Hörz, F., et al., 1991. Preliminary analysis of LDEF instrument A0187-1 “chemistry of micrometeoroid experiment.” In LDEF-69 months in space: First post-retrieval symposium (A.S. Levine, Ed.), NASA CP-3134.

Hörz, F., et al., 1992. Preliminary analysis of LDEF instrument A0187-1, the chemistry of micrometeoroid experiment (CME). In Hypervelocity Impacts in Space (J.A.M. McDonnell, Ed.), University of Kent at Canterbury Press.

Hörz, F., et al., 1994. Cratering and Penetration Experiments in Teflon Targets at Velocities from 1 to 7 km/s, NASA TM 104979.

Hörz, F., et al., 1995. Penetration Experiments in Aluminum 1100 Targets Using Soda-Lime Glass Projectiles, NASA TM-104813.

Hörz, F., et al., 1999. Optical Analysis of Impact Features in Aerogel From the Orbital Debris Collection Experiment on the *Mir* Station, NASA TM-1999-209372.

Humes, D.H., 1991. Large craters on the meteoroid and space debris impact experiment. In LDEF-69 months in space: First post-retrieval symposium (A.S. Levine, Ed.), NASA CP-3134.

Humes, D.H., 1993. Small craters on the meteoroid and space debris impact experiment. In LDEF-69 months in space: Third post-retrieval symposium (A.S. Levine, Ed.), NASA CP-3275.

Humes, D.H., 1998. MEEP Polished Plate Meteoroid and Debris Experiment—Craters in the Aluminum Alloy (6006-T-) Plate, MEEP Archive System, NASA Langley Research Center.

Hyde, J.L., et al., 2000a. As-Flown Shuttle Orbiter Meteoroid/Orbital Debris Assessment, Phase I, JSC-28768.

Hyde, J.L., et al., 2000b. As-Flown Shuttle Orbiter Meteoroid/Orbital Debris Assessment, Phase II, JSC-29070.

Johnson, N.L., et al., 2000. NASA's new breakup model of EVOLVE 4.0, Adv. Space Res., Vol. 28, No. 9, pp. 1377-1384, 2001.

Kessler, D.J., 1981. Derivation of the collision probability between orbiting objects: The lifetimes of Jupiter's outer moons, ICARUS **48**.

Kessler, D.J., 1984. Orbital Debris Environment for Space Station, JSC Internal Note 20001.

Kessler, D.J., et al., 1989. Orbital Debris Environment for Spacecraft Designed to Operate in Low Earth Orbit, NASA TM-100471.

Kessler, D.J., et al., 1991. Meteoroids and orbital debris. In Space Station Program Natural Environment Definition for Design, NASA SSP-30425/Rev. A.

Kessler, D.J., et al., 1996. A Computer-Based Orbital Debris Environment Model for Spacecraft Design and Observation in Low Earth Orbit, NASA TM-104825.

Krisko, P.H., et al., 2000. EVOLVE 4.0 User's Guide and Handbook, LMSMSS-33020.

Kuriki, K., et al., 1997. Meteoroid and space debris impact investigations in SFU post flight analysis activities: Preliminary results and further directions, the Institute of Space and Astronautical Science (ISAS) Report No. 666.

Levine, A.S. (Ed.), 1991. LDEF—69 months in space: The first post-retrieval symposium, NASA CP-3134.

Levine, A.S. (Ed.), 1992. LDEF—69 months in space: The second post-retrieval symposium, NASA CP-3194.

Levine, A.S. (Ed.), 1993. LDEF—69 months in space: The third post-retrieval symposium, NASA CP-3275.

Maag, C., 1996. Debris Clouds Indicated by ESEF Data From *Mir*, SFE Newsletter 7, No. 1.

Mandeville, J.C. and M. Bariteau, 2000. Cosmic dust and micro-debris measurements on the *Mir* space station, COSPAR 2000, in press.

Matney, M., et al., 1999. Recent results from Goldstone orbital debris radar, Adv. Space Res. **23**.

Matney, M., 2000, A New Approach to Applying Interplanetary Meteoroid Flux Models to Spacecraft in Gravitational Fields, Proceedings of IAU Colloquium 181/COSPAR Colloquium 11, in press.

McDonnell, J.A.M., et al., 1998a. Meteoroid and debris flux and ejecta models: Summary report, ESA Contract No. 11887/96/NL/JG.

McDonnell, J.A.M., et al., 1998b. Meteoroid and debris flux and ejecta models: Final report, ESA Contract No. 11887/96/NL/JG.

Neish, M.J., 2001. Personal communication.

Neish, M.J. and S. Kibe, 2001. Hypervelocity impact damage equations for Kapton multi-layered insulation and teflon second surface Mirrors, Proceedings of the 3rd European Space Debris Conference, ESA SP-473.

Paul, K.G., E.B. Igenbergs, and L. Berthoud, 1997. Hypervelocity impacts on solar cells—observations, experiments, and empirical scaling laws, Int. J. Impact Engng. **20**.

Press, W.H., et al., 1992. Numerical Recipes in Fortran 77, 2nd edition, Cambridge Press.

Sachs, L., 1984. Applied Statistics: A Handbook of Techniques. 2nd edition, Springer-Verlag, New York.

Sdunnus, H., et al., 2001. The ESA MASTER'99 space debris and meteoroid reference model, Proceedings of the 3rd European Space Debris Conference, ESA SP-473.

See, T., et al. (Eds.), 1990. Meteoroid and debris impact features documented on the Long-Duration Exposure Facility: A preliminary report, JSC-24608.

Settecerri, T.J. and E.G. Stansbery, 1997. Measurements of the orbital debris environment: Comparison of the Haystack and HAX radars, JSC-27971.

Settecerri, T.J., et al., 1997. Haystack radar measurements of the orbital debris environment; 1994-1996, JSC-27842.

Settecerri, T.J., et al., 1999. Radar observations of the orbital debris environment: Haystack and HAX radars Oct 1990-Oct 1998, NASA JSC-28744.

Stansbery, E.G., et al., 1996. Haystack radar measurements of the orbital debris environment; 1990-1994, JSC-27436.

Taylor, E.A., et al., 1998. Impacts on HST and EuReCa solar arrays compared with LDEF using a new glass-to-aluminum conversion, COSPAR 1998, Adv. Space Res., in press.

Vardi, Y. and D. Lee, 1993. From image deblurring to optimal investments: Maximum likelihood solutions for positive inverse problems, J. R. Statist. Soc. B **55**, No. 3.

Vaughan, W.W., et al., 1999. The NASA Marshall solar activity model for use in predicting satellite lifetime, Adv. Space Res. **23**, No. 4.

Watts, A., et al., 1993. Dimensional scaling for impact cratering and perforation, NASA Contractor Report NCR 188259.

Yano, H., 1999. Japanese contribution to in-situ meteoroid and debris measurement in the near Earth space, Earth, Planets Space **51**.

Yano, H., 2001. Personal communication.

Zhang, J.-C., and D.J. Kessler, 1993. Orbital debris and meteoroid population as estimated from LDEF impact data. In LDEF—69 months in space: Third post-retrieval symposium (A.S. Levine, Ed.), NASA CP-3275.

APPENDIX A: ORDEM96 VS. ORDEM2000

The 1999 Haystack and HAX radar observations for objects greater than 1 m, 10 cm, and 1 cm are compared with both ORDEM96 and ORDEM2000 model predictions in Figures A-1 to A-3.

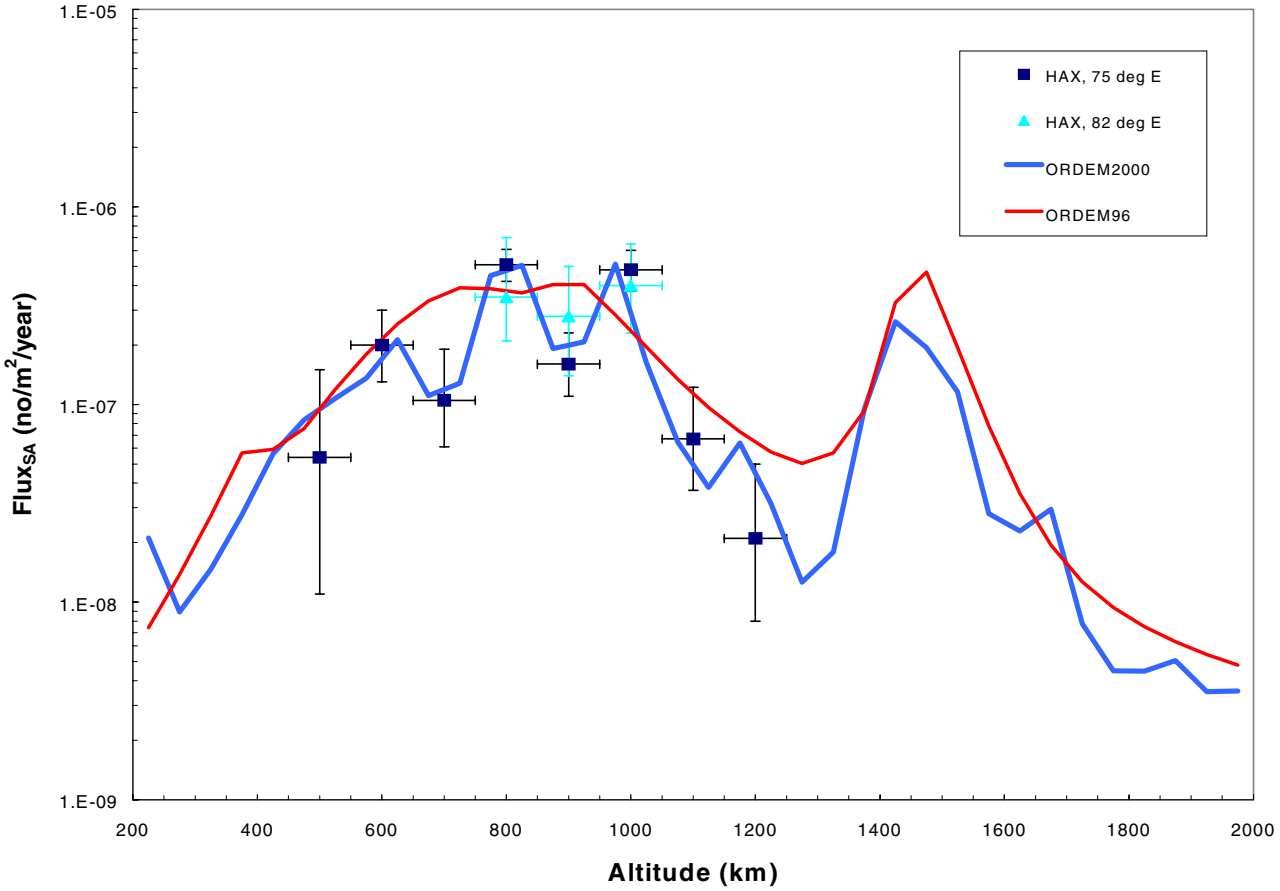

Figure A-1: ORDEM2000, ORDEM96 vs. HAX data (1999, objects >1 m).

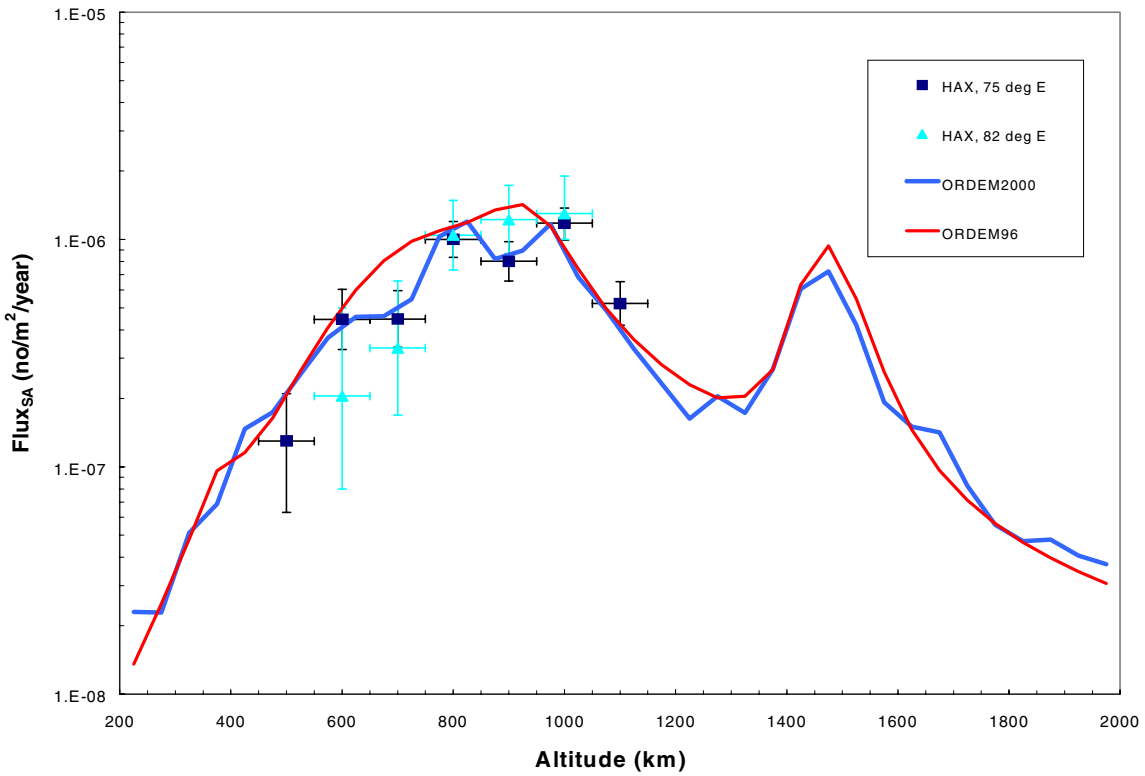

Figure A-2: ORDEM2000, ORDEM96 vs. HAX data (1999, objects >10 cm).

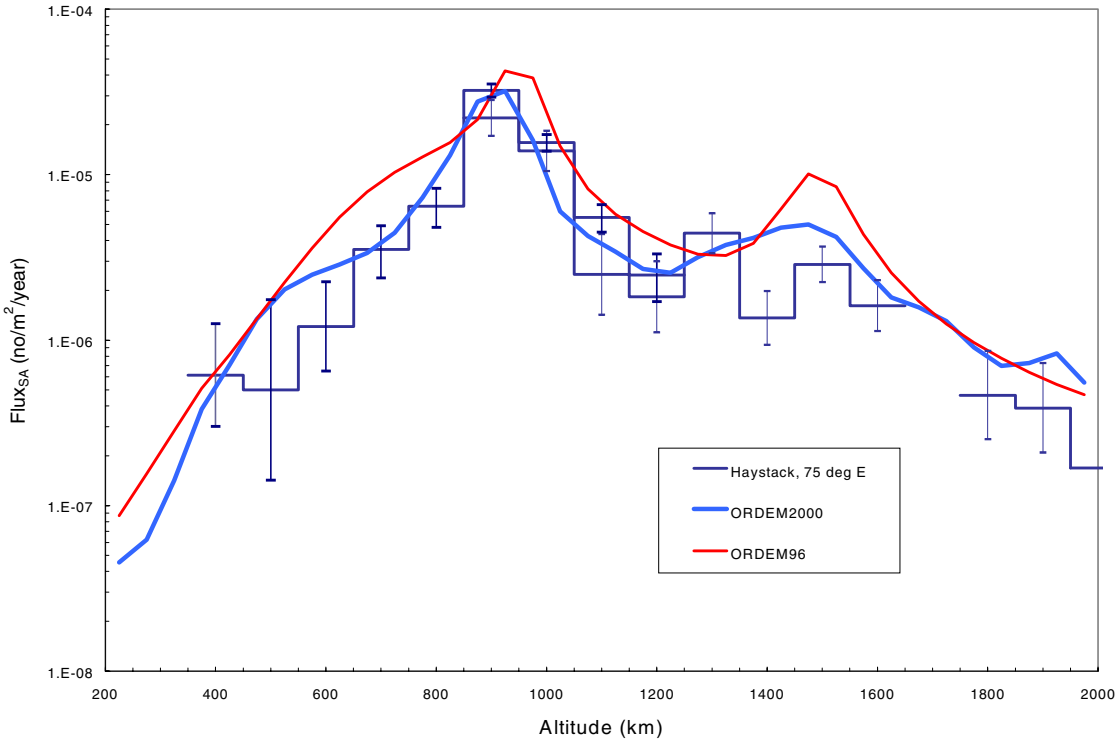

Figure A-3: ORDEM2000, ORDEM96 vs. Haystack data (1999, objects >1 cm).

APPENDIX B: DEBRIS FLUX AT 400 KM ALTITUDE (1999-2030)

The cross-sectional fluxes on a spacecraft with an orbit similar to that of ISS (circular orbit at 400-km altitude, 51.6-deg inclination) between 2000 and 2030 are shown in Figures B-1 to B-7. Both ORDEM2000 and ORDEM96 predictions are included.

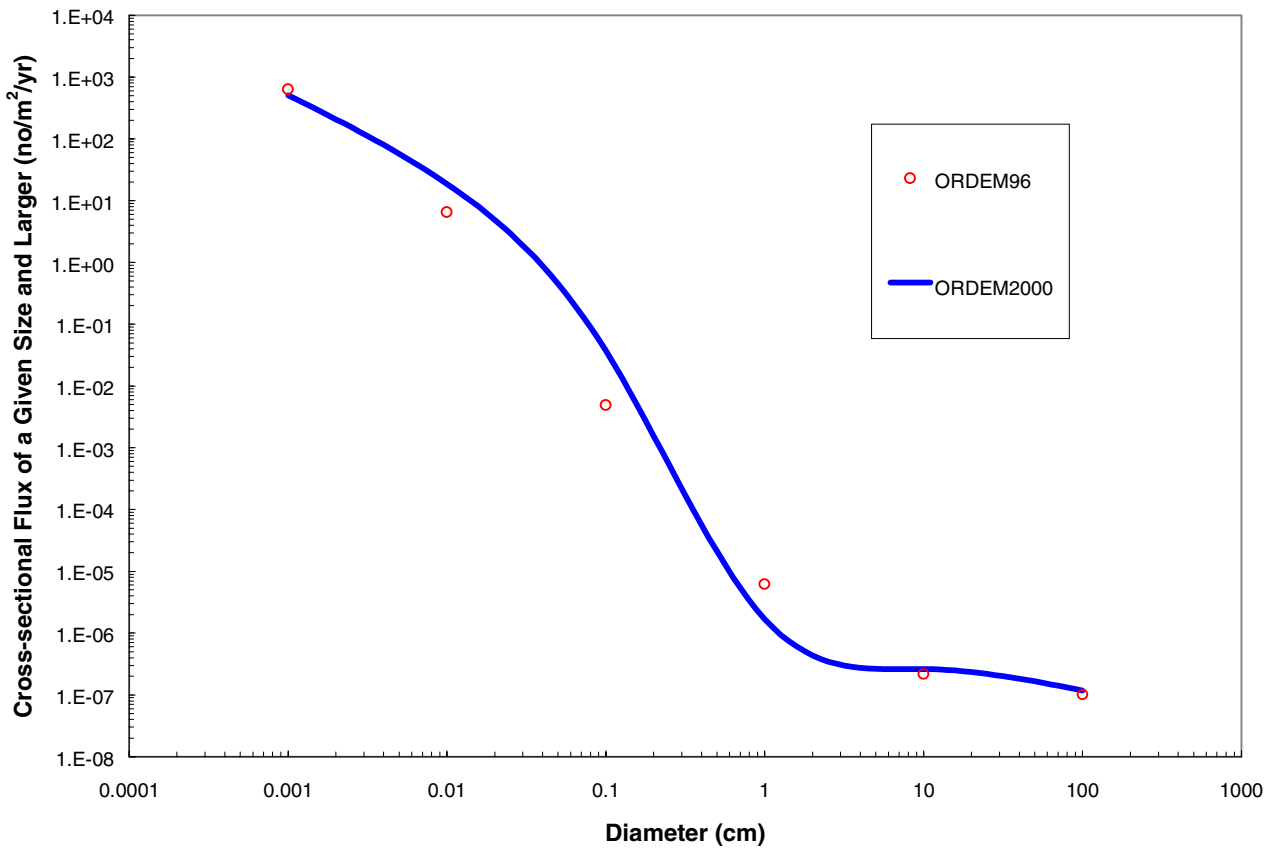

Figure B-1: Debris flux on ISS in 2000.

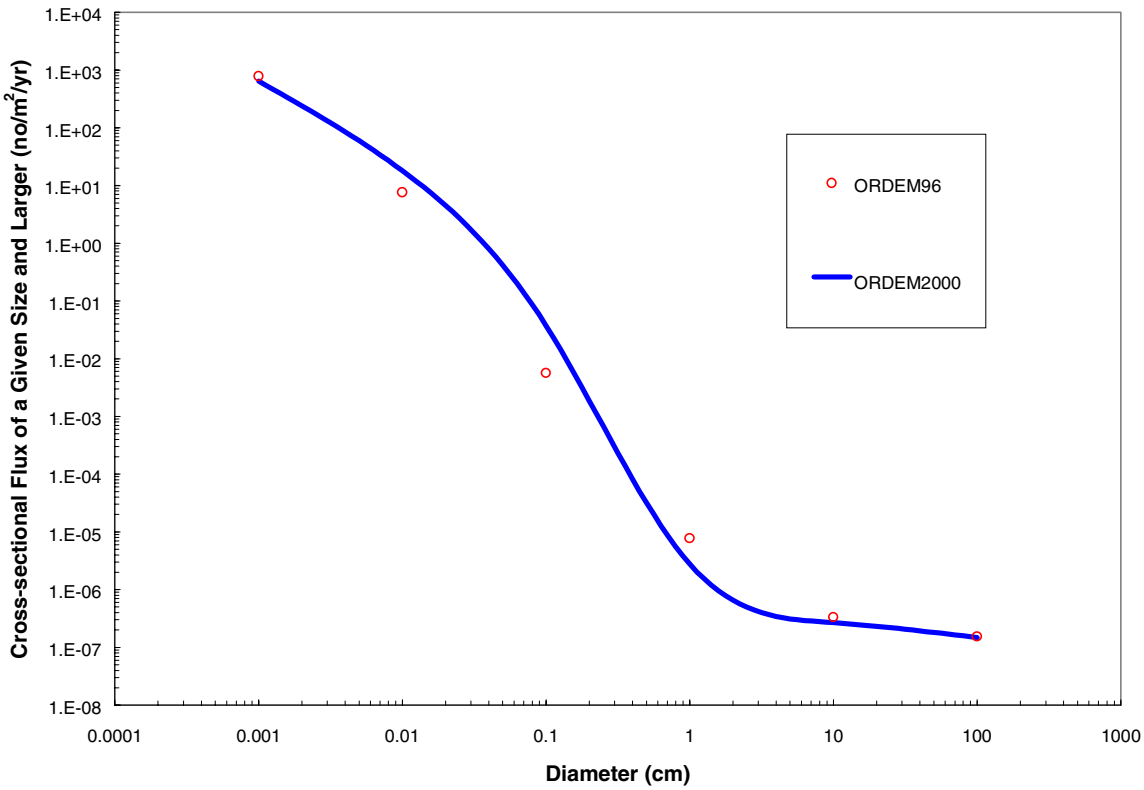

Figure B-2: Debris flux on ISS in 2005.

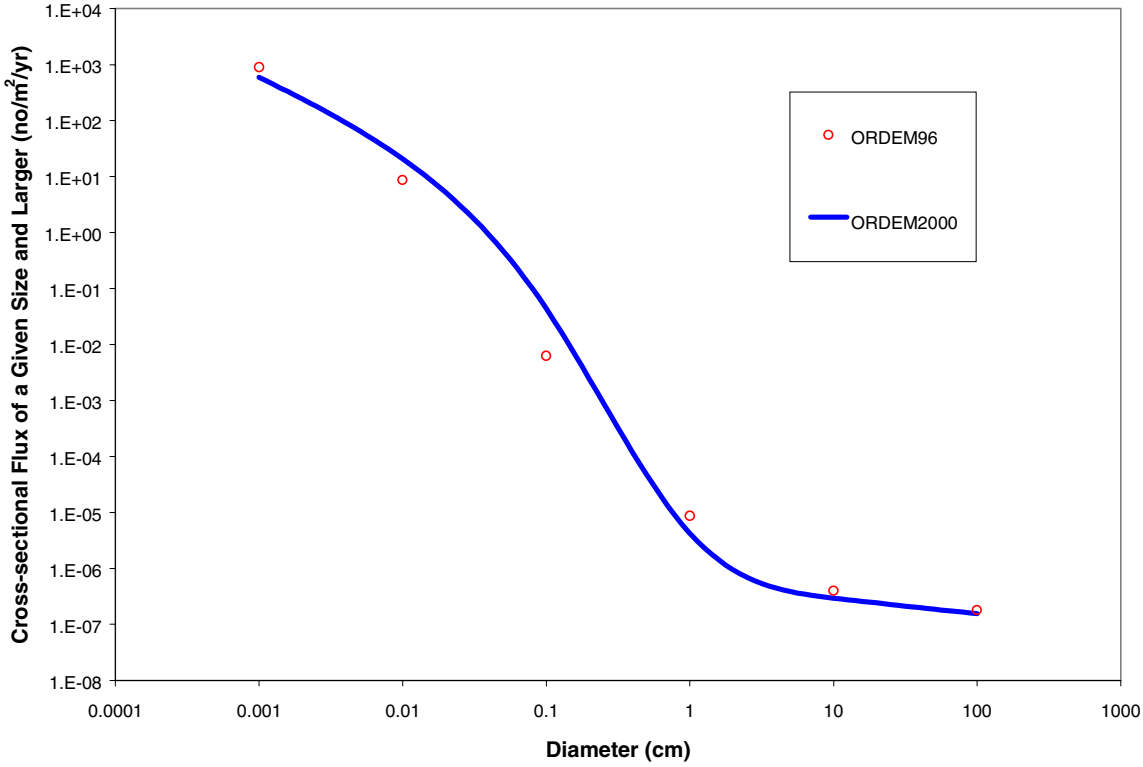

Figure B-3: Debris flux on ISS in 2010.

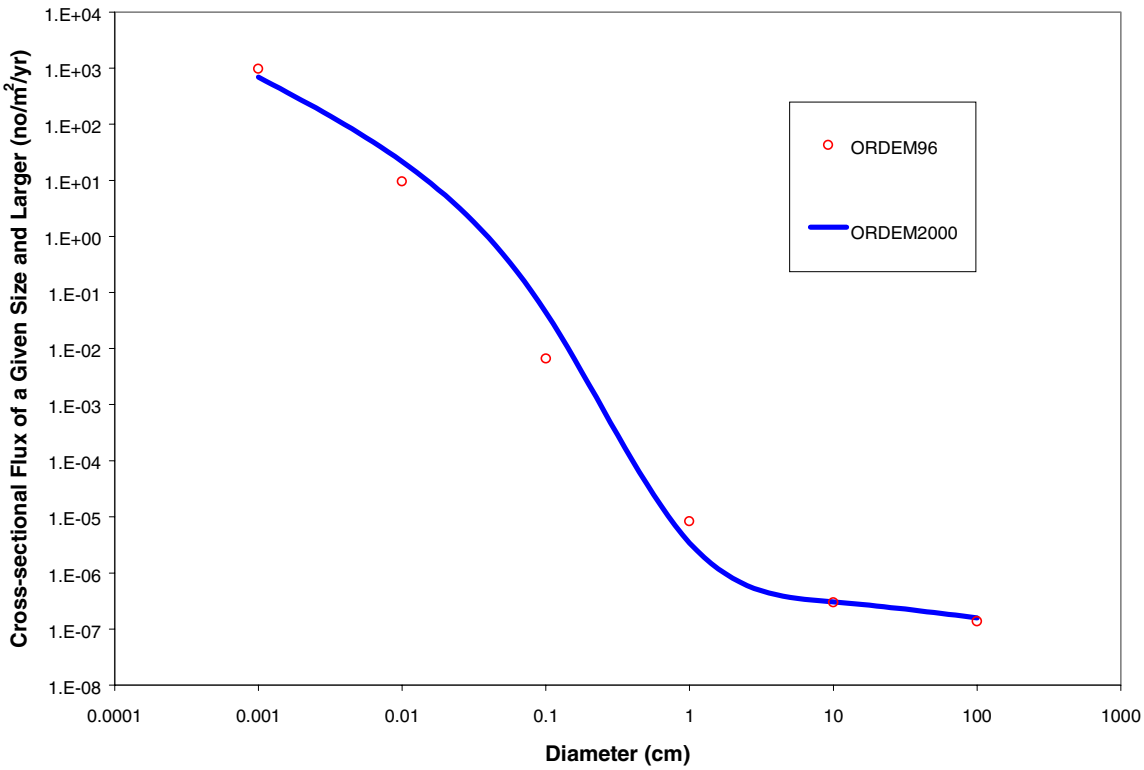

Figure B-4: Debris flux on ISS in 2015.

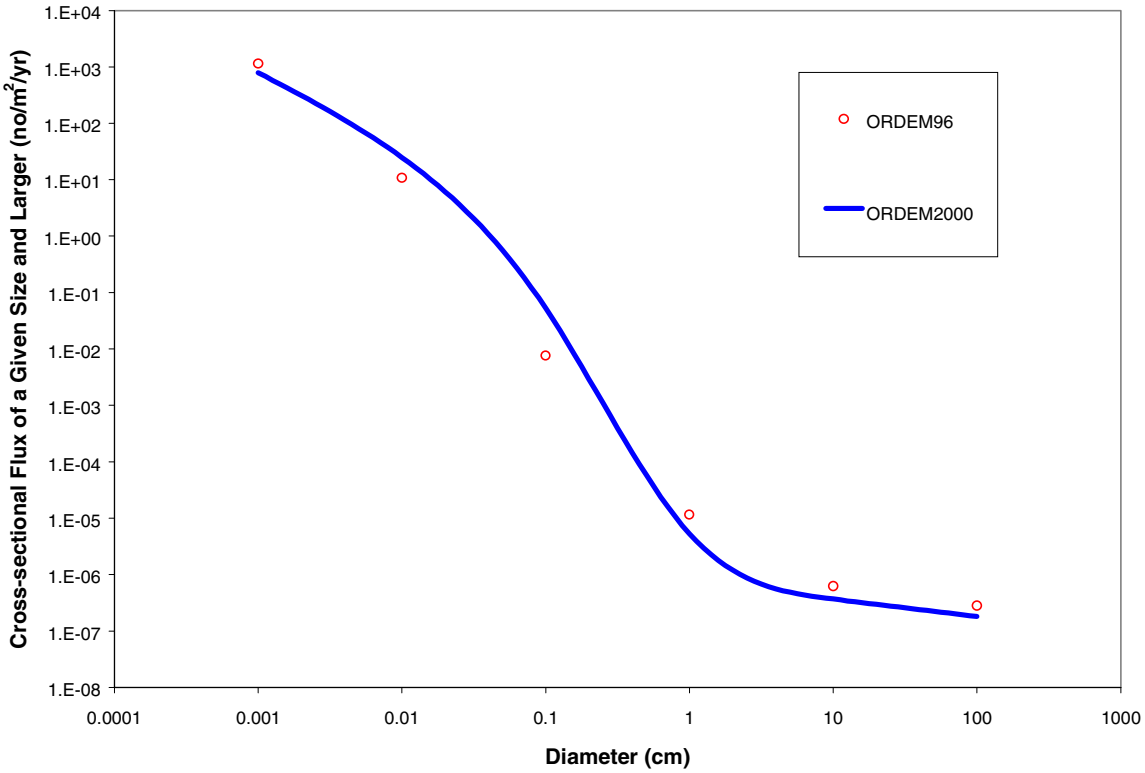

Figure B-5: Debris flux on ISS in 2020.

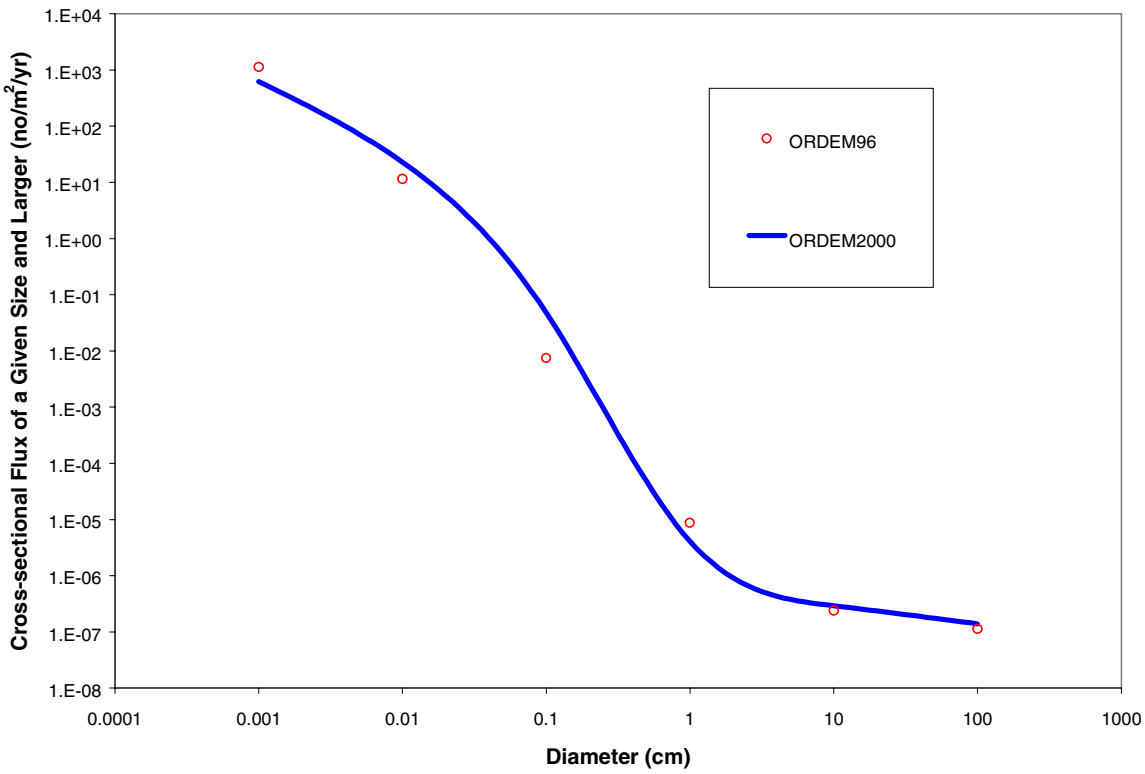

Figure B-6: Debris flux on ISS in 2025.

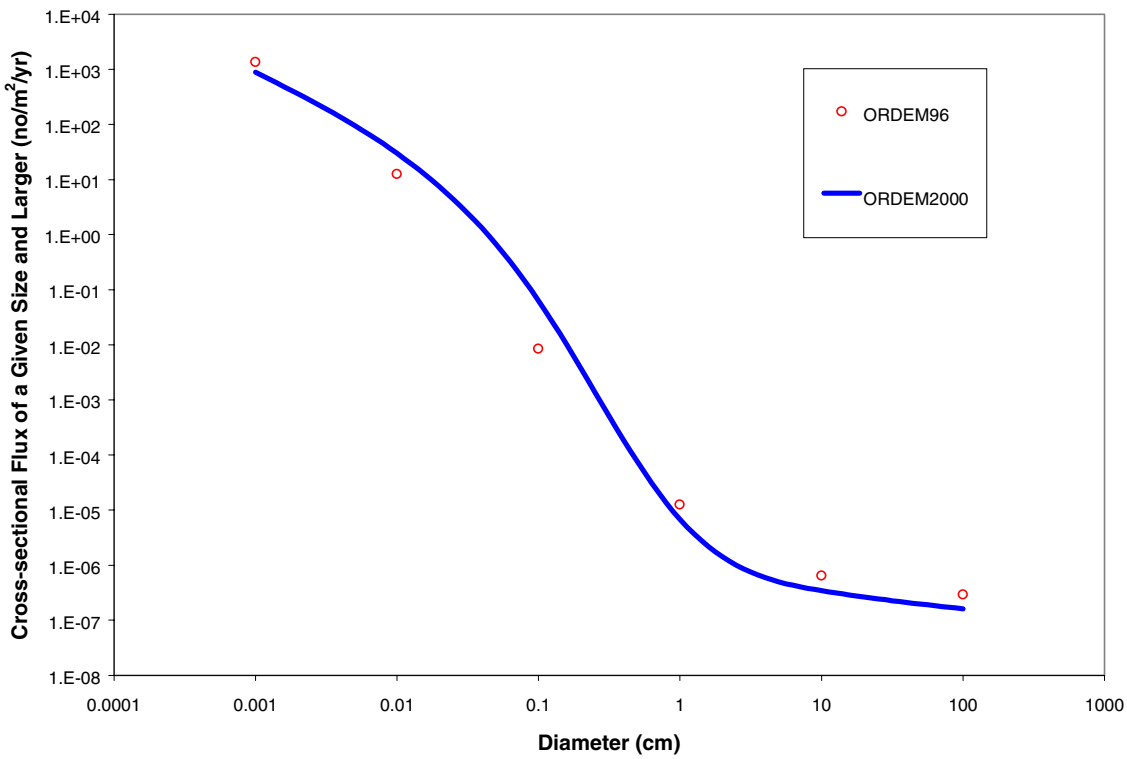

Figure B-7: Debris flux on ISS in 2030.

APPENDIX C: AVERAGE VELOCITY DISTRIBUTIONS

There are multiple ways to define the velocity distribution of a flux. The most generic is to have the flux binned in direction, speed, and size, as is done in the "Butterfly" module of ORDEM2000. For each velocity speed and direction v_i, there is an associated flux f_i.

However, there are some useful "average" velocities that one can compute. One is the density-weighted average velocity. This is the average velocity (<v>) that relates the local spatial density (ρ) to the direction- and velocity-averaged flux (<*f*>).

$$\rho < v > = \sum_{i=1}^{N} f_i$$

This is the average velocity printed in the output screen. However, if a user wishes to compute the most likely velocity that will hit a spacecraft, the flux-weighted average velocity is needed.

$$< v_f > = \frac{\sum_{i=1}^{N} f_i \, v_i}{\sum_{i=1}^{N} f_i}$$

Ultimately, to compute risk to a spacecraft, one must integrate the flux in detail over all sizes, directions, and impact speeds. This information is provided for the user in the "Butterfly" module.